

# **Optogenetic Stimulation Combined with High-Field fMRI (Opto-fMRI): A New Method for Examination of Evoked BOLD Responses and Functional Connectivity**

A dissertation

by,

**Mitul M. Desai**

In partial fulfillment of the requirements for the degree of

Doctor of Philosophy  
in  
Biomedical Engineering

Tufts University  
August, 2011

Adviser:

**Prof. Christopher I. Moore**

Committee:

**Prof. Mark Cronin-Golomb (Chair and Academic Adviser)**

**Prof. Christopher I. Moore (Research Adviser)**

**Prof. Sergio Fantini**

**Prof. Heather Urry**

## Abstract

Behaviors and brain disorders involve neural circuits that are widely distributed in the brain. The ability to map the functional connectivity of distributed circuits, and to assess how this connectivity evolves over time, will be facilitated by methods for characterizing the network impact of activating a specific sub-circuit, cell type, or projection pathway. In this thesis high-resolution blood oxygenation level-dependent (BOLD) functional MRI (fMRI) at 9.4 Tesla is used to examine the distributed BOLD response in primate and rodent brain.

In this thesis a high-resolution fMRI method for tracking activity in the squirrel monkey brain is developed. This method simultaneously provides sub-millimeter functional resolution and near whole-brain coverage. This method is used to delineate the effect of state dependent changes, as modeled through isoflurane anesthesia modulation, on tactile fMRI responses in somatosensory and basal ganglia regions. This study also examines the changes in functional connectivity between somatosensory and the basal ganglia region as isoflurane depth is modulated.

In this thesis a novel approach was described that combines optical neural activation of specific cells in the mammalian brain, with fMRI of resultant BOLD signals, or ‘Opto-fMRI.’ By optically activating channelrhodopsin-2 (ChR2)-expressing excitatory neurons in the primary somatosensory (SI) barrel cortex of mice during an optimized high-resolution fMRI protocol. Using this novel method we were able to reliably identify cortical and subcortical targets of pyramidal cells of the primary somatosensory cortex (SI), in an anesthetized as well as an awake mouse brain. To demonstrate the use of Opto-fMRI in characterizing the brain state dependence of functional connectivity, we assessed the impact of isoflurane anesthesia on activity and correlation of activity across areas in the barrel cortex, and the network stimulated due to barrel cortex activation. These collective results suggest opto-fMRI can provide a controlled means for characterizing the distributed network downstream of a defined cell

class in the awake brain. Opto-fMRI may find use in examining causal links between defined circuit elements in diverse behaviors and pathologies.

In this thesis we also used opto-fMRI to examine the relation between neural activity and the BOLD response. Extracellular electrophysiological recordings were used to measure the effects of stimulation on single-unit, multi-unit, and local field potential activity. Optically driven stimulation of layer V neocortical pyramidal neurons resulted in a positive local BOLD response at the stimulated site. Consistent with a linear transform model the BOLD response summated in response to closely spaced trains of stimulation demonstrating an equivalent response to a multi-synaptic method of driving cortical activity using somatosensory stimulation. These results bolster the underlying assumptions of BOLD fMRI and demonstrate the utility of opto-fMRI for probing the relation of the BOLD response to the underlying neuronal activity.

## **Acknowledgments**

This thesis would not have been possible without the contribution and support of many people. First and foremost, I would like to express my gratitude and appreciation to my advisor Prof. Christopher I. Moore. I am very grateful for his guidance, support and motivation. I am very fortunate to be his student and to have worked in some the most cutting edge topics in the field of neuroimaging. Every project that I have worked with him had been exciting, rewarding and a great learning experience.

I would like to thank Prof. Mark Cronin-Golomb, Prof. Sergio Fantini, and Prof. Heather Urry, who kindly gave their time to serve on my thesis committee and I am grateful for their helpful feedback on my work. I would also like to thank the chair of the Biomedical Engineering Department, Prof. David Kaplan.

This thesis work would not have been possible without the collaboration with Massachusetts Institute of technology and McGovern Institute for Brain Research. I feel fortunate to have the opportunity to work in a collaborative environment that has allowed me to learn so much about neuroscience and neuroimaging. I would like to thank entire MRI team of The A. A. Martinos Imaging Center at the McGovern Institute for Brain Research for their resources without which none of the studies in this thesis work would have been possible. Especially, I would like to thank Christina Triantafyllou, Steven Shannon, and Seeba Arnold Anteraper for their constant support and technical collaboration.

I am fortunate to have the opportunity to work with Prof. Edward S. Boyden. I thank him for his input, advice and mentorship, which have significantly contributed to this thesis. I am also fortunate to have the opportunity to work and collaborate with Prof. Ann M. Graybiel for past 4 years. She has played an important role in the success of this thesis and my graduate studies on a whole.

I would like to express my appreciation to Itamar Kahn (now Prof. Itamar Kahn) for sharing his experience on fMRI neuroimaging studies and for the many enlightening discussions on neuroscience in general. I really appreciate Itamar's help, support and making equal contribution towards successfully implementing opto-fMRI. I would also like to thank him for his input, advice and encouragement, which have significantly improved the quality of this thesis.

I would like thank Ulf Knoblich and Dominique Pritchett for their support in electrophysiology and behavioral studies. I have learned a lot from both of them, everything from dcLFP to monkey behavior. It was fun working with them and I am going to miss the long conversations that were often not limited to science alone. I would also like to thank Josh Siegel for his help with designing and making mouse restraint system. I would like to thank the members of the Moore lab, past and present, Aimee Nelson, Cheryl Cheney, Jason Ritt, Mark Anderman, Dorea Vierling-Claassen, Jessica Cardin, Ethan Skowronski-Lutz, Bryan Higashikubo, Junjie Liu, Rosa Cao, and Talia Konkle for their friendship and support. I would especially like to thank Alexis Bradshaw and Kate Wan, who as 'Lab Consigliere' made working in the Moore lab a lot easier.

I would like to acknowledge the financial support provided by the SGER grant and McGovern Institute for Brain Research.

I would like to thank my family and friends, especially my wife Rupangi, our son Ved, and my parents, Mukesh and Hema, for their love and support. For letting me do what I wanted to do and their trust in me. Without them none of this would have been possible.

## Table of Contents

<b>Chapter 1. Introduction</b> .....	1
1.1. Statement of the problem .....	1
1.2. Objectives .....	4
1.3. Thesis outline .....	6
<b>Chapter 2. Background and Motivations</b> .....	11
2.1. Small animal functional MRI (fMRI) studies .....	11
2.2. The BOLD fMRI contrast mechanism .....	14
2.3. Anesthesia and its effect on brain activation.....	16
2.4. Measuring functional connectivity .....	18
2.5. Optogenetic control and functional connectivity studies .....	20
<b>Chapter 3. The impact of isoflurane anesthesia depth on tactile activation of neocortex and striatum: High-resolution 9.4T fMRI studies in squirrel monkeys</b> .....	25
3.1. Introduction .....	25
3.2. Methods .....	28
3.2.1. Overview Of The Experiment .....	28
3.2.2. Non-MR Aspects of the Experiment .....	29
3.2.2.1. <i>Animal Setup</i> .....	29
3.2.2.2. <i>Tactile Stimulation</i> .....	34
3.2.3. MR Aspects of the Experiment .....	36
3.2.4. fMRI Data analysis .....	37
3.2.4.1. <i>Single subject analysis</i> .....	37
3.2.4.2. <i>Group analysis</i> .....	39
3.2.4.3. <i>Time series extraction and ROI analysis</i> .....	41
3.2.4.4. <i>Rest state functional connectivity analysis</i> .....	41
3.3. Results .....	42
3.3.1. BOLD responses Evoked By Vibro-tactile Stimulation of the Third Digit .....	42
3.3.2. Isoflurane modulates the probability of activation and strength of the BOLD signal .....	46

3.3.3. Isoflurane depth modulates the resting state correlations between regions that exhibits BOLD response to the stimulation.....	49
3.4. Discussion .....	51
<b>Chapter 4. Opto-fMRI: Integration of Optical Neural Control and Functional Magnetic Resonance Imaging.....</b>	<b>56</b>
4.1. Introduction .....	56
4.2. Methods.....	58
4.2.1. Animals and surgery.....	58
4.2.2. Opto-fMRI: Experimental setup and protocol.....	63
4.2.3. Control experiments .....	65
4.2.4. Opto-fMRI: data analysis .....	68
4.2.5. Region of interest (ROI) identification and cross-registration .....	69
4.2.6. Time series extraction and ROI analysis .....	72
4.2.7. Local field potential (LFP) and multi-unit activity (MUA) recordings.....	72
4.2.8. Histology .....	73
4.3. Results .....	74
4.3.1. Opto-fMRI hardware and protocol of usage.....	74
4.3.2. Demonstration of opto-fMRI drive of neocortical areas connected to SI barrel cortex.....	76
4.3.3. Consistency of Opto-fMRI outcomes across sessions and animals ....	81
4.3.4. High-resolution imaging with Opto-fMRI .....	87
4.4. Discussion .....	90
<b>Chapter 5. Opto-fMRI: Mapping Brain Networks in Awake Mice .....</b>	<b>95</b>
5.1. Introduction .....	95
5.2. Materials and Methods.....	97
5.2.1. Animals and surgery.....	97
5.2.2. Awake and anesthetized opto-fMRI of mouse: Experimental setup and protocol.....	100
5.2.3. Opto-fMRI of mouse: data analysis.....	105
5.2.4. Region of interest (ROI) identification and cross-registration .....	106
5.2.5. ROI time series analysis. ....	107

5.3. Results .....	108
5.3.1. Optimization of opto-fMRI methods for awake mice .....	108
5.3.2. BOLD signal changes downstream of SI pyramidal cell activation..	110
5.3.3. Neural targets recruited by SI pyramidal cell activation can be automatically identified .....	116
5.3.4. Opto-fMRI evokes a greater BOLD response in awake than anesthetized animals .....	120
5.3.5. Anesthesia affects BOLD functional connectivity in the network recruited by pyramidal cell activation .....	128
5.4. Discussion .....	131
<b>Chapter 6. Characterization of the Functional MRI Response Temporal Linearity via Opto-fMRI .....</b>	<b>137</b>
6.1. Introduction .....	137
6.2. Materials and Methods .....	139
6.2.1. Animals.....	139
6.2.2. Animal Anesthesia and Surgery .....	139
6.2.3. Light stimulation.....	139
6.2.4. Sensory stimulation .....	140
6.2.5. MRI Procedures .....	141
6.2.6. Electrophysiology .....	142
6.2.7. Electrophysiology Analysis .....	143
6.2.8. Statistical Procedures.....	144
6.2.9. Histology .....	144
6.3. Results .....	145
6.4. Discussion .....	153
<b>Chapter 7. Summary and Future Direction .....</b>	<b>156</b>
7.1. Summary .....	156
7.2. Future directions.....	159
<b>Chapter 8. References.....</b>	<b>162</b>

## List of Tables

<b>Table 4.1.</b> Summary of animal usage and fMRI parameters for different experiments throughout Chapter 4.....	59
<b>Table 4.2.</b> Control experiment in 0.5% isoflurane-anesthetized Thy1-ChR2 to examine blood pressure dependence on SI illumination.....	66
<b>Table 5.1.</b> Summary of animal usage and fMRI parameters for different experiments throughout Chapter 5.....	98

## List of Figures

<b>Figure 2.1.</b> Image SNR as a function of voxel volume and magnetic field strengths. ....	14
<b>Figure 2.2.</b> SE-EPI and GE-EPI BOLD fMRI percent signal changes as a function of cortical depth in the cat visual cortex. ....	16
<b>Figure 2.3.</b> Optogenetic tools to control neuronal firing. ....	21
<b>Figure 3.1.</b> Animal positioning in cradle. ....	32
<b>Figure 3.2.</b> Schematic drawing of the tactile stimulator. ....	35
<b>Figure 3.3.</b> Tactile stimulation paradigm. ....	37
<b>Figure 3.4.</b> Correlation threshold criteria. ....	39
<b>Figure 3.5.</b> Between sessions and between animal image alignment. ....	40
<b>Figure 3.6.</b> Functional activation in primary somatosensory cortex. ....	43
<b>Figure 3.7.</b> Functional activation in lateral sulcus and basal ganglia areas. ....	44
<b>Figure 3.8.</b> Time courses of the BOLD signal. ....	46
<b>Figure 3.9.</b> Anesthesia modulation of distributed neural activation patterns. ....	47
<b>Figure 3.10.</b> Anesthesia modulation of BOLD signal change in distributed neural activation patterns. ....	48
<b>Figure 3.11.</b> Spontaneous (rest state) functional connectivity analysis. ....	49
<b>Figure 3.12.</b> Rest state functional connectivity analysis to assess anesthesia modulation of distributed neural activation patterns. ....	51
<b>Figure 4.1.</b> Design of ‘Opto-fMRI’ setup. Left, schematic of Opto-fMRI setup for measuring distributed neural activation patterns due to optical perturbation of an opsin-expressing cell type. ....	60
<b>Figure 4.2.</b> RF coil design, cement usage, and EPI distortion elimination. ....	62
<b>Figure 4.3.</b> fMRI BOLD response in a Thy1-ChR2 mouse for blue and yellow laser light illumination over SI barrel field and undergoing right hind paw stimulation. ....	67

<b>Figure 4.4.</b> Demonstration of ‘Opto-fMRI’ methodology. ....	78
<b>Figure 4.5.</b> Negative BOLD signal in mouse brain with and without Chr2, and in fMRI phantoms. ....	80
<b>Figure 4.6.</b> Distributed neural activation patterns obtained via Opto-fMRI. ....	83
<b>Figure 4.7.</b> Raw single-slice EPI images in Thy1-ChR2 mice undergoing opto-fMRI. ....	85
<b>Figure 4.8.</b> Signal to noise (SNR) map for mouse RF coil. ....	87
<b>Figure 4.9.</b> Sub-columnar resolution Opto-fMRI. ....	88
<b>Figure 5.1.</b> Design of ‘Opto-fMRI’ setup. Left, schematic of Opto-fMRI setup for measuring distributed neural activation patterns due to optical perturbation of an opsin-expressing cell type. ....	99
<b>Figure 5.2.</b> Signal-to-noise characteristics pre- and post-acclimation. ....	101
<b>Figure 5.3.</b> Demonstration of ‘Opto-fMRI’ methodology in awake mice. ....	110
<b>Figure 5.4.</b> Positive and negative signals revealed by opto-fMRI in the presence and absence of Chr2. ....	112
<b>Figure 5.5.</b> Mapping of neural targets recruited by SI pyramidal cell activation in the awake mouse brain. ....	114
<b>Figure 5.6.</b> Raw opto-fMRI data for all 5 individual mice expressing Chr2 in SI and imaged awake. ....	115
<b>Figure 5.7.</b> Unbiased algorithmic mapping in the awake mouse brain. ....	117
<b>Figure 5.8.</b> Robustness of the algorithmic component of the opto-fMRI mapping process. ....	120
<b>Figure 5.9.</b> Opto-fMRI analysis of brain state modulation of causal network dynamics: effects of anesthesia on SI network recruitment. ....	121
<b>Figure 5.10.</b> Unbiased algorithmic mapping of neural targets recruited by SI pyramidal cell activation in the anesthetised mouse brain. ....	122
<b>Figure 5.11.</b> Opto-fMRI analysis of brain state modulation of causal network dynamics: effects of anesthesia on induced BOLD response. ....	124
<b>Figure 5.12.</b> Opto-fMRI analysis of brain state modulation of causal network dynamics: effects of anesthesia on induced BOLD response in Thy1-ChR2 mice. ....	127

<b>Figure 5.13.</b> Opto-fMRI analysis of brain state modulation of causal network dynamics: effects of anesthesia on functional connectivity.....	129
<b>Figure 5.14.</b> Opto-fMRI analysis of brain state modulation of causal network dynamics: effects of anesthesia on functional connectivity in Thy1-ChR2 mice. ....	130
<b>Figure 6.1.</b> Neural activation of layer V ChR2-expressing neurons by light stimulation evokes a reliable fMRI response.....	145
<b>Figure 6.2.</b> Neural activation of layer V ChR2-expressing neurons by light stimulation evokes a reliable fMRI response that is equivalent to somatosensory response evoked by whisker deflection. ....	148
<b>Figure 6.3.</b> Precisely evoked spike and local field potential activity for 1 s trains of optical stimulation of primary somatosensory cortex.....	150
<b>Figure 6.4.</b> The BOLD response shows linear temporal summation for closely spaced short trains of stimulation. ....	152



# **Chapter 1. Introduction**

## **1.1. Statement of the problem**

Functional magnetic resonance imaging (fMRI) is a powerful approach for measuring neural responses in distributed brain networks that are involved in the common processing of sensory stimuli, motor tasks, and more complex cognitive functions. The local and global extent of activation, as well as the relative spatial relationships of these brain areas, can be visualized and registered to the underlying anatomical features on structural magnetic resonance images (MRI). This technique is noninvasive, thus making it especially fitting for longitudinal studies of temporally extended processes – such as development, learning, and disease progression and treatment (Giedd et al. 1999; Hertz-Pannier et al. 2002; Kim et al. 2006; Tombari et al. 2004; Ward et al. 2003).

A drawback of fMRI studies is that an activation map thus produced does not always reflect network dynamics. fMRI maps the regions involved in a given task and shows how these regions are interconnected, but offers little information about how regions interact functionally. Studying how regions communicate with other regions of a network is important in understanding how information is relayed between regions in the brain.

To probe the ‘functional’ meaning of a given brain area observed in fMRI requires the ability to causally control at least one point the system, to stimulate or

disrupt specific regions and then track the consequences at multiple sites in the network. A prime example of such an invasive form of causal control is electrical micro-stimulation (Ekstrom et al. 2008; Logothetis et al. 2010; Moeller et al. 2008; Tolias et al. 2005). While powerful, this specific technique has limitations. Because electrical micro-stimulation can be non-specific to cell type, it is not well suited to studying the impact of specific cell types on a functional network. More generally, such stimulation can even activate fibers passing near a region, not only the cells in it, making interpretation often problematic. Also, electrical micro-stimulation is an invasive technique and thus not viable for chronic and repeated experimentation – what is otherwise one of the strengths of fMRI studies.

With the advent of optogenetics it is now possible to either activate or silence specific cell types with different colors of light (Boyden et al. 2005a; Zhang et al. 2007a). These optical neural control methods utilize the genetically-driven expression of light-driven proteins, such as the light-gated ion channel channelrhodopsin-2 (ChR2), in specific cells in the brain. This selectivity allows control (activation and silencing) of a specific neural pathway and/or cell classes in a largely intact nervous system. As a consequence we can assess the causal influence of a defined neuron type on local or downstream neural computations and network activity (Cardin et al., 2009; Cardin et al., 2010; Boyden et al. 2005a; Chow et al. 2010; Han and Boyden 2007a; Zhang et al. 2007b; Zhao et al. 2008).

Combining optical neural control methods with fMRI opens up the ability to assess the brain-wide influence of a specific set of neural circuit elements, and enables explorations of how such a functional map is modulated by development,

learning, or pathology. Further, we anticipate this combined methodology will find many uses in the systematic mapping of functional neural connectivity throughout neuroscience, in not only traditional genetic model organisms such as mice, but also species such as non-human primates (Han et al. 2009), and a unique role in neural circuit insights derived from animal experimentation towards improvements in human neurology and psychiatry.

In this dissertation a combined fMRI and optogenetics manipulation method is presented, and its reliability and uses are probed. It is demonstrated that the combined opto-fMRI method elicits clear, repeatable, distributed patterns of network activity following optical activation of excitatory neurons in the neocortex of mice, with high spatial resolution that is sufficient to resolve sub-columnar activity patterns in the cortex. It is also demonstrated that opto-fMRI can be used to characterize the impact of brain state (modeled through the modulation of anesthesia levels) upon the network recruited by a specific neuron type in a specific region.

The vibrissa sensory system is widely employed for studies of neural processing and behavior (Andermann and Moore 2006; 2008; Ritt et al. 2008; Woolsey and Van der Loos 1970), because of its regular columnar architecture and a one-to-one correlation between barrels and whiskers on the rodent snout. Except for the high-field somatosensory squirrel monkey fMRI study, throughout this dissertation the rodent vibrissa system model is used to study sensory processing and as a test-bed for technique development.

Most fMRI studies on animal models involve general anesthesia to eliminate movement artifacts. Although animal studies under anesthetized conditions remain valuable, and unavoidable under many circumstances, the use of anesthetics has a profound influence on cerebral circulation, metabolism, and neural-vascular coupling. fMRI of awake animals offers many distinct advantages, e.g., avoiding confounding effects of anesthesia, ability to study higher-order cognitive functions. Due to these advantages there have been significant efforts to optimize fMRI of awake monkeys (Ferris et al. 2001; Logothetis et al. 1999; Vanduffel et al. 2001) and rodents (Lahti et al. 1998; Sicard et al. 2003). In this dissertation, an awake opto-fMRI setup in mice is implemented to study regions of the brain that have substantial differences in blood oxygenation level-dependent (BOLD) fMRI responses between awake and anesthetized condition.

## **1.2. Objectives**

The broader objective of this thesis is to develop methods that extend unique aspects of small-animal high-field fMRI and to deploy them to better understand how neurons within a particular functional network interact.

More specifically, in this dissertation optogenetic stimulation is used to manipulate a specific set of neurons during simultaneous measurement of brain activity with high-field fMRI. This combined methodology is termed as ‘opto-fMRI’. In this thesis, I describe methods we developed to test opto-fMRI’s reliability, and demonstrate the use of this combined method in multiple

experimental contexts that are of importance for neuroscience. The goal was to optimize key technical approaches, including the critical hardware design choice, surgical strategies, MRI pulse sequences, and data analysis methods required to combine fMRI in awake mouse with optical control of defined neural networks in the brain that are necessary to implement opto-fMRI successfully. A more specific goal of this work was to demonstrate that opto-fMRI elicits clear, repeatable, distributed patterns of network activity following optical activation of excitatory neurons in primary somatosensory barrel fields (SI-BF) in mice, with high spatial resolution, sufficient to resolve sub-columnar activity patterns in the cortex and to characterize the functional connections of SI-BF projections.

Another objective of this dissertation is to demonstrate how opto-fMRI can be used to study the effect of state dependent changes on the induced BOLD response and the functional connectivity. Here the state dependent change is modeled through manipulating isoflurane anesthesia depth and studying its effect on brain wide neuronal responses and the functional connectivity between different regions of the brain.

In this dissertation the relation between neural activity and BOLD responses evoked using optogenetic and sensory stimulation is also examined. More specifically, we probe whether the BOLD response evoked by closely spaced bouts of optically driven pyramidal cell activity summates linearly and compare this result to vibrissa-stimulation evoked BOLD response. Optogenetically evoked BOLD responses are also compared to electrophysiology measures of unit activity and local field potentials.

### 1.3. Thesis outline

**Chapter 2**, “Background and Motivations”, serves as a reference point for the chapters to follow. This chapter starts with a discussion about the advantages of small-animal fMRI studies. The motivation behind going to high-field MRI is discussed next. A detailed discussion on the properties of the fMRI BOLD signal is then presented, along with some specific design choices that can be made in using a high-field MRI scanner for high-resolution scanning. Next, the challenges of using anesthesia in small-animal fMRI studies to reduce stress and motion artifact is discussed. The advantages and disadvantages of different anesthesia protocols are also discussed in this section. The next section of this chapter discusses the state-of-the-art in functional connectivity studies, and points out the motivations for combining functional connectivity studies to techniques that allows causal manipulation of neural circuits. In the final section of this chapter, one such approach, optogenetic, is discussed in detail. The background for this technique and the potential of combining this technique with fMRI functional connectivity studies are highlighted.

**Chapter 3** demonstrates a high-resolution (9.4 T) fMRI study for tracking activity in the primate brain (squirrel monkey). This method simultaneously provides sub-millimeter functional resolution and near whole-brain coverage. This study is also designed to delineate the effect of isoflurane on tactile fMRI activation. Three levels of anesthesia (0.6%, 1.0% or 1.4% end-tidal isoflurane depth) were presented to three animals in eight independent imaging sessions.

Tactile stimulation was presented by custom tactile stimulators to the distal and middle pads of the 3<sup>rd</sup> digit. Along with tactile stimulation, rest scans were also obtained when the finger-pads were not stimulated. The findings in this study demonstrate differential sensitivity of sensory-driven fMRI signals in different regions of somatosensory network to changes in isoflurane depth. This study also demonstrates the efficacy of high-field fMRI for probing brain activation and connectivity in a primate brain.

**Chapter 4** presents a study that combines optogenetic manipulation with high-field fMRI. This novel method is termed as ‘opto-fMRI.’ This chapter describes the means for achieving ultra-high resolution fMRI (up to  $100 \times 100 \mu\text{m}^2$  in-plane resolution) using a 9.4 T scanner, and across multiple brain areas in mice during optical activation of a specific cell type in a specific region of the brain. In this study mice expressing Channelrhodopsin-2 (ChR2; a channel that is sensitive to blue light), either transgenically under the Thy1 promoter or virally transduced under the  $\alpha\text{CaMKII}$  promoter, are used. This study describes key innovations including the hardware, surgical strategies, pulse sequences, and clustering and cross-correlation data analytic methods appropriate for determining how the activity in a neural network is influenced by optically-controlled stimulation of a defined node within a neural circuit. Optical stimulation of ChR2-expressing excitatory neurons in the somatosensory cortex, reliably and consistently revealed fMRI activation patterns in a functional network of neocortical areas. This study also demonstrates how different parts of a neural network are activated by a single upstream target site and establish the reliability

of opto-fMRI to probe these networks – across imaging sessions and animals. In this study opto-fMRI experiments are implemented in lightly anesthetized mice – 0.5% end-tidal isoflurane depth.

**Chapter 5** describes an approach of using opto-fMRI in an awake mouse brain. This technique measures the distributed BOLD responses evoked by optical activation of a defined cell class of neurons expressing ChR2. In this study the utility of the opto-fMRI approach was explored by identifying known cortical and subcortical targets of pyramidal cells of the primary somatosensory cortex (SI), and by analyzing how the set of regions recruited by optogenetically-driven SI activity differs between the awake and anesthetized states. This study demonstrates how positive BOLD responses was observed in a distributed network that included secondary somatosensory cortex (SII), primary motor cortex (MI), caudoputamen (CP), and contralateral SI (c-SI), by optogenetically-driven SI neurons. This study also examines the network connectivity (correlations between pairs of regions) changes in the anesthetized mice (0.7% isoflurane) when compared to awake mice.

In **Chapter 6** opto-fMRI is used to study the relation between neural activity and the BOLD response. This study examines a property, temporal linear summation, of sensory evoked BOLD responses and compares them to optogenetically evoked BOLD responses. Temporal linear summation, wherein the induced BOLD response summates in linear manner to closely spaced trains of stimulation, was validated by a vibrissa deflection stimulation. This study then examines if the optogenetically evoked BOLD response also summates in a

temporally linear manner. This chapter also examines how optogenetically evoked BOLD responses compare to the electrophysiological measures of unit activity (single- and multi-unit) and the local field potentials.

**Chapter 7** provides the summary of this dissertation along with an outline for future directions.



## **Chapter 2. Background and Motivations**

Magnetic Resonance Imaging (MRI) is a widely used technique for studying human anatomy and function (fMRI). With the widespread availability of MRI scanners, many studies use the blood oxygenation level dependent (BOLD) contrast as a marker of variations in brain activity. BOLD fMRI in a short period of time (less than 20 years) has become the most prevalent method for investigating human brain function. The BOLD response provides us an unparalleled view of neural activity in the human brain. fMRI has not only revolutionized human brain research, but also contributed to a variety of important domains in small-animal neuroscience research. These include studies of the pathophysiology of brain function, the basic science of brain activity, and functional connectivity of different sensory circuits.

### **2.1. Small animal functional MRI (fMRI) studies**

The availability of high-field MRI scanner systems with bore sizes suitable for small-animals (e.g. rodents, cats, ferrets, small primates, etc.) has advanced the field of high-resolution small animal neuroimaging. Most small animal fMRI techniques use the hemodynamic response to local neuronal electrical activity as a surrogate measure of underlying neural function. Similar to human brain studies, the most commonly used fMRI method is measuring the

blood oxygenation level dependent (BOLD) contrast. The BOLD contrast mechanism reflects changes in cerebral blood volume, cerebral blood flow, and oxygen consumption. High-resolution small-animal fMRI is an ideal technique for studying fMRI BOLD contrast. Further, small-animal fMRI studies can also be used to develop new forms of contrast, i.e., manganese-enhanced MRI (MEMRI), Cerebral Blood Flow (CBF), Cerebral blood Volume (CBV), Oxygen metabolism (CMRO<sub>2</sub>), and other molecular imaging probes.

One of the biggest advantages that small-animal fMRI offers over human fMRI is the ability to combine fMRI with other modalities – especially the more invasive ones like electrophysiology and pharmacochemical manipulations. Thus small animals can be used wherever an fMRI study in humans is not possible – to either study pathology or even the basic science of functional activity, and functional connectivity. Small-animal fMRI is also an excellent tool for longitudinal studies to visualize disease progression, therapy, functional reorganization and plasticity.

The signal-to-noise ratio (SNR) in MRI scales linearly with the field strength (Hoult et al. 1986). **Figure 2.1** shows this experimentally, where for a given resolution the raw SNR for a high-field scanner (7 T) is higher than that for low field scanners (1.5 T and 3 T). Not only the raw SNR, but the sensitivity and specificity of the BOLD contrast, also increase for the higher field strengths. Theoretical sensitivity of BOLD contrast goes up with the field strength more than quadratically, despite a shortening in transverse relaxation times (T<sub>2</sub> and T<sub>2</sub>\*) at high fields. This increase in sensitivity has been experimentally

demonstrated at fields up to 7 T in humans (Gati et al. 1997; Yacoub et al. 2001) and 9.4 T in animals (Lee et al. 1999). Even when physiological noise is taken into account, the sensitivity of BOLD contrast increases linearly for higher field strengths compared to the lower field strengths (Triantafyllou et al. 2005; Triantafyllou et al. 2004). Increased sensitivity of the BOLD contrast allows higher spatial and temporal resolution in the fMRI studies. Study of the rat somatosensory cortex performed at 11.7 T (Silva and Koretsky 2002) has revealed the ability of high-field fMRI in providing a map of layer specific structure. The desire to further improve the sensitivity and specificity of fMRI BOLD contrast has been a major force driving the move towards higher magnetic fields for *in vivo* fMRI studies in small animals.

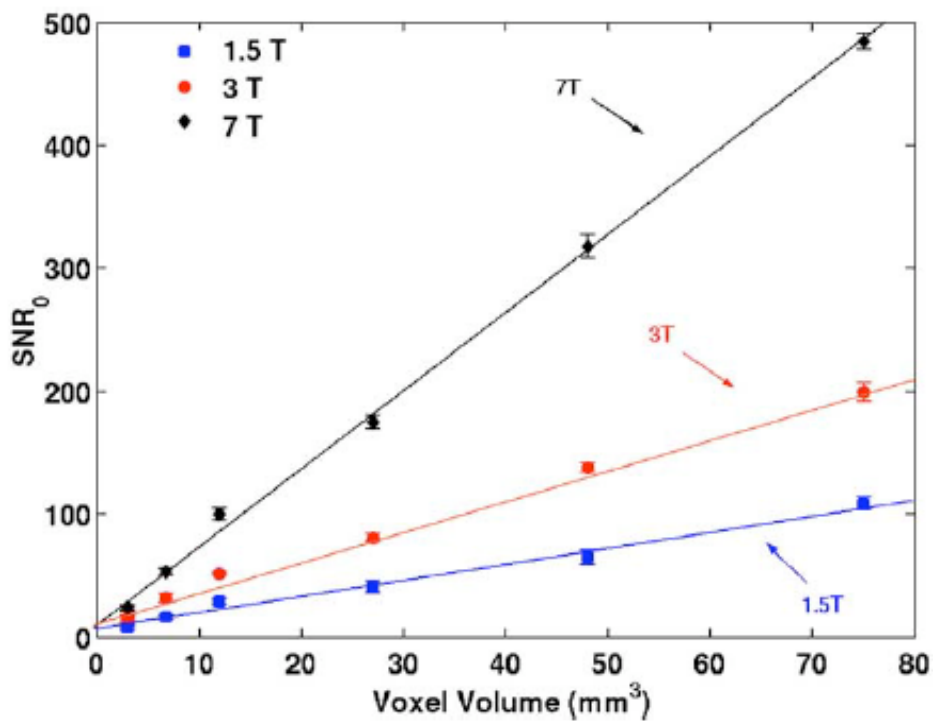


**Figure 2.1. Image SNR as a function of voxel volume and magnetic field strengths.** Measurements derived from areas of cortical gray matter and are averages over five subjects at each field strength. Lines are linear least-squares fit to the data. SNR was normalized for bandwidth differences and differences in the degree of partial Fourier acquisition. *Adapted from (Triantafyllou et al. 2005), with authors' permission.*

## 2.2. The BOLD fMRI contrast mechanism

Even though most studies use BOLD contrast as a marker of variations in brain activity, the origins of BOLD contrast remains a hotly debated topic. The BOLD signal does not directly measure neural activity and relies on an indirect correlate. It is therefore vital to understand the BOLD signal to properly interpret data from BOLD fMRI studies.

A change in blood flow following neural activity was first reported in the late 19th century (Fulton 1928; Roy and Sherrington 1890; Sokoloff 1960; Sokoloff and Kety 1960). However, mapping hemodynamic changes following neural activity was only possible after the introduction of the deoxyglucose (2DG) autoradiography and later by Positron emission tomography (PET) (Fox and Raichle 1986; Raichle et al. 1976a; Raichle et al. 1976b; Sokoloff et al. 1977). PET allowed mapping activated regions detecting the effects of neural activity on variables such as CBF, CBV and CMRO<sub>2</sub>.

Through a series of PET studies it was discovered that when a region in the brain is activated, the local supply of oxygenated blood far exceeds the increase in oxygen metabolism (Fox et al. 1988; Fox and Raichle 1986). This phenomenon is known as *functional hyperemia*. A neural activation is followed

by an increased local blood flow that increases the oxy- to deoxy-[Hb] ratio. Thus this increase in oxy-[Hb] is correlated to neural activation.

In 1936 Linus Pauling discovered that the hemoglobin molecule is diamagnetic when oxygenated (oxyhemoglobin; oxy-[Hb]) and is paramagnetic when it is not (deoxyhemoglobin; deoxy-[Hb]). Thus, any change in oxy- to deoxy-[Hb] ratio can be measured by an MRI method that is sensitive to magnetic inhomogeneity (referred to as the T2\* weighted method). As the name suggests, the BOLD signal measures this change in magnetic inhomogeneity evoked by blood oxygenation changes. The discovery of BOLD fMRI in the early nineties by Ogawa and colleagues (Ogawa et al. 1990a; Ogawa et al. 1990b; Ogawa et al. 1993; Ogawa et al. 1992) was a major breakthrough in brain imaging research.

It is also important to note that the change in inhomogeneity depends on the fMRI method employed. The vast majority of fMRI BOLD studies use gradient-echo (GE) echo planer imaging (EPI) technique, which is sensitive to large vessels and small capillaries for the change BOLD signal. At high-field strengths (9.4 T) spin-echo (SE) EPI, in contrast, eliminates the non-specific contribution from extra-vascular BOLD signal changes in the vicinity of large venous vessels (**Fig. 2.2**). SE-EPI is also less sensitive to susceptibility-related signal dropout. Thus using SE-EPI, instead of GE-EPI, increases the effective functional resolution of the BOLD contrast in high-field strength fMRI studies.

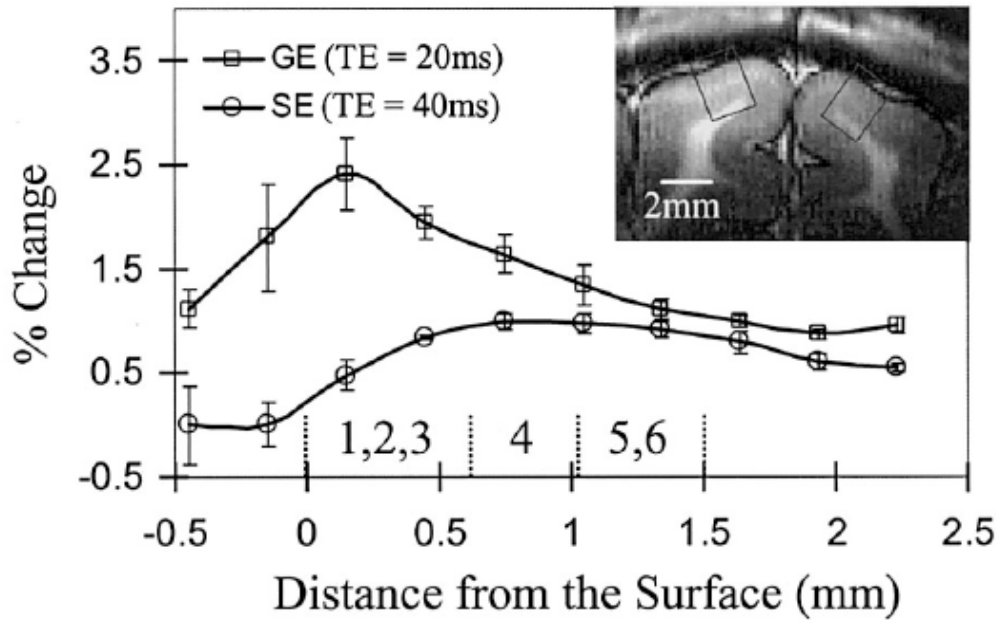


**Figure 2.2. SE-EPI and GE-EPI BOLD fMRI percent signal changes as a function of cortical depth in the cat visual cortex.** T1-weighted image with two rectangular sections, chosen for the depth-specific signal analysis. Data from Gradient Echo (TE = 20 ms) and Spin Echo (TE = 40 ms) BOLD fMRI were used without a statistical threshold. The dorsal surface of the cortex is at zero, and increasingly positive distances indicate deeper cortical regions. Approximate schematic boundaries between the upper (layers I–III), middle (layer IV), and lower (layers V and VI) cortical layers are also shown as dashed vertical bars. Spatial resolution of the data points is 300  $\mu\text{m}$ . GE BOLD percent changes monotonically decrease with depth, but SE BOLD percent changes are minimal at the surface of the cortex. Error bars are SEM (N = 6 animals). *Adapted from (Zhao et al. 2004) with authors' permission.*

### 2.3. Anesthesia and its effect on brain activation

The majority of small-animal fMRI studies require that animals are anaesthetized during the study period, instead of using a rather time-consuming and challenging training period to get the animals acclimated to the magnet environment and related issues such as scanner noise (King et al. 2005). The use

of anesthesia also minimizes stress-induced effects on the physiological responses of interest and facilitates animal handling (Peeters et al. 2001).

Various anesthetics have been tested in small-animal (predominantly rodent) fMRI studies for compatibility with functional activation using BOLD contrast (Lindauer et al. 1993; Nair and Duong 2004; Ueki et al. 1992). The coupling of functional activity of the cerebral cortex with blood flow and metabolism is sensitive to anesthetics (Crosby et al. 1983). Many anesthetics are known to either reduce or suppress the coupling between functional activation and metabolic and blood flow responses (Crosby et al. 1983; Meyer et al. 1969). The most widely used anesthetic agents in small-animal BOLD fMRI studies are  $\alpha$ -chloralose (Ahrens and Dubowitz 2001; Leniger-Follert and Hossmann 1979) and urethane (Xu et al. 2003). However, both have serious drawbacks, mainly toxicity, that excludes their application for longitudinal fMRI studies. Isoflurane is also used widely in small-animal fMRI studies (Masamoto et al. 2009a).

Isoflurane is known to alter functional connectivity by modifying the characteristics of spontaneous neural activity (amplitude, frequency, and synchrony) or by changing properties of the vasculature. Despite confounding effects of anesthetics on brain-wide neuronal response and functional connectivity, studying mechanisms of anesthesia through BOLD fMRI studies remains promising. Functional connectivity studies provide a means of investigating the modulation of functional networks at varying levels of anesthesia.

## 2.4. Measuring functional connectivity

The use of fMRI methods to study *in-vivo* connectivity in the brain has grown dramatically over the past several years. While a large part of this growth is due to the availability of diffusion tensor imaging (DTI), examining connectivity using BOLD contrast has also been widely adapted. The general term used for connectivity studies using BOLD contrast is “functional connectivity studies”, and was defined by Friston and colleagues (Friston et al. 1993) as “temporal correlation between spatially remote neurophysiological events”. In the functional connectivity fMRI (fcMRI) analysis method, regions are considered functionally connected if their activity is correlated. Functional connectivity does not imply a physical pathway, but includes patterns of connectivity that are entirely mediated by the common influence of some external event on distant neural areas.

Much of the study of functional connectivity is carried out by examining interregional correlations in resting state (i.e., with no external stimulation). The resting state fcMRI approach can be traced to studies by Biswal et al. (Biswal et al. 1995) and Rogers et al. (Rogers et al. 2007); who observed correlations between activity in left and right somatosensory cortex during resting BOLD fMRI studies. Temporal correlations in resting state data are of special interest because they are not easily explained by externally imposed task demands.

Functional connectivity can also be measured from data collected during task performance to discover regions that are functionally connected to an exogenously driven stimulus, e.g., different regions that form a functional

network in the motor cortex during finger-tap stimulation. However, spatial patterns of inter-correlation maps produced from fcMRI studies are largely passive, they provide a snapshot of the areas interconnected to a task or at the rest state, but offer little information about how these nodes interact functionally.

While these correlational studies are powerful, studying how functionally connected regions communicate and modulate with other network elements is important to understanding how information is transferred between regions in the brain. A functional dissection of a network is required to evaluate the relative contributions of individual network element – a region or a cell types. It is however difficult to *in-vivo* perturb one element in a functional network, where the complex environment of the brain imposes obstacles to the stimulation, and then recording its subsequent effects throughout the brain.

To this end, fMRI is often combined with invasive techniques that yield the ability to stimulate or disrupt specific network elements and track the consequences at multiple sites in the network. This combined approach allows an assessment of causal influence of a specific element (a region or a cell type) in a functionally connected network. Examples of these invasive techniques include electrical microstimulation (Ekstrom et al. 2008; Moeller et al. 2008; Tolia et al. 2005) and reversible cortical deactivation through either cooling (Khachaturian et al. 2008) or pharmacological delivery. However, there are several shortcomings. In addition to being invasive, these techniques are often non-specific and unviable for chronic experimentation, and thus not well suited for repeated use in the same subject – usually a feature of fMRI studies.

## 2.5. Optogenetic control and functional connectivity studies

Traditionally, cells and synapses have been manipulated using electrical, physical, pharmacological, and genetic methods. Although much progress has been made using these classical techniques, considerable drawbacks prevent their use in the study of neural circuits with fine spatial and temporal precision *in-vivo*. Electrical and physical techniques are not spatially precise and can cause stimulation, inhibition, or inactivation of surrounding cells and processes. Pharmacological and genetic methods exhibit improved spatial selectivity but lack temporal resolution at the scale of single action potentials.

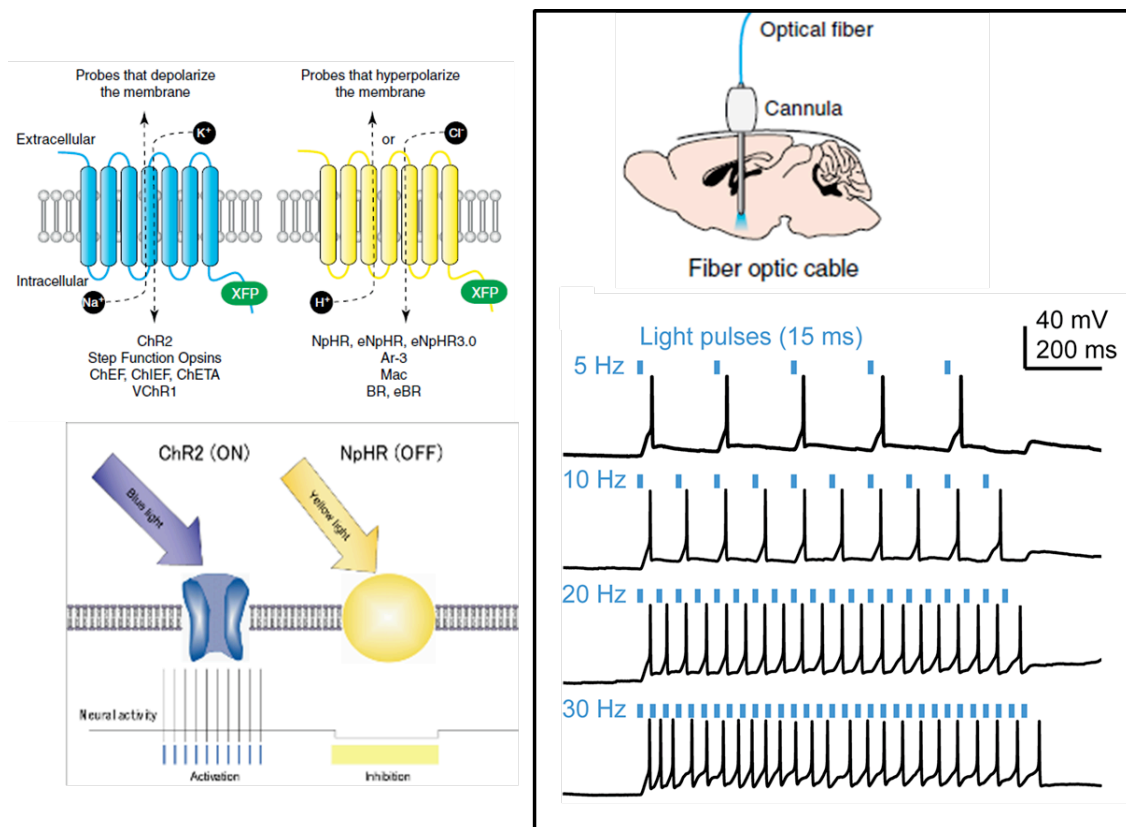


**Figure 2.3. Optogenetic tools to control neuronal firing.** Optogenetic probes are based on opsins, seven transmembrane domain proteins that interact with a chromophore (retinal or vitamin A) to become light sensitive. Probes that depolarize the membrane act as nonspecific cation channels that open in response to pulses of light. Probes that hyperpolarize the membrane actively pump either Cl<sup>-</sup> ions (in the case of NpHRs) or protons in response to pulses of light. A strategy to deliver light to transduced neurons *in vivo* is through a guided cannula is stereotaxically implanted above a target region for subsequent placement of an optic fiber. The fiber is attached to a laser diode, which might be attached to a computer or pulse generator for automatic stimulation protocols. Responses of a neuron to trains of light pulses (15 ms) at constant frequencies. Adapted from (Carter and de Lecea 2011) and (Zhu et al. 2009).

A new set of tools has been developed and now used extensively in neuroscience research to precisely stimulate (Berndt et al. 2009; Boyden et al. 2005a; Cardin et al., 2009; Gunaydin et al. 2010; Li et al. 2005; Nagel et al. 2003; Zhang et al. 2006; Zhang et al. 2007b), inhibit (Chow et al. 2010; Gradinaru et al. 2008; Gradinaru et al. 2010; Han and Boyden 2007b; Han et al. 2009; Zhang et al. 2007a; Zhang et al. 2007b; Zhao et al. 2008), or alter biochemical activity (Airan et al. 2007) in specific cells or their processes with high temporal precision and rapid reversibility. These probes are activated by light and are genetically encoded, allowing for the direct control of specific populations of cells *in vitro* and *in vivo* (**Fig. 2.3**) (Cardin et al. 2009; Gradinaru et al. 2007; Zhang et al. 2007a; Zhang et al. 2006). These new tools are collectively referred to as ‘optogenetics’ (Deisseroth et al. 2006). The unprecedented spatial and temporal precision of these tools has allowed substantial progress in revealing the structure and function of previously intractable neural circuits.

The most commonly used optogenetic probes are engineered versions of natural opsins, light-sensitive membrane-bound proteins that translocate ions across the plasma membrane in response to stimulation by specific wavelengths of light (Kramer et al. 2009). These probes can be classified as either causing a membrane depolarization, or membrane hyperpolarization.

The most commonly used probe that depolarizes the membrane is channelrhodopsin-2 (ChR2; **Fig. 2.3**, *top left*). ChR2 is a nonspecific cation channel that absorbs blue light (absorption peak of 480 nm) causing a subsequent conformational change in the transmembrane protein (**Fig. 2.3**, *bottom left*), opening the pore and allowing cations to diffuse across the membrane (Nagel et al. 2003). The ChR2 has several features that make it particularly attractive as a neuroscience probe to depolarize neurons. First, ChR2 can be activated rapidly and closes quickly upon light offset. Therefore, single action potentials can be generated with a brief pulse of blue light (**Fig. 2.3**, *right*). Second, ChR2 is a genetically-encoded protein, allowing cell-specific targeting with characterized promoter and enhancer elements and therefore eliminates the need for it to be loaded into neurons via glass pipettes or equivalent methods. Taken together, these properties make ChR2 an attractive probe for stimulating neurons with millisecond-precise temporal resolution (Boyden et al. 2005a).

The first microbial opsin to gain prominence as a tool for inhibiting neural activity (Han and Boyden 2007a; Zhang et al. 2007b) was halorhodopsin (NpHR; **Fig. 2.3**, *top left*) - a light-driven  $\text{Cl}^-$  pump that actively pumps  $\text{Cl}^-$  ions into cells in response to yellow light absorption (peak at 570 nm). Recently, additional

proteins have been discovered and characterized that can be used to inhibit neural activity in response to light (Chow et al. 2010). Instead of actively pumping  $\text{Cl}^-$  ions into a cell, these proteins function as light-driven proton pumps. Archaelhodopsin-3 (also called 'Arch') proteins allow near-100% silencing of neurons in vivo in response to yellow light with efficiency comparable to third generation NpHR – the NpHR3.0 (Chow et al. 2010).

The combination of optical neural control and fMRI could open up the ability to assess the brain-wide influence of a specific set of neural circuit elements, and enable explorations of how such a functional map is modulated by development, learning, or pathology. Further, such a unified methodology would assist in applying other neuroscientific tools in a more systematic fashion, enabling researchers to focus their electrophysiological or anatomical experiments on functionally-identified sets of brain regions.



## **Chapter 3. The impact of isofluorane anesthesia depth on tactile activation of neocortex and striatum: High-resolution 9.4T fMRI studies in squirrel monkeys**

This chapter is adapted from a manuscript prepared as:

Mitul. Desai, Itamar. Kahn, Yumi. Ishizawa, Emory. Brown, Randy. L. Buckner, Ann. M. Graybiel and Christopher. I. Moore; “The impact of isofluorane anesthesia depth on tactile activation of neocortex and striatum: High-resolution 9.4T fMRI studies in squirrel monkeys”

### **3.1. Introduction**

The basal ganglia are hypothesized to have a central role in motor coordination, habit formation and reward valuation. Sensory information is crucial to each of these processes, with somatosensory input particularly important to motor coordination and specific sub-domains of reward-related behavior (Hikosaka 1991; Pleger et al. 2008; Yin and Knowlton 2006). Somatosensory input in basal ganglia may contribute to motor coordination either directly via projections to motor regions or indirectly via projections to the thalamic nuclei (Hikosaka 1991). Somatosensory input in basal ganglia may also track reward in an integrated circuit with basic sensory areas: In humans, reward signals are represented in the primary somatosensory (SI) neocortex in a parametric manner, paralleling similar activity observed in striatum (Pleger et al. 2008). The link between somatosensory input and basal ganglia processes is also supported by disease studies (Mohammadi et al. 2011; Weder et al. 1999).

The basal ganglia receive massive projections from almost all neocortical areas, including SI. In rodents and squirrel monkeys, SI projects to the dorsolateral striatum (Brown and Marsden 1998; Flaherty and Graybiel 1991; 1995; Hoover and Strick 1993; Levesque et al. 1996; Ramanathan et al. 2002). The same part of striatum receives projections from both ipsi- and contralateral SI (Alloway et al. 2006; McGeorge and Faull 1989; Reiner et al. 2003; Wilson 1987; Wright et al. 2001). There is also a convergence of cortical connections in the striatum from corresponding somatotopic representations in multiple cortical areas (SI, SII and MI: Alloway et al. 2000; Flaherty and Graybiel 1995; 1993a; Hoffer and Alloway 2001). In primates, cortical projections preferentially target the putamen, with only a minority of fibers, from the foot representation, innervating the caudate (Flaherty and Graybiel 1991). Anatomical studies also suggest that cortical areas also participate in ‘closed’ loops with the basal ganglia and cerebellum to transmit information (Middleton and Strick 2000; 1998).

Somatosensory receptive fields have been observed in the striatum in anesthetized and unanesthetized rodents, cats and primates. A significant fraction of these neurons are multisensory (Chudler et al. 1995; Hikosaka and Wurtz 1983; 1989; Magarinos-Ascone et al. 1994; Nagy et al. 2005b; Poudroux and Freton 1979). In the anesthetized cat, neurons more involved in multisensory integration were found in the dorsolateral aspect of the caudate (Nagy et al. 2006). In the anesthetized monkey, somatosensory receptive fields for the arm were also found in dorso-anterior part of the putamen (Graziano and Gross 1993). Tactile receptive fields, in basal ganglia are often large (Nagy et al. 2005a; 2003; Nagy et

al. 2005b), in many cases covering the whole body and showing an absence of topographical organization (Nagy et al. 2005a; 2003).

While tactile receptive fields are present in caudate and putamen, relatively little is known about how response properties vary between them in the same preparation – typically studies target one or the other structure. Little is also known about their independence in information processing, and in their state-dependent connectivity with neocortex. Further, the dependence of basal ganglia on neocortical sensory input is also not fully understood. Several other sources, such as the tectum or cerebellum, could also provide this information.

To study functional responses in the basal ganglia and their relation to neocortical activity at high resolution, we utilized high-field (9.4 T) functional Magnetic Resonance Imaging (fMRI) in squirrel monkeys. To assess the brain state dependence of functional connectivity between somatosensory cortex and basal ganglia, three levels of isoflurane anesthesia were presented to these animals. Squirrel monkeys were selected as our model system for several reasons. First, squirrel monkeys have a relatively flat cortical surface and is ideal for mapping studies using techniques such as optical imaging (Chen et al. 2005; Tommerdahl et al. 2002) and electrophysiology (Sur et al. 1982), and facilitate the transition from voxel localization in fMRI to these other approaches. Second, a great deal is already known about the cortical organization of squirrel monkeys. Specifically, the representations and receptive field properties in many sensory modalities have been characterized, including tactile (Jain et al. 2001; Merzenich et al. 1987; Sur et al. 1982), visual (Livingstone 1996), auditory (Cheung et al.

2001), and vestibular (Akbarian et al. 1992; Guldin et al. 1992) cortices. This species has also been used extensively as a model for studies of basal ganglia (Flaherty and Graybiel 1991; 1994; 1995; 1993b).

We observed consistent sensory activation of SI, the bilateral lateral sulcus ("SII"), and the caudate and putamen at a 0.6% isoflurane depth. At 1.0% and 1.4% isoflurane depth, there was a loss of activation in the caudate, while SI and the putamen continued to show activation (in > 60% of imaging sessions). In contrast, the resting state correlation between SI and putamen during 'no stimulation scans significantly decreased ( $p < 0.0001$ ). The findings from our study are in apparent close agreement with a recently published rodent study (Hutchison et al. 2011) showing that while the impact of isoflurane on sensory-driven activation of SI and putamen is modest, the connectivity between these regions decreases at increased isoflurane levels.

## **3.2. Methods**

### **3.2.1. Overview Of The Experiment**

Animal and experimental setups were similar to those described in the chapter 'High-Field (9.4T) Magnetic Resonance Imaging (MRI) in Squirrel Monkey' (Nelson et al. 2006). Monkeys were transferred from their housing facility to the MRI surgical preparation room. Anesthesia was induced using sevoflurane and the animals were intubated and catheterized, and subsequently maintained on isoflurane anesthesia for the duration of the experiment. The

animals were positioned on an MR-compatible cradle (holding device) that was designed to reduce head movement. A radio frequency (RF) MRI surface coil was then secured on the animals' head for image collection. Tactile stimulator was then attached to the cradle and secured to the animals' left hand. The MRI cradle was then secured in the scanner such that the animals' head centers in the scanner bore. A series of anatomical and functional images were then acquired over a 3–6 hour period. Following scanning, anesthesia was terminated, and the animals were transferred back to their housing facility.

### **3.2.2. Non-MR Aspects of the Experiment**

#### ***3.2.2.1. Animal Setup***

Squirrel monkeys are housed in a temperature (20–23 °C), humidity (30–70%), and photoperiod (12 h dark/12 h light) controlled environment. They are single-housed in standard cages with a variety of perches and enrichment devices. The evening prior to an experiment, an animals was placed on an overnight food restriction (~5–7 hours).

Animals were transferred to the imaging site for functional imaging experiments in a custom-built anesthesia induction box. The animals were trained to enter the box without significant interaction. There is a front opening to the anesthesia induction box that has a sliding plastic door, through which the animal climbs, and a side panel that has two ducts for ventilation and an additional opening with rubber flaps for access to the lower limb to establish an intravenous (IV) catheter.

Animals were induced with anesthesia in the induction box with a moderate dose of sevoflurane anesthesia (4–8% in oxygen) for 5–7 minutes till they were completely anesthetized. Reflexes were checked to make sure the animal was fully anesthetized. Once fully anesthetized, we get 7–10 minutes to intubate the animals. We used customized, re-usable silicone cuffed 2.5 mm (inner diameter) endotracheal tubes (ET) without wire reinforcement (Med-Caire, Vernon, CT). The length of each tube was customized to fit each animal, such that it spans the distance from the mouth to the manubrium sternum. Prior to intubation, a single spray of the topical anesthetic Cetacaine was delivered to the glottis, to reduce the incidence of laryngospasm. The ET was coated with Lidocaine Hydrochloride oral topical solution and inserted into the trachea using a stylet and laryngoscope (size 1 Macintosh blade). Successful ET placement was determined by observing motion of hairs held at the opening of the ET connector, condensation on a mirror, and/or expansion/contraction of a latex covering placed at the end of the ET connector. The cuff on the ET was then inflated with air. The ET was secured by way of a velcro strap, customized with an opening that fits around the ET connector (15 mm) and wraps around the head.

At the time when the animal starts regaining consciousness from sevoflurane induction, isoflurane (1.25–2%) was provided during free breathing while an IV catheter was placed in the lateral or medial tarsal, metatarsal or saphenous vein, or alternatively in the lateral tail vein (Brady 2000) using a 24G×3/4” Surflo catheter with a 27G needle and Surflo injection plug (Terumo Medical Corporation). The IV line was then used to deliver Lactated Ringers

solution (7.5 ml/kg/hr) and atropine at 45–60 minutes intervals throughout scanning. An injection of dextrose (100–250 mg/kg IV; 5% dextrose in water as a single 3.0 ml slow dosage) was given after the animal was taken out of the scanner.

Following intubation and catheter placement, the animal was placed on mechanical ventilation (SAR-830 Series Small Animal Ventilator, CWE, Inc.), where the animal was maintained on isoflurane anesthesia in balance oxygen (0.5–0.6 L O<sub>2</sub>/minute). During animal positioning (ear bar insertion, head restraint, placement in cradle), isoflurane was maintained at 1.5% and was subsequently reduced in three incremental steps over 30 minutes to achieve 0.6% (in balanced oxygen) expired isoflurane level (measured with a V9004 Capnograph Series with inspired/expired anesthetic gas, Surgivet). Ventilation was maintained at a rate between 34–39 breaths per minute with an inspiration time of 0.5 s and expiration duration of ~1.1 s. For the anesthesia manipulation experiment, isoflurane was maintained either at 0.6%, 1.0% or 1.4% end-tidal expired level.

Throughout the experiment we monitor and record animal's physiology; end-tidal CO<sub>2</sub>, expired/inspired isoflurane concentration (V9004 Capnograph Series, Surgivet), heart rate and arterial oxygen saturation via a pulse oximetry sensor secured to the palm (Nonin 8600V), and rectal temperature. Non-invasive blood pressure from the femoral artery is also measured between functional imaging scans (V6004 Series Non-Invasive Blood Pressure, Surgivet).

Following intubation, catheter placement, and about 10 minutes of isoflurane exposure, the muscle tone gets sufficiently low and the animal was placed on the custom-made MRI cradle. The setup for imaging (**Fig. 3.1**) used throughout this paper was similar to the one illustrated in the chapter ‘High-Field (9.4T) Magnetic Resonance Imaging in Squirrel Monkey, in Development and Plasticity in Sensory Thalamus and Cortex’, Nelson, A.J., et al., 2006, Springer: New York. p.288-316 (Nelson et al. 2006). The length of the cradle encases the entire elongated outstretched body, including the tail. The body of the cradle was made from plastic piping (ID 9.5 cm, OD 11 cm), and the outer surface was covered in rubber foam pipe insulation tape (~1 mm thick) to dampen the transfer of magnet vibrations to the preparation, and to provide frictional resistance to micro-motions of the apparatus. The animal was placed on the cradle in the prone position, atop a heated water blanket (Gaymar Therma Pump, Harvard Apparatus) that controls the body temperature and maintains it at 99°F. The body was extended with the arms outstretched in front of the animal for presentation of tactile stimuli.

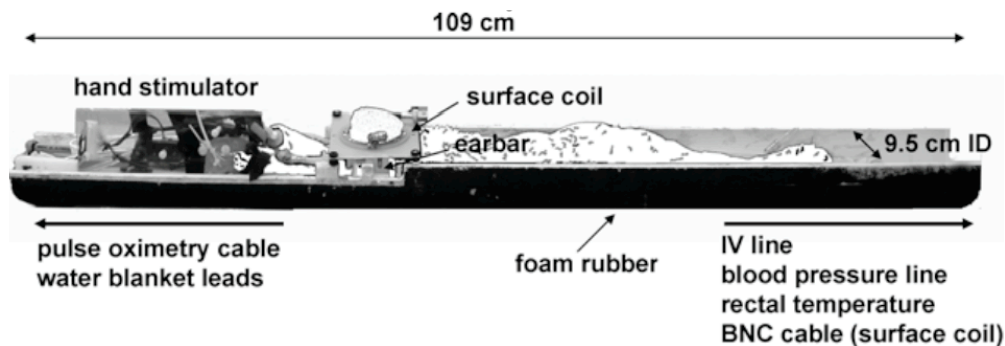


**Figure 3.1. Animal positioning in cradle.** The scanning cradle is shown with a cartoon image of the basic monkey position. The arms are extended forward, and

one hand is secured to the tactile stimulator hand mold, while the other is used for pulse oximetry measures. The cradle with foam rubber application on the base fits precisely in the diameter of the 11.7 cm 9.4 T bore. *Figure adapted from (Nelson et al. 2006).*

A proper head restraint was necessary to minimize head motion, which was critical at low isoflurane level (0.6%). We employed a triangulation of restraint – chin rest, ear bars and head piece – to restrict animal motion to an acceptable level. The chin rest consisted of a hard rubber stopper (2.4 cm height) secured on the bottom of the cradle. The ear bars were delrin cylinders (3.7 cm length  $\times$  0.4 mm diameter) tapered at their insertion tip to be non-rupturing. They were positioned at a height of 4.2 cm from the floor of the cradle. Prior to insertion into the ears, the ear bars were coated with topical anesthetic (Lidocaine HCL Jelly, 2%, Teva). The head piece consisted of a horizontal rubber slab joined at 2 points to a ‘Y’ support. To achieve identical cradle placement across scanning sessions, a peg was inserted through an opening in the posterior base of the cradle into a hole in the gradient coil insert.

Because subject motion poses a substantial challenge at the imaging resolution we use, each functional scan was subjected to motion assessment immediately following its acquisition (AFNI: Analysis of Functional Neuroimages). This near on-line motion estimation provided a rapid assessment of the effectiveness of the head restraint, which was adjusted if necessary. Only those scan that have less than 200  $\mu$ m motions within a functional imaging scan were utilized for further analyses.

#### ***3.2.2.2. Tactile Stimulation***

A custom rubber mold (left hand of the monkey; to provide stability) was mounted to an L-shaped acetyl plastic housing (2.0 cm thickness) that also housed the vibrotactile elements. The finger positions were maintained via plastic cable ties, and two velcro straps maintained the wrist in its position. **Figure 3.2**, shows a side view schematic of the stimulator. Piezoelectric (Piezo) elements (Noliac, Denmark:  $3.2 \times 0.78 \times 0.18 \text{ cm}^3$ ) were used to deliver mechanical vibrotactile stimulation to the glabrous surface of the 3<sup>rd</sup> digit of the left hand. Each Piezo was equipped with a 3 mm diameter delrin post that vibrates perpendicular to the skin surface through an opening in the mold. Two of the three Piezos were positioned such that the delrin post was in contact with the distal and the middle segments of the 3<sup>rd</sup> digit. A third Piezo element (no stimulation Piezo) was secured at a distance of 2.0 cm from the hand (not in contact with the skin) and was used to deliver a ‘no stimulation’ stimulation – one that does not stimulate the animal, but emulate vibrotactile stimulation to control for non-specific effects of Piezo vibration.

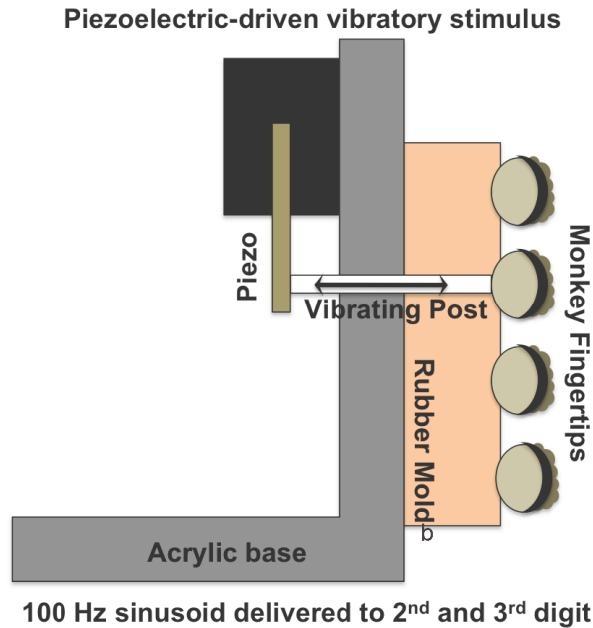


**Figure 3.2. Schematic drawing of the tactile stimulator.** A side profile schematic of the tactile stimulator in contact with the 3<sup>rd</sup> digit of the animal's left hand. Two piezos are mounted on a plastic brace, and a small plastic post that contacts the skin is slotted into a base affixed to the piezo.

Vibrotactile stimulation was controlled via custom software developed in MATLAB (The Mathworks, Natick, MA). Using a portable computer (BSI) with slots for four full sized PCI cards, signals were sent through an array of National Instruments digital output cards connected to a BNC panel. The scanner sent a TTL output at the beginning of the functional imaging scan that was routed through a digital port on the BNC panel. This TTL pulse then triggered the MATLAB program to output signals that contains the programmed vibrotactile on/off durations, waveform type, amplitude and frequency. A voltage that evoked ~80  $\mu\text{m}$  of indentation to the skin surface, was calibrated the day before the experiment, and was then used in combination with a 100 Hz sinusoidal vibration

that simultaneously stimulated the distal and the middle segments of 3<sup>rd</sup> digit of the left hand.

Once the animal and the stimulator were securely positioned in the MRI cradle, we visually inspected the stimulus before putting the MRI cradle and the animal inside the magnet bore.

### **3.2.3. MR Aspects of the Experiment**

Magnex Scientific 9.4 T 20 cm inner diameter horizontal bore magnet, with a gradient strength of 200 mT/m with fast gradient switching (100  $\mu$ s rise time) was used for our experiments. The system was equipped with Bruker Avance console, and has an effective ID of 11.7 cm with the gradient inset. We used a custom made oval transmit-receive RF surface coil ( $6 \times 4 \text{ cm}^2$ ) that fits snugly around the circumference of the animals' head. The custom RF surface coil maximized signal-to-noise (SNR) ratio, while allowing whole brain imaging.

Prior to collecting functional scans, whole brain anatomical images were collected with RARE (Rapid Acquisition Relaxation Enhancement) pulse sequences. The anatomical images were collected at a resolution of  $100 \times 100 \times 500 \mu\text{m}^3$ .

We employed a single-shot spin-echo (SE) echo planer imaging (EPI) sequence to collect BOLD fMRI at a resolution of  $450 \times 450 \times 1000 \mu\text{m}^3$  (TR = 3 s; TE = 25 ms; FOV =  $4.5 \times 4.5 \text{ cm}^2$ ; 25 slices). To keep slice prescription consistent between imaging sessions and animals, third slice of slice package (25 slices), in each imaging session, was localized on anterior commissure. Due to

the known decreases in BOLD signal with isoflurane anesthesia (Disbrow et al. 2000), 10 EPI scans were collected order to increase the chances of stimulus-evoked BOLD responses. 10 acceptable (motion of less than 200  $\mu\text{m}$ ) EPI scans were averaged for each isoflurane level, to create a grand average of functional scans for each isoflurane level.

### 3.2.4. fMRI Data analysis

#### 3.2.4.1. Single subject analysis

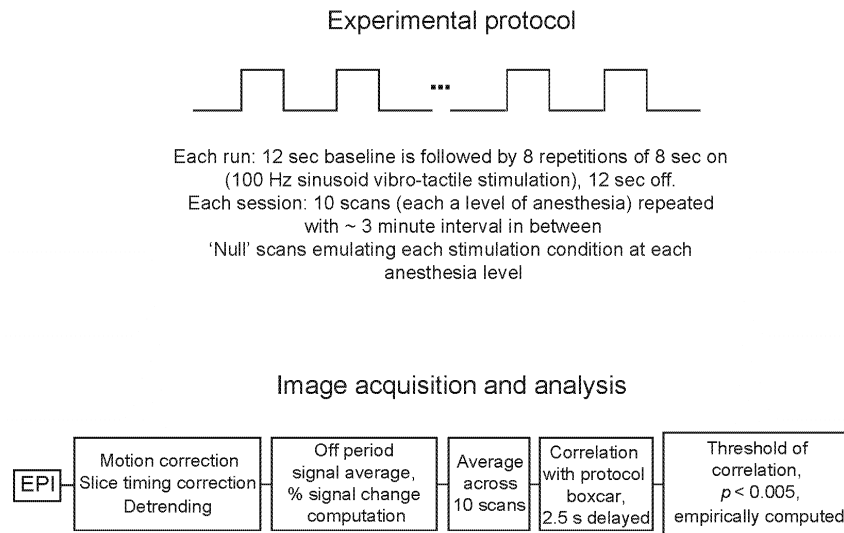


**Figure 3.3. Tactile stimulation paradigm.** *Top*, boxcar-pattern protocol for delivery of a series of 8 second periods of 100 Hz sinusoidal vibro-tactile stimulation to two distal pads of the 3<sup>rd</sup> digit. *Bottom*, images (EPIs) are motion-corrected, slice-timing corrected, detrended, converted into percent signal change by subtracting the average signal from the “no stimulation” periods, and averaged across scans. Then, the percent signal change is correlated, voxel-wise, to the boxcar pattern of the protocol, shifted forwards by 2.5 s to compensate for the BOLD delay, to determine the voxels that are significantly changing. Significance in the vibro-tactile scans was empirically computed such that we have less than 5 aberrant voxels activated in 1000 voxels ( $\sim p < 0.005$ ) in the no stimulation ‘no stimulation’ dataset.

Using a boxcar correlation and the AFNI software, the grand averaged time series (averaged for 10 EPI scans at each isoflurane level; analysis pipeline is outlined in **Fig. 3.3**) is correlated with the hypothesized hemodynamic response function. To employ an appropriate ‘significance’ level to determine significant functional response, we collected ‘no stimulation scans, wherein we stimulated the no stimulation Piezo. The no stimulation stimulus condition was used to estimate the non-physiological noise, potentially induced by the Piezo elements. The correlation threshold level was determined such that less than 5 aberrant voxels (from 1000 voxels) showed functional response for the no stimulation stimulus condition. This per imaging session, empirically determined, correlation threshold value is then set as the significance threshold for the vibrotactile functional scans. **Figure 3.4** shows an example of non-overlapping distributions of correlation values for a stimulus run versus a no stimulation scan. As noted by the black line and asterisk in this example, significance was determined at a correlation threshold of  $r = 0.42$ . The runs were acquired in the same session in alternation with vibrotactile stimulation, and an equivalent number (10) of no stimulation scans.

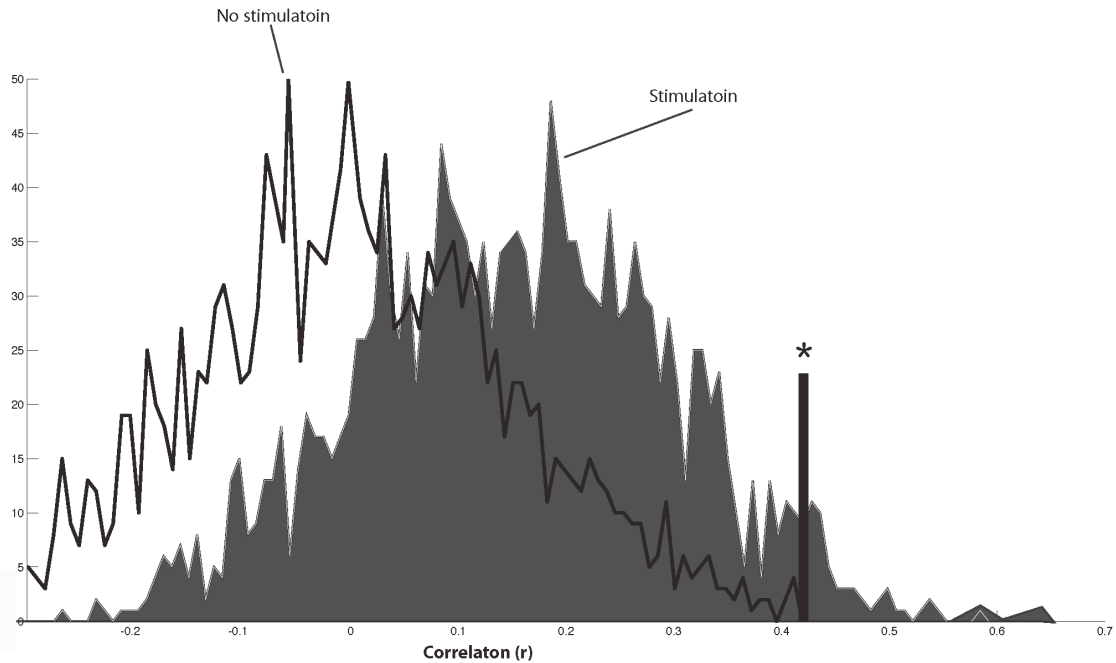


**Figure 3.4. Correlation threshold criteria.** Plotted are the frequency distributions of correlation values for a vibrotactile condition and a 'no' stimulus condition, during which a piezo element attached to the hand holder was driven using the on/off paradigm but was not in direct contact with the skin surface. Thresholds in functional imaging studies were empirically determined using 'no' stimulus false positive distributions to define the correlation threshold cutoff for  $p < 0.005$ . In this example (one slice with  $\sim 1000$  voxels), only responses in the stimulus condition with correlation values greater than  $r = 0.42$  would be considered significant (black bar and asterisk).

#### ***3.2.4.2. Group analysis***

Individual animal (3 monkeys; 10 imaging separate imaging sessions) were then co-registered in a standard space. At random an imaging session is selected as a reference imaging volume (standard space) and remaining imaging sessions were co-registered (rigid-body transformation) to this standard space using FMRIB's Linear Image Registration Tool (Analysis Group, FMRIB, Oxford, UK). High-resolution anatomical images were used for the image registration. We then apply the same spatial transform to the functional scans,

thus bringing them into the standard space as well. **Figure 3.5** illustrates the co-registration for two animals to the third one (standard space), which brings them all in a standard space. This image co-registration was achieved using FSL's FLIRT algorithm.

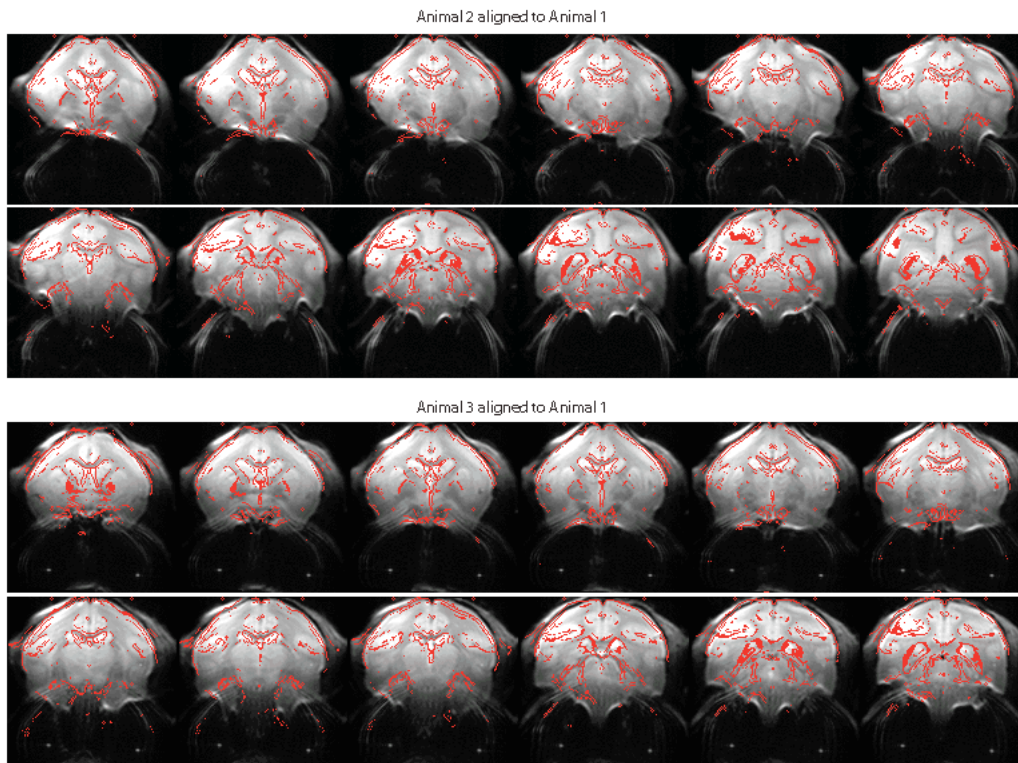


**Figure 3.5. Between sessions and between animal image alignment.** Transforming of images from different animals and imaging sessions to a common space was achieved using FLS's FLIRT algorithm. The figure shows the goodness of fit for the transformation for two animals (Animal 2 and Animal 3) to the third one (Animal 1).

#### ***3.2.4.3. Time series extraction and ROI analysis***

Regions of interest (ROIs) once identified, based on atlas (Gergen & MacLean, 1962) or based on previously reported results in squirrel monkey physiology (Coq et al. 2004; Flaherty and Graybiel 1995; Sur et al. 1982), were then outlined voxel-by-voxel in AFNI, and their time series were extracted. The extracted time series were then signal averaged across voxels (within each ROI) and then across pulse trains to generate an averaged time series of percent change in the BOLD signal for each ROI (**Fig. 3.8**). The peak percent change in the BOLD signal, across time, was then extracted from these thus-averaged traces (**Fig. 3.10**).

#### ***3.2.4.4. Rest state functional connectivity analysis***

Functional connectivity analysis was achieved following the preprocessing and correlation procedures used by Fox and colleagues (Fox et al. 2005; Kahn et al. 2008; Vincent et al. 2010; Vincent et al. 2007; Vincent et al. 2006). Briefly, for each voxel, temporal filtering removed constant offsets and linear trends over each run while retaining frequencies  $< 0.08$  Hz. Data were spatially smoothed using a 2 mm full-width half-maximum Gaussian blur. Sources of spurious or regionally nonspecific variance were removed by regression of nuisance variables including: six parameters obtained by rigid body head motion correction and signals extracted from masks computed on each individual animal that included the whole-brain, the lateral ventricles, and a region centered in the deep cerebral white matter. Temporally shifted versions of these waveforms also were removed

by inclusion of the first temporal derivatives computed by backward differences) in the linear model. This regression procedure removes variance unlikely to represent regionally specific correlations of neuronal origin. Correlation maps for each seed were computed by correlating regional time courses (averaged over all voxels within the seed region) with every voxel in the brain. Correlation maps were converted to z maps using Fisher's r-to-z transformation (Zar 1996). This transformation generates values for each voxel that are approximately normally distributed across individuals in a homogenous population.

### **3.3. Results**

BOLD activation pattern and time courses of specific regions presented in **Figures 3.6–3.12** were from 3 animals (in all six imaging session per animal).

#### **3.3.1. BOLD responses Evoked By Vibro-tactile Stimulation of the Third Digit**

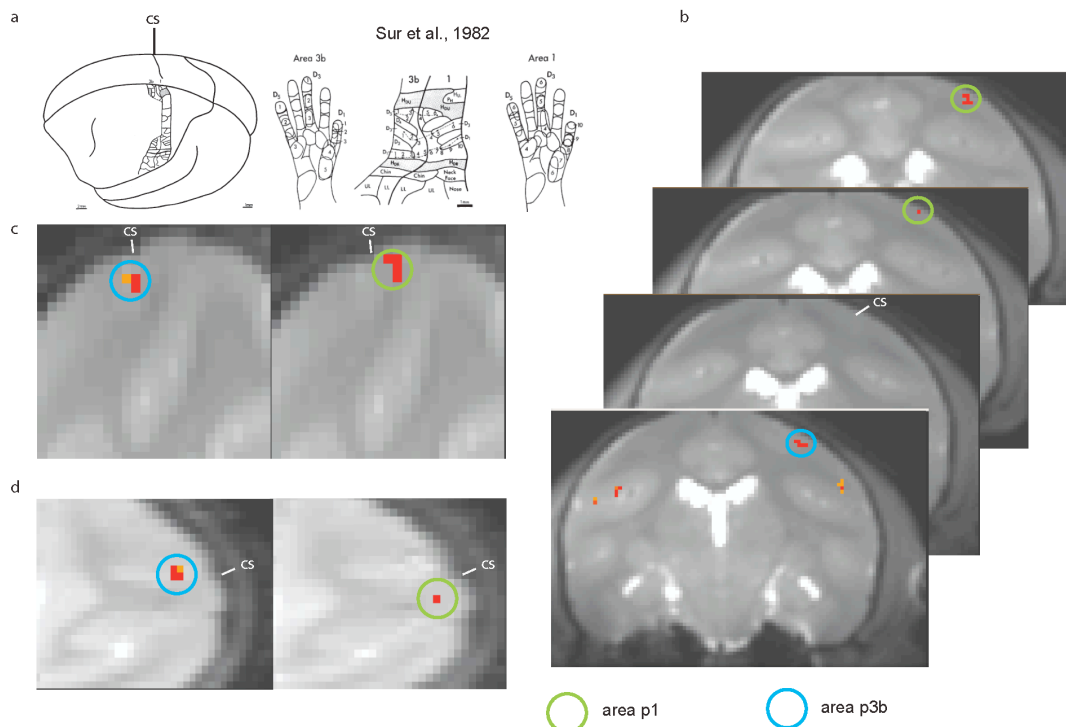


**Figure 3.6. Functional activation in primary somatosensory cortex.** **a**, Schematic figures from Sur et al., 1982 depicting areas 3b and 1 in the squirrel monkeys. **b**, Functional activation in putative area 3b (SI) and area 1 (area p1), superimposed on coronal anatomical images. A characteristic thickening of the cortical mantle is localized to the area SI. The distance between the SI and area p1 is between 2 and 3 mm, as predicted by electrophysiology maps shown in **a**. **c**, Functional activity overlaid on sagittal images showing activation of putative areas SI and area p1. **d**, Functional activity overlaid on transverse images showing activation of areas SI and area p1. **Figures 3.6 b-d**, location of the central sulcus is shown by a white arrow and a blue and a green circle show activation in areas of SI and area p1 respectively.

Consistent with prior electrophysiological studies in New World monkeys (Sur et al. 1982), single-digit vibratory stimulation evoked BOLD responses in SI. **Figure 3.6 b–d** shows an average (across 3 animals at 0.6% isoflurane concentration) of the BOLD response maps in SI during vibrotactile stimulation of the 3<sup>rd</sup> digit. The anterior-posterior and mediolateral location of the BOLD

responses in putative area 3b and area 1, and the distance between them, were consistent with previously published electrophysiology maps in squirrel monkeys (**Fig. 3.6 a** (Sur et al. 1982)). The time course of the percent change in BOLD signal in the area 3b ROI is shown in **Figure. 3.8 a**, *red curve*.

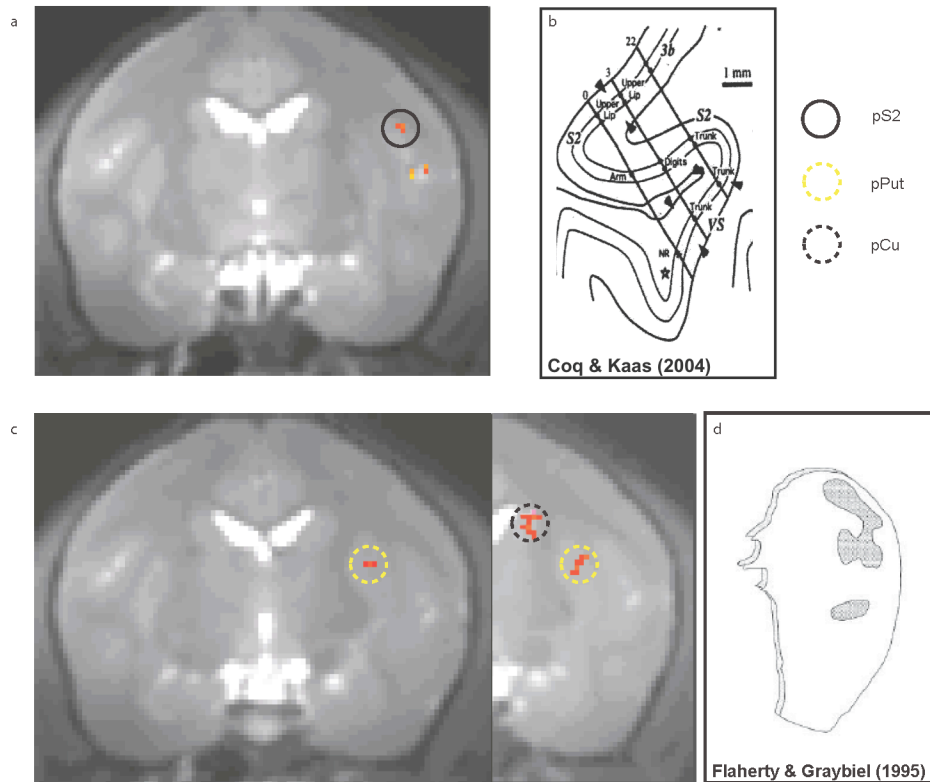


**Figure 3.7. Functional activation in lateral sulcus and basal ganglia areas.**

**a**, An fMRI statistical map of distinct activation foci in the lateral sulcus, the putative ventral somatosensory (pVS), second somatosensory (pSII, black circle) areas. **b**, A schematic from Coq et al., 2004 showing the position of tactile receptive fields and cortical areas in the lateral sulcus of NewWorld Titi monkeys. **c**, An fMRI statistical map of activation in the basal ganglia areas, the putative caudate (pCu, black dashed circle) and putamen (pPut, yellow dashed circle) areas. **d**, Schematic figure from Flaherty et al., 1995 depicting regions (shaded) in putamen with figure representation in squirrel monkeys.

In addition to the BOLD response in SI, vibrotactile stimulation also elicited BOLD responses in other brain regions. **Figure 3.7 a** shows an average (across 3 animals at 0.6% isoflurane concentration) BOLD response map for the region overlying the second somatosensory area (SII). Location of the BOLD responses in putative area SII was consistent with previously published electrophysiology maps in New World monkeys (**Fig. 3.7 b**, (Coq et al. 2004)). The time course of the percent change in BOLD signal in SII ROI is shown in **Figure. 3.8 b**, *red curve*.

In addition to BOLD responses in somatosensory neocortical areas, vibrotactile stimulation elicited BOLD responses in the striatum. **Figure 3.7 c** shows an average (across 3 animals at 0.6% isoflurane concentration) BOLD response map in the caudate and putamen. Location of the BOLD responses in putamen was consistent with electrophysiology maps in squirrel monkeys and with the termination zones of afferent input from SI (**Fig. 3.7 b**, (Flaherty and Graybiel 1995)). Relatively less has previously been reported about the position of caudate tactile activation, and, as described above, there is less evidence for direct SI input (see, (Flaherty and Graybiel 1995) Figure 2). The time courses of the BOLD signal in the caudate and putamen ROIs are shown in **Figure. 3.8 c and d**, *red curves*.

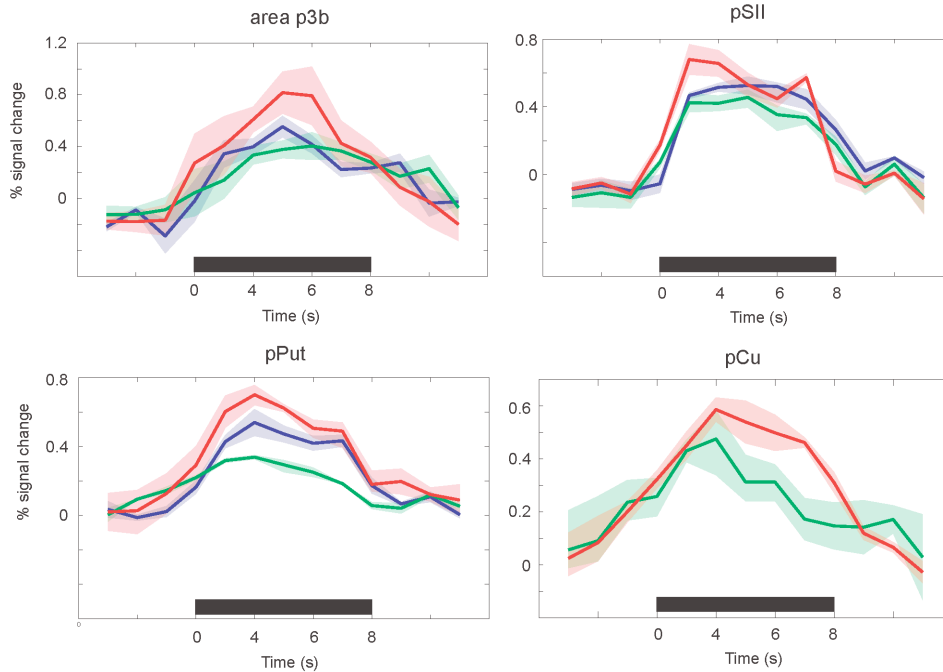


**Figure 3.8. Time courses of the BOLD signal.** Percent change in the BOLD signal, plotted over time, for each ROI of interest (pSI, pS2, pCu and pPut). The BOLD signal was, for this plot, pre-averaged across pulse trains within a scan, across sessions, and across voxels within each specified ROI. Solid lines indicate the average across animals of the percent signal change, for 0.6% isoflurane (red), 1.0% isoflurane (blue) and for 1.4% isoflurane (green); shaded areas indicate the standard error across animals of percent signal change;  $n = 3$  animals.

### 3.3.2. Isoflurane modulates the probability of activation and strength of the BOLD signal

In each experiment, we varied the depth of isoflurane anesthesia to two of three possible levels – 0.6%, 1.0% and 1.4%. Across animals, we collected data from six imaging sessions for each anesthesia depth. To probe the effects of isoflurane anesthesia on the BOLD response and functional connectivity in the somatosensory cortex and the basal ganglia, we analyzed ROIs of voxels that

showed consistent BOLD responses ( $\geq 80\%$  of the times across imaging sessions for 0.6% isoflurane condition) for vibrotactile finger stimulation. The four areas analyzed were area 3b of primary somatosensory cortex (SI), secondary somatosensory cortex (SII), caudate (Cu) and putamen (Put). The time course of the BOLD signal change, averaged across three animals, for all three isoflurane depths are plotted in **Figure 3.8** – red, blue and green curves for 0.6%, 1.0% and 1.4% isoflurane depths respectively.

For the four ROIs (SI, SII, Cu and Pu), the probability of observing a BOLD response across imaging sessions decreased as isoflurane depth increased from 0.6% to 1.4% (**Fig. 3.9**).

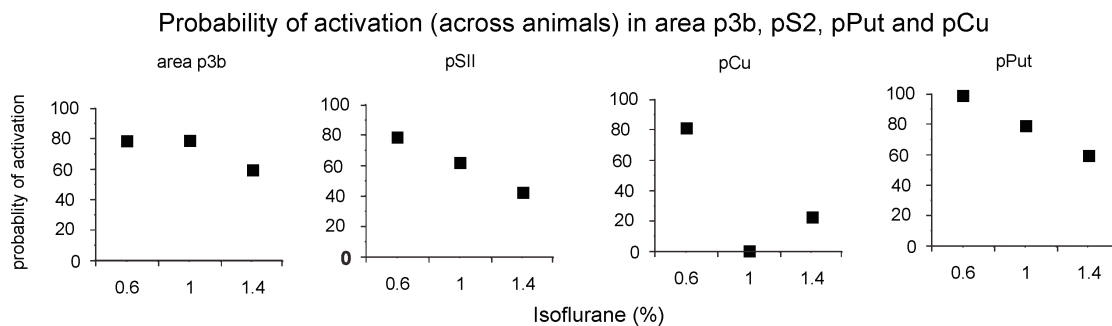


**Figure 3.9. Anesthesia modulation of distributed neural activation patterns.**

Probability of activation in area SI, pSII, pCu and pPut areas for 6 different imaging sessions for a monkey.

We also observed that as the isoflurane depth was increased, there was a decrease in amplitude of the BOLD response for all four ROIs. Despite decreased peak activation values, the shape/temporal dynamics of the BOLD time course did

not visibly change for different depths of isoflurane (**Fig. 3.8**). This finding is consistent with previous studies (Cohen et al. 2002; Nair and Duong 2004). We quantified the peak of the BOLD signal change for each of the imaging session in all three animals, and found that its amplitude was significantly different across regions (**Fig. 3.10**;  $p < 0.0001$ ,  $F(3,24) = 14.32$ , factor of region in a two-way ANOVA of anesthesia level  $\times$  region) and significantly decreased with increased anesthesia ( $p < 0.0001$ ,  $F(2,24) = 35.57$ , factor of anesthesia level in a two-way ANOVA of anesthesia level  $\times$  region; significant interaction between the two factors,  $p = 0.005$ ).

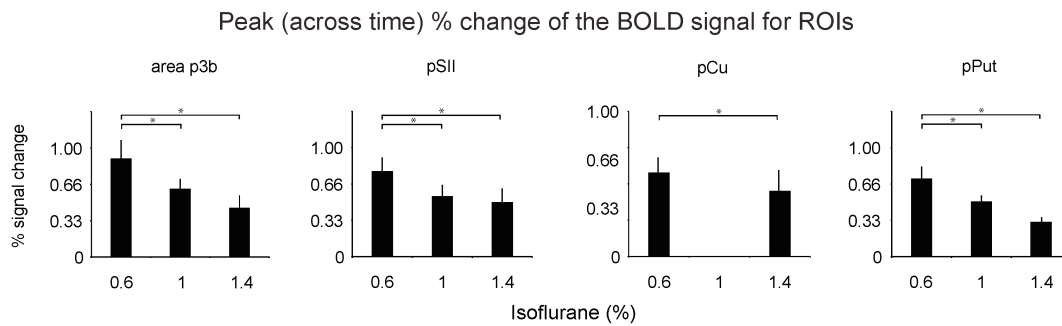


**Figure 3.10. Anesthesia modulation of BOLD signal change in distributed neural activation patterns.** Peak percent change in the BOLD signal for the timecourses plotted in **Figure 3.8**. \*,  $p < 0.0001$ , factor of anesthesia level (two-way ANOVA of anesthesia level  $\times$  region).

The three post-hoc tests of differences in the amplitude of the peak BOLD signal change in all four ROIs revealed that there was a significant drop in the amplitude for 1.0% and 1.4% compared to 0.6% isoflurane depth, however the

amplitude did not significantly change for 1.4% when compared to 1.0% isoflurane depth.

### 3.3.3. Isoflurane depth modulates the resting state correlations between regions that exhibits BOLD response to the stimulation

Along with vibro-tactile stimulation, we also collect scans where we did not stimulate the fingertip but captured all other scan conditions. We analyzed the impact of anesthesia depth on “baseline” scan correlations between the identified tactually-activated areas. A correlation seed placed in SI revealed a significant correlation with caudate, putamen and SII, among other correlations (see **Fig. 3.11** for SI and SII correlation throughout the brain).

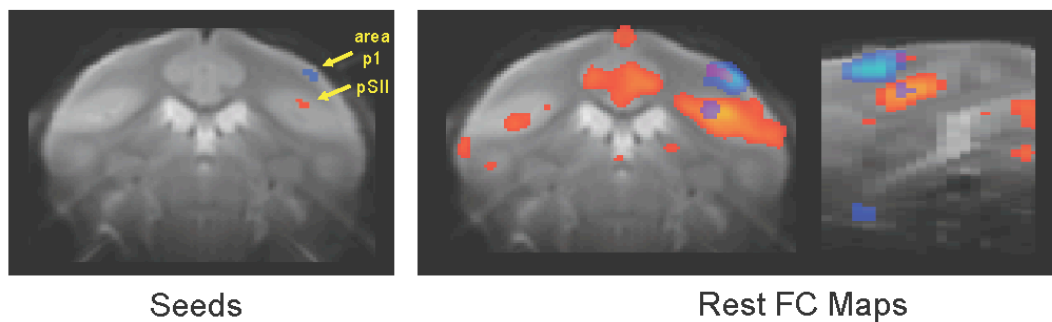


**Figure 3.11. Spontaneous (rest state) functional connectivity analysis.** Fluctuations in the fMRI signal, present at rest, during anesthesia, and across species are thought to reflect spontaneous neural activity, and were extensively used to reveal functional networks. Shown here are two seeds (SI and SII, blue and red respectively) and the map of regions spontaneously connected to those seeds during rest state fMRI scans.

Increasing anesthesia depth reduced the cross-correlation between SI and the other three ROIs (SII, Cu and Pu; **Fig. 3.12**, *top and bottom left*;  $p < 0.0001$ ,  $F(2,24) = 34.91$ , factor of anesthesia level in a two-way ANOVA of anesthesia level  $\times$  region). This result suggests that anesthesia level modulates functional network connectivity. There was a significant difference in the values of cross-correlation between SI and 12 randomly selected voxels in the brain (control ROI, from left-ventral cortex in the anterior most slice; a region that did not show any rest state functional connectivity to SI ROI) and the cross-correlation values for other three pairs (**Fig. 3.12**, *bottom right*,  $p < 0.0001$ ,  $F(2,24) = 17.57$ , main effect of region in a two-way ANOVA of anesthesia level  $\times$  region;  $p < 0.0001$ , Fisher's PLDS, comparison with other pairs of ROIs).

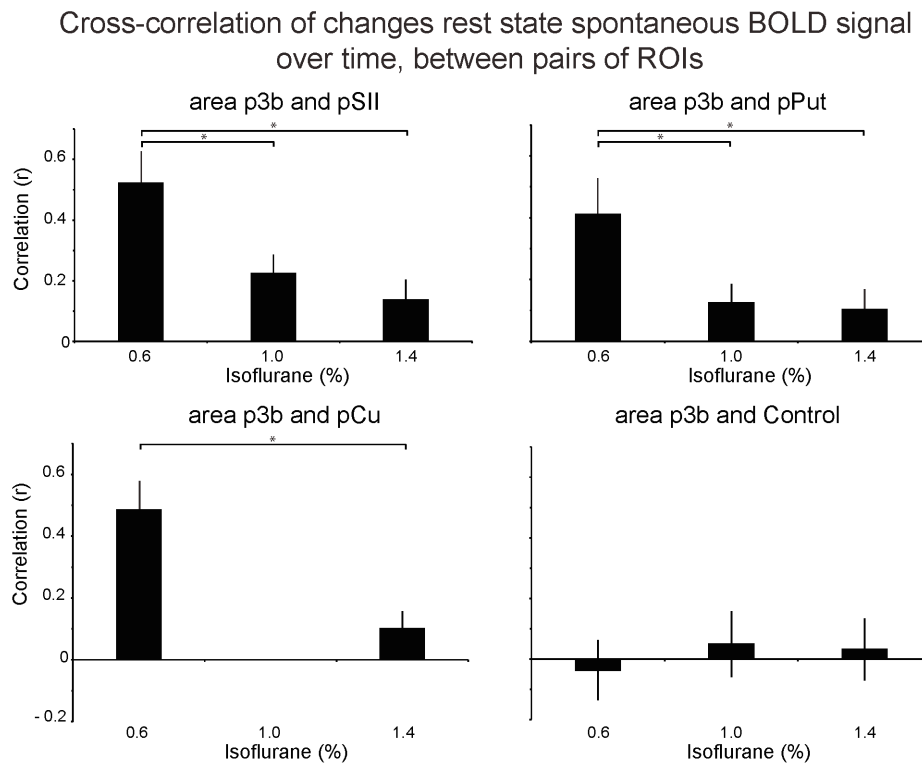


**Figure 3.12. Rest state functional connectivity analysis to assess anesthesia modulation of distributed neural activation patterns.** Rest scan (no tactile stimulation) cross-correlation between area SI and four other ROIs (pSII, pCu, pPut and control) at different anesthesia levels (0.6%, 1.0% and 1.4%). \*,  $p < 0.0001$ , factor of anesthesia level (two-way ANOVA of anesthesia level  $\times$  region).

As with the amplitude of the peak BOLD signal change measure, the three post-hoc tests of difference in the cross-correlation of percent BOLD signal change time course between pairs of ROIs revealed that there was a significant drop in the cross-correlation value for 1.0% and 1.4% when compare to 0.6% isoflurane depth, however the cross-correlation value did not significantly change for 1.4% when compared to 1.0% isoflurane depth.

### **3.4. Discussion**

In this study we used BOLD fMRI to map activation associated with stimulation of the distal fingerpad of the 3<sup>rd</sup> digit in three squirrel monkeys. We found activation in SI, SII and both subsections of striatum, consistent with previously published anatomical (Coq et al. 2004; Flaherty and Graybiel 1995; Sur et al. 1982), optical imaging (Chen et al. 2005; Tommerdahl et al. 2002) and fMRI studies (Chen et al. 2007; Nelson et al. 2006). We used these areas to delineate the effect of isoflurane on the functional connectivity between regions of the somatosensory system that show tactile fMRI activation. In this study three levels of anesthesia (0.6%, 1.0% or 1.4% end-tidal) were presented in six independent imaging sessions in three squirrel monkeys. We observed a dose

dependent effect of isoflurane on fMRI responses in SI and the putamen for the tactile stimulation, but a near loss in the response in caudate nucleus (0/6 sessions for 1.0% and 1/6 sessions for 1.4% isoflurane depth). We also observed that while the impact of isoflurane on sensory-driven activation of SI and putamen was modest (responses in > 60% of the sessions at 1.4%), the connectivity between these regions was significantly decreased at increased isoflurane levels.

Isoflurane anesthetic agent is widely used in animal fMRI studies to reduce motion artifacts, immobilization stress, and to eliminate the need for physical acclimation to the experimental apparatus (King et al. 2005; Lahti et al. 1998; Lukasik and Gillies 2003; Masamoto et al. 2007; Sicard et al. 2003). Isoflurane also provides a stable condition for the animals, allows easy control of the targeted depth of anesthesia, and can be used repeatedly for survival experiments in the same animal (King et al. 2005; Lahti et al. 1998; Lukasik and Gillies 2003; Masamoto et al. 2007; Sicard et al. 2003). However, previous studies have shown that isoflurane has confounding effects on excitatory neurotransmission (Detari et al. 1999; Detsch et al. 2002; Hentschke et al. 2005; Moruzzi and Magoun 1995; Puil and el-Beheiry 1990; Steriade and Amzica 1996), neurovascular coupling (Masamoto et al. 2009b), cerebral blood flow changes (Brevard et al. 2003; Sicard et al. 2003), resting membrane potential (Felisberti et al. 1997), and calcium currents in neocortical neurons (Puil et al. 1994). Isoflurane is thought to suppress neural activity by multiple mechanisms, and this effect becomes more pronounced as the concentration of isoflurane is

increased (Joksovic and Todorovic 2010; Langmoen et al. 1995; Liachenko et al. 1999; Ries and Puil 1999; Wakamori et al. 1991).

Isoflurane is also shown to preferentially target cortical information processing by action on subcortical structures (Alkire et al. 2000; Fiset et al. 1999; Nelson et al. 2002). Isoflurane is thought to impact excitatory and inhibitory input to the thalamic nucleus (Alkire et al. 2000; Detsch et al. 2002; Ries and Puil 1999). It is also widely reported that anesthesia suppresses stimulus-induced activity in the striatum (West 1998) and blocks connectivity between basal ganglia and primary somatosensory cortex (Hutchison et al. 2010; Mhuircheartaigh et al. 2010) for a review see (Nallasamy and Tsao 2011)). However, a recent study by Mowery et al., (Mowery et al. 2011) found vibrissa-driven striatal responses in lightly anesthetized (0.5% –1.0% isoflurane) rats, in agreement with our observation that anesthetic does not necessarily block striatal activation.

Isoflurane is widely used in fMRI and other imaging methods that rely on hemodynamic contrast mechanisms. The role that isoflurane anesthesia has on local versus global network dynamics, and on the coupling of these neural signals to blood flow, is still being delineated (Corfield et al. 2001; Matta et al. 1999; Tsurugizawa et al. 2010). While isoflurane may have several non-specific effects that could potentially prevent detection of BOLD signals, the relatively robust activation of both cortical (SI) and subcortical (putamen) structures at the higher levels employed here suggests that the failure to see activation in caudate with increasing depth is not simply a non-specific effect of administration.

Overall our study is in agreement several other previously published studies that suggest a dose-dependent effect of anesthesia on the functional connectivity and excitability of neurons in the brain. Our study specifically studies the functional connection between somatosensory cortex and the basal ganglia region, as this connection has a central role in several important basal ganglia tasks. We find that state dependent changes, here modeled through anesthesia change, affect the excitability of somatosensory regions and functional connectivity between somatosensory cortex and the basal ganglia region.



## **Chapter 4. Opto-fMRI: Integration of Optical Neural Control and Functional Magnetic Resonance Imaging**

This chapter is adapted from:

Published conference proceedings; Mitul Desai, Jacob Bernstein, Hisham Atallah, Itamar Kahn, Christopher I. Moore, Nancy Kopell, Ann M. Graybiel, Edward S. Boyden; “Integration of optical neural control and high-field fMRI: Towards systematic exploration of functional neural dynamics with Opto-fMRI”, 39<sup>th</sup> annual Society for Neuroscience meeting, Chicago, IL.

A published paper; Mitul Desai.\*, Itamar Kahn.\*, Ulf Knoblich, Jacob Bernstein, Hisham Atallah, Amy Yang, Nancy Kopell, Randy L. Buckner, Ann M. Graybiel, Christopher I. Moore C, & Edward S. Boyden; “Mapping Brain Networks in Awake Mice Using Combined Optical Neural Control and fMRI”, *Journal of Neurophysiology* 2011 Mar;105(3):1393-405.

\* These authors contributed equally

### **4.1. Introduction**

Functional magnetic resonance imaging (fMRI) is a powerful approach for measuring activity distributed throughout the brain at a relatively high spatial resolution. fMRI is also non-invasive, making it appropriate for longitudinal studies monitoring temporally extended processes such as development, learning, and disease progression and treatment (Tombari et al. 2004). As we discussed in **Chapter 2**, when combined with other modalities that allow causal control of specific region, fMRI allows us to track the consequence of perturbing one set of region on other regions throughout the brain. This has been successfully shown in studies that combine fMRI with electrical microstimulation (Ekstrom et al. 2008; Logothetis et al. 2010; Moeller et al. 2008; Tolias et al. 2005). However, there is

couple of drawbacks to this technique. One, this technique is non-specific to the cell type and can often be non-specific to a region, and second this technique is invasive and not suitable for chronic and repeated experimentation.

Optical neural control methods, using light-driven proteins such as the light-gated ion channel channelrhodopsin-2 (ChR2) targeted to specific cells, allow the temporally-precise activation and silencing of specific neural pathways and cell classes in the brain, thus enabling assessment of the causal influence of defined neural activity patterns upon connected neural networks (Boyden et al. 2005a; Chow et al. 2010; Han and Boyden 2007a; Petreanu et al. 2009; Zhang et al. 2007b). The combination of optogenetic control with fMRI would open up the ability to assess the brain-wide influence of a specific set of neural circuit elements, and enable explorations of how that functional map is modulated by development, learning, or pathology. Accordingly, we have developed and optimized such a combined methodology, which we call opto-fMRI.

We here describe the key technical approaches, including the critical hardware design choices, surgical strategies, MRI pulse sequences, and data analysis methods required to combine small-animal fMRI and optical control of defined neural networks in the mouse brain, thus enabling the mapping of the patterns of activity in regions connected to a defined cortical neuron set, in a genetic model organism of great importance for furthering health. We demonstrate that opto-fMRI elicits clear, repeatable, distributed patterns of network activity following optical activation of excitatory neurons in primary somatosensory barrel cortex (SI-BF) in mice, with high spatial resolution,

sufficient to resolve sub-columnar activity. We further show that opto-fMRI can be used to analyze the network activity related to a defined input. We anticipate that opto-fMRI will find many uses in the mapping of functional neural connectivity throughout neuroscience, and provide a bridge between the increasingly popular use of optical methods to probe causal neural circuit functions in animals, and the complexity of human behavior and subjective experience as commonly probed with fMRI.

## **4.2. Methods**

### **4.2.1. Animals and surgery**

All procedures were conducted in accordance with National Institutes of Health guidelines and with the approval of the MIT Committee on Animal Care. 6 wild-type mice (C57BL/6, purchased from Charles River), and 11 transgenic ChR2 mice (line 18, stock 007612, strain B6.Cg-Tg (Thy1-COP4/EYFP)18Gfng/J from Jackson Labs, Bar Harbor, ME; bred in-house with wild-type mice) were used. A summary of animals used for the different experiments throughout this study is presented in **Table 4.1**.

Experiment type	Mice			fMRI parameters		Referenced in...
	Animal type	Number of animals	Animal IDs	Voxel resolution	Number of slices	
<b>Opto-fMRI</b>						
0.5% isoflurane	Virally injected wild types	3	CamKII-ChR2-A thru C	200 $\mu\text{m}$ $\times$ 200 $\mu\text{m}$ $\times$ 500 $\mu\text{m}$	10	Fig. 4.4 A & C, Fig. 4.5 A & E, and Fig 4.7
	Thy1-ChR2 mice	3	Thy1-ChR2-E thru G	100 $\mu\text{m}$ $\times$ 100 $\mu\text{m}$ $\times$ 500 $\mu\text{m}$	5	Fig. 4.9 A - C
	Un-injected wild types	2	WT-noChR2-A and B	200 $\mu\text{m}$ $\times$ 200 $\mu\text{m}$ $\times$ 500 $\mu\text{m}$	10	Fig. 4.4 B & C, Fig. 4. 5 B & E, and Fig 4.7
	Thy1-ChR2 mice	4	Thy1-ChR2-A thru D	200 $\mu\text{m}$ $\times$ 200 $\mu\text{m}$ $\times$ 500 $\mu\text{m}$	10	Fig. 4.5 C & E, Fig. 4.6., and Fig. 4. 7
<b>Electrophysiology experiment</b>						
LFP and MUA recordings for optogenetic stimulation	Thy1-ChR2 mice	2	Thy1-ChR2-H and I	NA	NA	Fig. 4.9 D - F
<b>Control fMRI</b>						
Head post and pulse sequence EPI distortion	Un-injected wild types	1	WT-noChR2-C	200 $\mu\text{m}$ $\times$ 200 $\mu\text{m}$ $\times$ 500 $\mu\text{m}$	10	Fig. 4.2 B and C
Yellow light optical and electrical paw stimulation	Thy1-ChR2 mice	1	Thy1-ChR2-J	200 $\mu\text{m}$ $\times$ 200 $\mu\text{m}$ $\times$ 500 $\mu\text{m}$	10	Fig. 4.3
physiological measurements	Thy1-ChR2 mice	1	Thy1-ChR2-K	200 $\mu\text{m}$ $\times$ 200 $\mu\text{m}$ $\times$ 500 $\mu\text{m}$	10	Table 4.2

**Table 4.1. Summary of animal usage and fMRI parameters for different experiments throughout this chapter.** The table presents a summary of all the animals that are used throughout this study and the kind of experiments they are used for. The summary also presents the fMRI parameters (resolution and number of slices) employed for a specific experiment and the figure it represents in this chapter.

For viral injection, 3 of the wild-type mice were first anesthetized with isoflurane (~1-2% mixed with oxygen), then craniotomized (~0.5 mm wide) and injected with lentivirus encoding for ChR2- green florescent protein (GFP) under the  $\alpha\text{CaMKII}$  promoter (FCK-ChR2-GFP, 1  $\mu\text{L}$ , as utilized in (Han et al. 2009), over a 30-minute period, into the left SI barrel field). Injections were performed using an injection pump (Quintessential Stereotaxic Injector, Stoelting Co., Wood Dale, IL) driving a 10  $\mu\text{L}$  Hamilton syringe connected to a glass micropipette

(100  $\mu\text{m}$  tip) via polyethylene tubing. The system was filled with mineral oil. The coordinates of viral injection relative to bregma were as follows: 1.0 mm posterior, 3 mm lateral, 0.7 mm ventral.

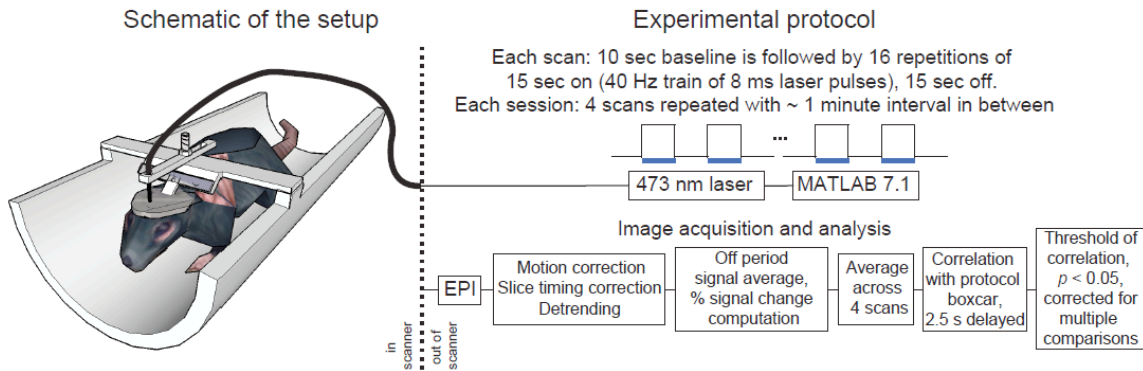


**Figure 4.1. Design of ‘Opto-fMRI’ setup. Left, schematic of Opto-fMRI setup for measuring distributed neural activation patterns due to optical perturbation of an opsin-expressing cell type.** Shown is a mouse bearing an MRI-compatible head post, attached to a head post holder, which is in turn attached to a cradle with RF coil attached (surrounding the head post; not shown for clarity; see **Fig. 4.2 A** for photograph of the RF coil). An optical fiber holder orients an optical fiber (200 microns wide) into the craniotomy, above the cortical surface. The cradle is inserted into a 9.4T MRI scanner. *Top right*, boxcar-pattern protocol for delivery of a series of 15 second periods (indicated by blue bars, in this and subsequent figures) of 40 Hz pulse trains of 8 ms blue laser pulses (473 nm, 10-15 mW unless otherwise indicated), driven by a PC running MATLAB. *Bottom right*, images (EPIs) are motion-corrected, slice-timing corrected, detrended, converted into percent signal change by subtracting the average signal from the “laser off” periods, and averaged across scans. Then, the percent signal change is correlated, voxel-wise, to the boxcar pattern of the protocol, shifted forwards by 2.5 seconds to compensate for the BOLD delay, in order to determine the voxels that are significantly changing. Significance was judged with respect to a Monte Carlo simulation, as having a multiple comparisons corrected p value of 0.05 for the boxcar correlation (uncorrected p-value < 0.005;  $r > 0.83$ ; see **Fig. 4.4 C**)

For opto-fMRI, animals were surgically implanted – with a headpost (**Fig. 4.1**) atop their skulls using dental cement (C&B-Metabond, Parkell, Inc.). The headpost (weighing ~250 mg) and the headpost holder were custom made from Accura 55 plastic, an ABS-like plastic (**Fig. 4.1**). For virally injected animals (n = 3), the headpost surgery was done at least three weeks after the surgery for viral injection. For Thy1-ChR2 mice, the kind of craniotomy performed depended on the experiment: in four Thy1-ChR2 mice (**Fig. 4.6** and **Fig. 4.7**), a small craniotomy (~ 0.5 mm) was also drilled at this time through the skull over SI to allow positioning of the optical fiber above the cortical surface; in five other Thy1-ChR2 mice used for near-microscopic resolution opto-fMRI (**Fig. 4.9**) and for three control experiments (a blood pressure control, a yellow light control, and a paw stimulation control), instead of a craniotomy over SI, the skull was thinned to half of its thickness, to reduce distortion even further for high-resolution imaging. At the end of each surgery, exposed skull (except for that which was thinned) was covered with a thin and uniform layer of dental cement to minimize echo-planar image (EPI) distortion caused by susceptibility mismatch in fMRI. The reason for this final dental cement step was to reduce distortion: **Figure 4.2 B** shows a pair of images (each maximum-intensity projected across 4 coronal slices) from a mouse, which shows the effect of a uniform layer of Metabond on the EPI distortion artifact. Specifically, this headposted wild-type mouse was imaged (spin-echo EPI [SE-EPI]) without any Metabond (**Fig. 4.2 Bi**) and then reimaged after applying a thin and uniform layer of Metabond (**Fig. 4.2 Bii**), showing in the latter case a reduction in artifact.

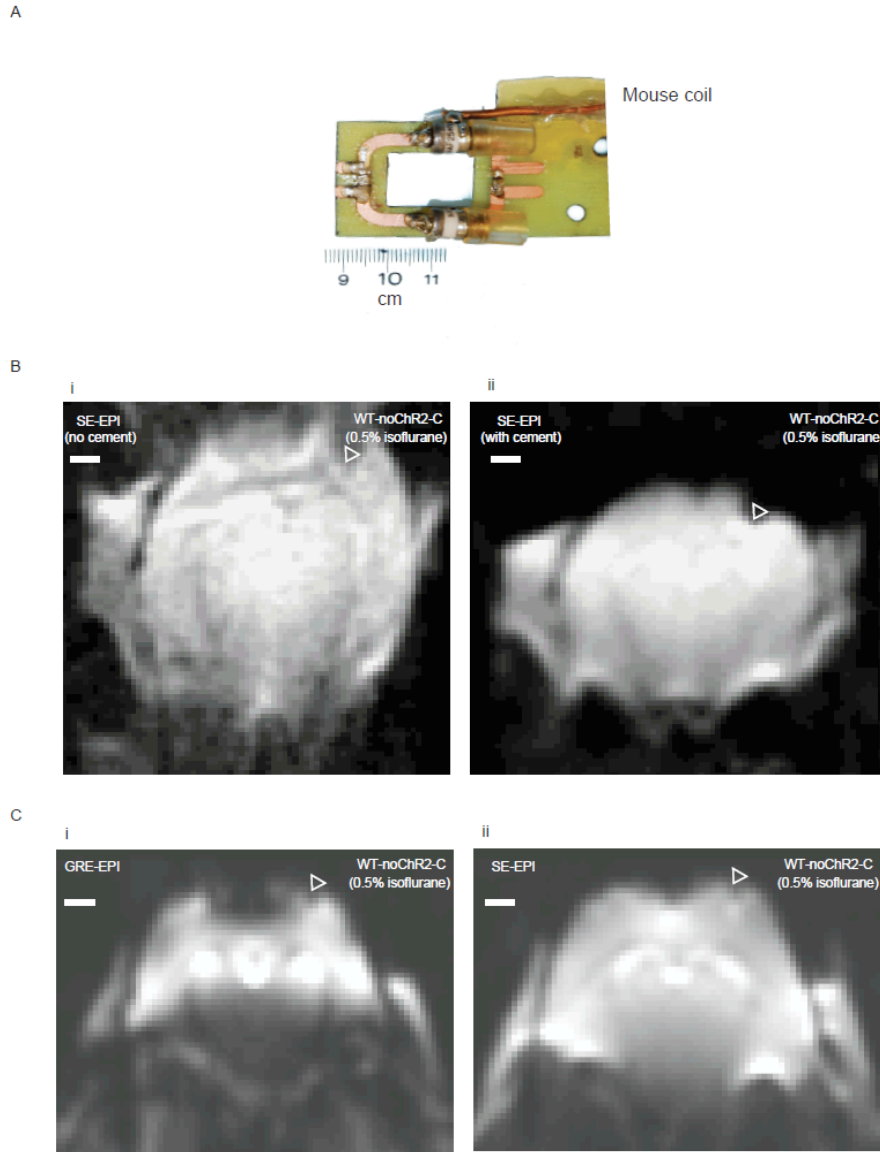


**Figure 4.2. RF coil design, cement usage, and EPI distortion elimination. A,** Custom-built RF transmit-receive surface coils used for opto-fMRI. **B,** Single-slice images obtained via SE-EPI, in an anesthetized animal, without (i) and with (ii) a thin and uniform layer of Metabond coating the skull. Images were collected at  $200\ \mu\text{m} \times 200\ \mu\text{m} \times 500\ \mu\text{m}$  voxel resolution, and maximum-intensity projected across 4 coronal slices (2 mm). Scale bar in **B** and **C** is 1 mm. **C,** Single-scan images of the same headposted mouse shown in **B**, with cement already applied, obtained via GRE-EPI (i) and SE-EPI (ii). Each image was acquired at  $200\ \mu\text{m} \times 200\ \mu\text{m} \times 500\ \mu\text{m}$ . White open triangle in **B** and **C** indicates position of the optical fiber tip; the laser was left unilluminated for these experiments.

#### 4.2.2. Opto-fMRI: Experimental setup and protocol

Data were acquired on a 9.4 Tesla (Bruker BioSpin MRI GmbH, Ettlingen, Germany), 20 cm inner diameter, horizontal bore magnet. Custom-built radio frequency (RF) transmit-receive surface coils, specifically designed for mouse and rat brain, were used for imaging (**Fig. 4.2 A**). Functional data were acquired using a SE-EPI in the coronal orientation; we compared this protocol to gradient-echo EPI (GRE-EPI) in **Figure 4.2 C**, in an acute (0.5% isoflurane anesthetized) experiment on a wild-type mouse, and found GRE-EPI to be more susceptible to distortion artifacts than SE-EPI.

Opto-fMRI experiments were performed on 3 virally injected wild-type mice, 9 Thy1-ChR2 mice, and 2 wild-type mice. The 3 virally injected mice were imaged at 0.5% isoflurane for laser power and negative BOLD controls (**Fig. 4.4 C, Fig. 4.5 B**).

For opto-fMRI imaging, animals were initially anesthetized with isoflurane (2-3% in oxygen). Breathing rate (Small Animal Monitoring 1025, SA Instruments, Stony Brook, NY) and end-tidal expired isoflurane (V9004 Capnograph Series, Surgivet, Waukesha, WI) were continuously monitored during the imaging experiment. Anesthetized animals were placed on a custom built G-10 fiberglass MRI cradle in a position that approximated their final position, and then radio frequency (RF) transmit-receive coil (single copper loops, milled out from a copper plated 1/16" epoxy material (FR-4, T-Tech, Inc., Norcross, GA); shown in **Fig. 4.2 A**) was then positioned over the animals' heads.

The animals were then attached by their headpost to their headpost holder, which was then affixed the MRI cradle. A 200 mm optical fiber (Ocean Optics, Dunedin, FL) attached to an adjustable optical fiber holder was then oriented towards the target (e.g., into the craniotomy), passing through the RF coil. The MRI cradle was then slid into the magnet bore. The cradle was then locked to the stage so as to position the head of the animal in the center of the magnet bore. The anesthesia level for these animals was maintained, as indicated by end-tidal isoflurane level (see below), at 0.5%.

Functional images were collected at a voxel resolution of 200 mm x 200 mm x 500 mm (10 slices; mouse images in **Fig. 4.2–4.4**, **Figs. 4.6 – 4.8**, **Fig. 4.5 A–C**, and **Fig. 4.5 E**), or 100 mm x 100 mm x 500 mm (5 slices; **Fig. 4.9 A–C**, and **Fig. 4.5 D**). For simplicity, a summary of fMRI parameters used for different experiments throughout this study is presented in **Table 4.1**. For the high-resolution imaging sessions (that is, less than  $150\ \mu\text{m} \times 150\ \mu\text{m} \times 500\ \mu\text{m}$  in voxel size), we took advantage of the speed and strength of our gradient coils to frame the volume imaged with four saturation slices (e.g., **Fig. 4.9**), thus avoiding wrap-around artifacts (Wang et al. 2004; Wilm et al. 2007). Functional data were acquired using a SE-EPI; 2.5 s repetition time ( $T_R$ ) and 25 ms Echo time ( $T_E$ ). High-resolution  $T_2$ -weighted anatomical images (78 mm x 78 mm x 500 mm) were acquired using a rapid acquisition process with relaxation enhancement (RARE) sequence in the coronal orientation, after physiological data acquisition was complete.

The optical protocol used for opto-fMRI in this paper (although obviously many variants are possible for this aspect of opto-fMRI) was a 10 s baseline period of darkness followed by 16 repetitions of 15 s on, 15 s off periods of 40 Hz trains of 8 ms laser pulses (the boxcar pattern shown in **Fig. 4.1**, *top right*), applied to the primary somatosensory cortex (SI). Light was delivered with a 473 nm blue laser (Shanghai Dream Lasers, Shanghai, China), placed outside the magnet room and coupled to a 200 micron optical fiber (~5 m in length), which was passed inside the magnet room through a small duct. A MATLAB program and a USB Data Acquisition Modules (Cole-Parmer, Vernon Hills, IL) was used to control the laser to deliver the protocol boxcar pattern (**Fig. 4.1**, *top right*).

For mapping experiments in the 5 awake mice (and the 0.7% isoflurane states), and for the near-microscopic opto-fMRI experiments, the laser power out the fiber was 5 mW-10 mW (fiber tip irradiance, 150-300 mW/mm<sup>2</sup>). For control experiments, 3 virally-injected mice, 3 Thy1-ChR2 mice, and two wild-type mice, we used 10-15 mW laser power; these last two wild-type were exposed to 25-30 mW as controls.

### **4.2.3. Control experiments**

Three control experiments were performed on two 0.5% isoflurane-anesthetized Thy1-ChR2 mice to examine (1) blood pressure dependence on SI illumination, (2) fMRI response to yellow light, and (3) fMRI response to paw stimulation. For the first of these control mice, blood pressure, heart rate, body temperature, and respiration rate were continuously monitored (sampling rate of 5

s; Advisor, Vital Signs Monitor, Surgivet, Waukesha, WI) throughout the length of an opto-fMRI experiment, on one mouse, to observe the effect of laser stimulation on the animal's physiology. The femoral artery was cannulated with polyethylene tubing (ID 0.28 mm, OD 0.61 mm) to measure blood pressure and heart rate. The mean arterial blood pressure (mabp), mean heart rate (hr), mean temperature (t), and mean breathing rates (br) were  $89.4 \pm 8.7$  mm Hg,  $577.4 \pm 12.8$  beats per minute,  $35.8 \pm 1.5$  °C and  $98.7 \pm 3.7$  breaths per minute respectively, during the on periods (mean  $\pm$  std. error; taken across 64 on periods, in 4 scans of 16 on periods each), and  $89.3 \pm 8.5$  mm Hg,  $576.5 \pm 15.7$  beats per minute,  $35.8 \pm 1.0$  °C and  $98.9 \pm 3.4$  breaths per minute during the off periods (**Table 4.2**). On and off were not significantly different for any of these measures (paired *t*-test, *n* = 64 on periods, each followed by an off period;  $p_{\text{mabp}} > 0.90$ ;  $p_{\text{hr}} > 0.90$ ;  $p_{\text{t}} > 0.55$ ;  $p_{\text{br}} > 0.85$ ).

	MABP	Heart Rate	Temp	RR
Blue laser ON periods	89.35 $\pm$ 8.68	576.93 $\pm$ 12.8	35.8 $\pm$ 1.48	98.78 $\pm$ 3.68
Blue laser OFF periods	89.29 $\pm$ 8.52	576.48 $\pm$ 15.7	35.8 $\pm$ 0.98	98.86 $\pm$ 3.98

**Table 4.2. Control experiment in 0.5% isoflurane-anesthetized Thy1-ChR2 to examine blood pressure dependence on SI illumination.** The mean arterial blood pressure (MABP), mean Heart Rate, mean Temperature, and mean Breathing Rates (RR), during laser ON and laser OFF periods.

For the second mouse, the effect of paw stimulation was measured (15 s, 40 Hz, 3 ms pulse duration, 3 mA-amplitude pulse current delivery) on the BOLD

signal, finding the % change in SI to be, at its temporal peak, a 2.2% increase (at 7.5 s after stimulus onset), with a shape that matches the HRF with  $p < 0.0005$  (Fig. 4.3 A; least squares linear regression analysis, comparing the canonical HRF with each of the four scans within the session;  $R^2 = 0.9627$ ,  $F = 32.93$ ). In this same mouse, we then measured the effect of yellow light (593 nm, 5 mW) on the fMRI signal and found no induced BOLD signal changes - positive or negative (Fig 4.3 B).

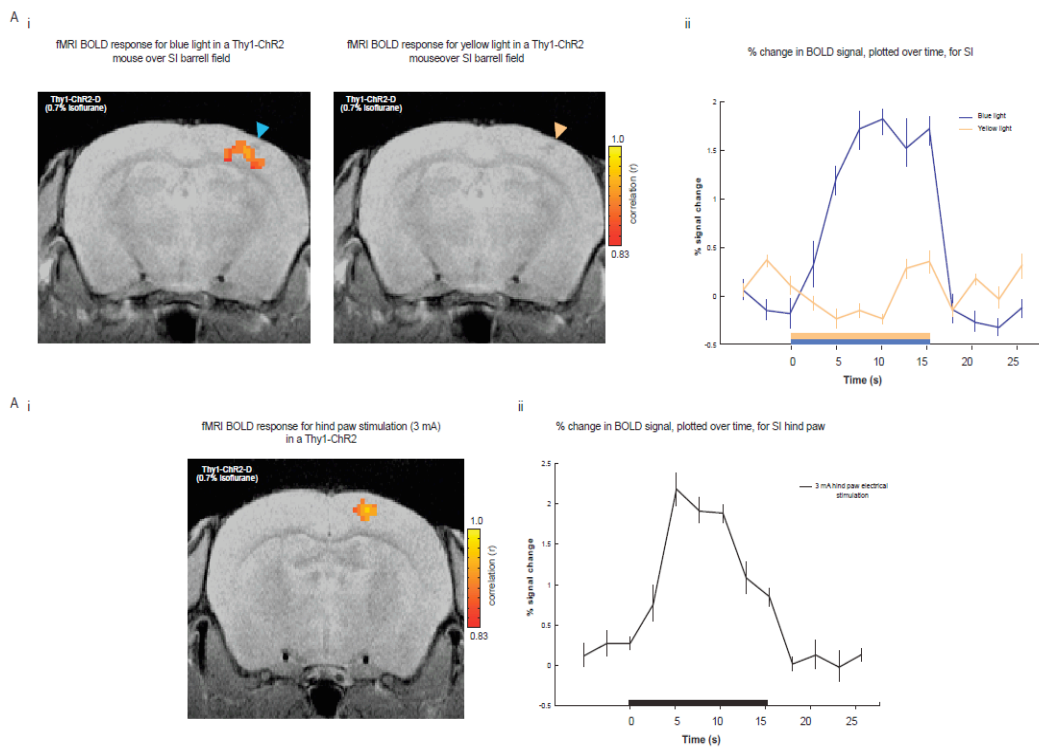


**Figure 4.3. fMRI BOLD response in a Thy1-ChR2 mouse for blue and yellow laser light illumination over SI barrel field and undergoing right hind paw stimulation. Ai, fMRI BOLD response in Thy1-ChR2 mice for blue laser light illumination over SI barrel field. Aii, % change in BOLD signal, plotted over time, for SI barrel field for blue and yellow laser light illumination. The BOLD signal timecourse was averaged across the 16 pulse trains within a scan, for 4 such scans, and across all the voxels that show significant increase in BOLD signal for the blue light stimulation. Error bars are the standard errors for 4 scans. Bi, fMRI**

BOLD response, plotted as correlation image over a T1 anatomical image, in a Thy1-ChR2 mouse for an electrical stimulation (3 mA) of the right hind paw. **Bii**, % change in BOLD signal, plotted over time, for the voxels in the cortex (SI, hind paw region) showing significant increase in the BOLD signal. The BOLD signal time course was averaged across the delivery of 16 electrical pulse trains (40 Hz stimulation for 15 s, shown as a black bar) within a scan, for 4 such scans, and across all the voxels that show significant increase in BOLD signal. Error bars are the standard errors across 4 scans.

Control experiments investigating putative negative BOLD were conducted using an MRI phantom of 3% agarose in saline containing a LEGO brick (**Fig. 4.5 E**). MRI water phantom water (**Fig. 4.8**), in a 50 mL centrifuge tube, was used to characterize RF coil's SNR properties.

#### **4.2.4. Opto-fMRI: data analysis**

The analysis pipeline is outlined in the lower right hand part of **Figure 4.1**. Boxcar correlation maps for EPI functional data were generated using AFNI(Cox 1996; Nelson et al. 2006) (NIH, <http://afni.nimh.nih.gov/afni>, Bethesda, MD) and MATLAB (The Mathworks, Natick, MA). EPI functional data were motion corrected in all three spatial dimensions, but no spatial smoothing or undistortion was performed (to preserve full resolution). The images were slice-time corrected and detrended, as is standard for EPI scanning (Lindquist 2008; Smith et al. 1999). Percent signal change was computed by subtracting, from each voxel's BOLD time series, the temporal average of all off periods for all scans in a session, and then dividing by the average of the signal

across all off periods. We performed 4 scans per session, and percent signal change was averaged across scans in a session unless otherwise indicated.

To determine which voxels had significant increases or decreases in BOLD signal, a voxel-wise time series correlation of the percent signal change was performed, as determined above, with the protocol boxcar (**Fig 4.1, top right**), delayed by one repetition time ( $T_R$ ; 2.5 s) to compensate for the BOLD response time lag (Cox 1996; Nelson et al. 2006); we label this analysis “boxcar correlation” in the text. Activation in a region was deemed significant if a cluster (here used in the fMRI sense of the word) of at least 6 contiguous voxels had correlation  $p$ -values at an uncorrected threshold of  $p < 0.005$ . This cluster size of 6 and this uncorrected  $p$ -value threshold of 0.005 were objectively chosen via Monte Carlo simulations performed in AFNI (family-wise error correction using ‘AlphaSim’ program), to result in a multiple comparisons corrected type I error of 5 %, appropriate for the performance of statistics for individual voxels taken throughout the entire imaging volume (Forman et al. 1995a; Xiong et al. 1995b). The parameters used for the four Monte Carlo simulations (one for each scanning resolution utilized) were as follows: number of voxels,  $100 \times 100 \times$  number of slices; voxel size (functional resolution); size of smoothing filter (same as voxel size); number of Monte Carlo iterations, 10,000.

#### **4.2.5. Region of interest (ROI) identification and cross-registration**

In order to identify activated regions, for each individual fMRI session the statistical map (that is, the correlation of BOLD percent signal change to the

boxcar pattern, described above) was overlaid on the EPI average image for that session, for visualization. Images were cross-registered using EPI-assessed landmarks: the center of the medial ventricle in the EPI slice in which the craniotomy distortion is visibly maximal (i.e., because the craniotomy and fiber are in that slice) was set to (0, 0, 0) in the plot (**Fig. 4.6 B, C and D**).

For each imaging session, the coordinate location of the voxel with peak boxcar correlation, in each contiguous set of significantly-activated voxels, was identified. Using k-means clustering we clustered (note: the term ‘cluster’ is now being used in the k-means sense, not in the fMRI pre-processing sense used in the previous section of the **Methods**) the coordinate locations of the peak-correlation voxels thus identified. We adapted an algorithm (Duda et al. 2000) to perform the k-means analysis in an unsupervised fashion, following the steps listed below, starting with  $C = 1$ :

- performing k-means clustering with  $C$  clusters;
- computing for each resultant cluster the within-cluster sum-of-squares position variance – that is, the sum, over all peak-correlation voxels in a cluster, of the squared distance  $|(\text{coordinate of the peak-correlation voxel}) - (\text{mean coordinate of all peak-correlation voxels within the cluster})|^2$ ;
- comparing the  $C$  sum-of-squares variances thus computed, using a  $t$ -test, to those obtained when k-means was run with  $C+1$  clusters.

We iterated this process, increasing  $C$  by 1 each time until the  $p$ -value of this  $t$ -test was no longer significant ( $p < 0.05$ ); then, the number of clusters used for  $k$ -means was set to  $C$ .

We used a second method, which we call the atlas-comparison method. To provide candidate names for these emergent clusters, clusters were identified based on the comparison of coordinate locations defined on EPI slices to precise dorsoventral, anteroposterior, and mediolateral coordinates on corresponding mouse atlas section (Paxinos and Watson, 1998), aided by knowledge of the circuit connectivity (the names SI, SII, M1, and C-S1 were chosen based upon sets of contiguous significant voxels near each of these landmarks, **Figure 4.6 C**, as well as upon knowledge of the circuit connectivity of S1). The EPI slice comparison to the atlas was performed visually, based upon rigorous anatomical landmarks and properties visible in EPI slices (e.g., the mid-line, medial ventricle, hippocampus, cortical thickness, and brain width and height). We used this method throughout the main text of this chapter, the clusters were similar to those obtained by the  $k$ -means approach: 90% of the peak correlation voxels within a single  $k$ -means identified cluster, were also found within a single atlas-defined cluster.

For 3-D visualization, T2-anatomical images were rendered in 3D using AFNI and overlaid with colored points corresponding to the peak-correlated voxels for each ROI, as cross-registered and determined above (**Fig. 4.6 D**).

#### **4.2.6. Time series extraction and ROI analysis**

Identified ROIs (SI, C-SI, SII and M1), as identified by the atlas-comparison method above, were outlined voxel-by-voxel in AFNI and their time series were extracted. Then, extracted time series were signal averaged across voxels (within each ROI), then across pulse trains within each scan, and then finally across sessions to generate an averaged time series of percent change in the BOLD signal for each ROI (**Fig 4.3** and **Fig. 4.6 E**).

BOLD signal responses as a function of cortical depth were computed by drawing a line perpendicular to the cortical surface, and choosing sets of three voxels (the one closest to the line, and the two horizontally flanking ones) for each cortical depth. Peak percent BOLD signal change was then averaged across each of these sets of three voxels, and then across animals ( $n = 3$ ) for each depth below the surface of the cortex (**Fig. 4.9 C**).

We utilized t-tests and ANOVA (e.g., StatView) throughout, e.g. to analyze the dependence of BOLD signal change or significantly activated brain volume upon anesthesia level and brain region.

#### **4.2.7. Local field potential (LFP) and multi-unit activity (MUA) recordings**

Two Thy1-ChR2 mice were anesthetized with isoflurane (0.5%) and headposted for electrophysiology, followed by the opening of a small craniotomy over barrel cortex. A laminar silicon linear electrode array (Neuronexus Technologies) was connected to a Cheetah32 data acquisition system (Neuralynx). The array consisted of 16 contacts along the probe shank, each with

a diameter of 15  $\mu\text{m}$  and spaced 100  $\mu\text{m}$  apart. The probe shank was inserted such that at least 12 contacts covered the cortical laminae from immediately below the surface to a depth of about 1200  $\mu\text{m}$  continuously (depicted in **Fig. 4.9 D**). Recordings were performed with minimal filtering (bandpass 0.1 – 9000 Hz), and separated into LFP and MUA signals in software using MATLAB. Specifically, MUA was determined by filtering the original recording between 600–6000 Hz and thresholding at four standard deviations above background noise; LFP was determined by filtering the original recording between 7 and 200 Hz. MUA and LFP plots in **Figure 4.9 E** and **F** were averaged across 2 animals, for 10 trials of 1 s of light stimulation (40 Hz, 8 ms pulses) each time, and plotted as a function of cortical depth. LFP power was normalized to the 1 s baseline before light onset.

#### **4.2.8. Histology**

After opto-fMRI experiments were concluded, we verified the extent of ChR2 expression. Animals were transcardially perfused with 100 mM PBS followed by 4% formaldehyde in PBS. Brains were post-fixed overnight at 4°C, and then cryoprotected in 30% sucrose for 24–48 h before sectioning. Free-floating sections (50  $\mu\text{m}$ ) were cut using a cryostat (Leica 3050S, Leica Microsystems GmbH, Wetzlar, Germany), mounted on glass slides with Vectashield mounting medium with DAPI (Vector Laboratories, Burlingame, CA) and coverslipped. Spread and labeling efficiency were estimated by examination of 50  $\mu\text{m}$  coronal sections near the site of injection for the presence of GFP. For

the five animals that underwent the core awake opto-fMRI experiments, four were histologically examined; the fifth mouse (CaMKII-ChR2-D) was not examined due to potential health issues unrelated to the opto-fMRI experiment. Examination of the entire brain between V1 and frontal cortex revealed no GFP beyond the site of injection. To estimate the volume of the cortex containing ChR2-GFP expressing cells, we measured the area in each slice, by measuring image intensity of GFP (field of view  $1.9 \text{ mm} \times 1.9 \text{ mm}$ ,  $4\times$  objective, BX51, Olympus Corporation, Tokyo, Japan). Each injection of  $\sim 1 \mu\text{l}$  labeled an ellipsoid volume with a diameter of 700-1000  $\mu\text{m}$  along the anterior-posterior aspect, 700-1000 along the medial-lateral aspect, and 800-1100 mm along the dorsal-ventral aspect. Next, we collected confocal image stacks ( $21 \mu\text{m} \times 21 \mu\text{m} \times 45 \mu\text{m}$ ; FV10i, Olympus Corporation, Tokyo Japan) sampling two regions along the dorsal-ventral axis of each GFP-positive area, on each of three equally-spaced slices sampled from each animal. For each of these regions, we counted the number of GFP-positive and DAPI-positive cell bodies. By this measure, the local density of cells expressing ChR2 would be estimated as  $314938 \pm 110485 \text{ mm}^{-3}$ , over the regions identified (mean  $\pm$  std. err;  $n = 4$  mice).

## 4.3. Results

### 4.3.1. Opto-fMRI hardware and protocol of usage

A schematic diagram of the hardware for mouse opto-fMRI is shown in **Figure 4.1**, *left*. The experimental setup combines a blue laser (as is often used for activation of ChR2-expressing neurons *in vivo*) coupled to a long optical fiber

with an optimized MRI cradle in which a rodent with a ChR2-expressing neural target is immobilized under light isoflurane anesthesia (0.5% unless otherwise indicated). Although small animal fMRI can be done in the awake state, or using various anesthetics (e.g., propofol, isoflurane, alpha-chloralose)(Hyder et al. 1994; Lahti et al. 1999; 1998; Liu et al. 2004; Peeters et al. 2001; Scanley et al. 1997; Sicard et al. 2003), we here for the initial validation of our novel technique chose to use light isoflurane, to isolate BOLD responses due to illumination of neural networks from other changes such as those resulting from injected drug administration (Austin et al. 2005; Sommers et al. 2009) or stress from restraint (King et al. 2005). The cradle allows rigid positioning of an RF coil over the brain (**Fig. 4.2**), as well as positioning of an optical fiber (which passes through the open loop of the coil) over the desired neural target on the animal's head. The RF surface coil was chosen to provide high-resolution and high signal-to-noise ratio (SNR) imaging of neocortical areas for this initial study (**Fig. 4.8**). To facilitate placement of the animal in the MRI cradle, the animal was surgically prepared in advance with a plastic head post that could be bolted to the cradle, and a craniotomy (going part or all of the way through the skull) was opened up over the cortical target, in this case, SI barrel cortex. We used both transgenic mice expressing ChR2 under the Thy1 promoter (Arenkiel et al. 2007), as well as mice in which lentivirus encoding ChR2 was used to transduce SI barrel neurons in a prior surgery. During the head post-surgery, a thin layer of dental cement (Metabond) was applied homogeneously across the surface of the skull. This step was crucial to reduce artifacts due to susceptibility variation from intact tissue to

air (Neufeld et al. 2005), which are exacerbated at the high field strengths required for high-resolution functional rodent brain imaging (**Fig. 4.2 B**).

The experimental opto-fMRI protocol (**Fig. 4.1, right**) used EPI in conjunction with a boxcar protocol of light delivery (e.g., 15 second periods of 40 Hz delivery of 8 ms laser pulses, separated by 15 second periods of no illumination). We used SE-EPI instead of the commonly used GE-EPI, as SE-EPI is less sensitive to magnetic susceptibility variability than GE-EPI (**Fig. 4.2 C** and ref. (Bandettini et al. 1994)), amongst other advantages (Kim et al. 2000; Lee et al. 1999; Moon et al. 2007). Significantly activated voxels in images were objectively identified by correlating the percent signal change of the BOLD response with a boxcar function that corresponds to the periods of light delivery, and thresholding the correlation coefficients (determined by Monte Carlo simulation) to a multiple comparisons-corrected, per voxel,  $p$ -value of  $\leq 0.05$  (equivalent to an uncorrected  $p$ -value of 0.005), and a cluster threshold, i.e. a minimum number of contiguous significantly activated voxels, of  $\geq 6$ .

#### **4.3.2. Demonstration of opto-fMRI drive of neocortical areas connected to SI barrel cortex**

We observed robust, distributed BOLD responses in neocortex ipsilateral and contralateral to the fiber illumination site, time locked to the illumination of ChR2-expressing SI neurons. **Figure 4.4 Aii** shows the results for a mouse in which lentivirus encoding ChR2 had been injected stereotaxically into the SI barrel cortex ( $n = 3$  mice; representative mouse shown; single-slice EPI images

are shown for all mice in **Fig. 4.7**). BOLD activation patterns appeared similar across the different animals, and comprised local (i.e., under the illumination point, where the virus was injected, **Fig. 4.4 Ai**) and distant sets of contiguous significantly activated voxels, both ipsilateral and contralateral to the illuminated point. A representative time series of the change in BOLD signal is plotted for a few cycles of the boxcar protocol, in **Fig. 4.4 Aiii**. We did not detect BOLD activation in control mice not expressing ChR2 (**Fig. 4.4 B**;  $n = 2$  mice; representative mouse shown; single-slice EPI images are shown for all mice in **Fig. 4.7**). This control rules out the possibility that positive BOLD responses were due to temperature change induced by laser illumination, as such temperature-induced BOLD signal changes would simulate activation patterns (Yablonskiy et al. 2000). Indeed, in control mice practically zero voxels were significantly activated even at an uncorrected  $p$ -value of 0.15, even under laser illumination with power double that used in the opto-fMRI mapping studies presented here (**Fig. 4.4 C**).

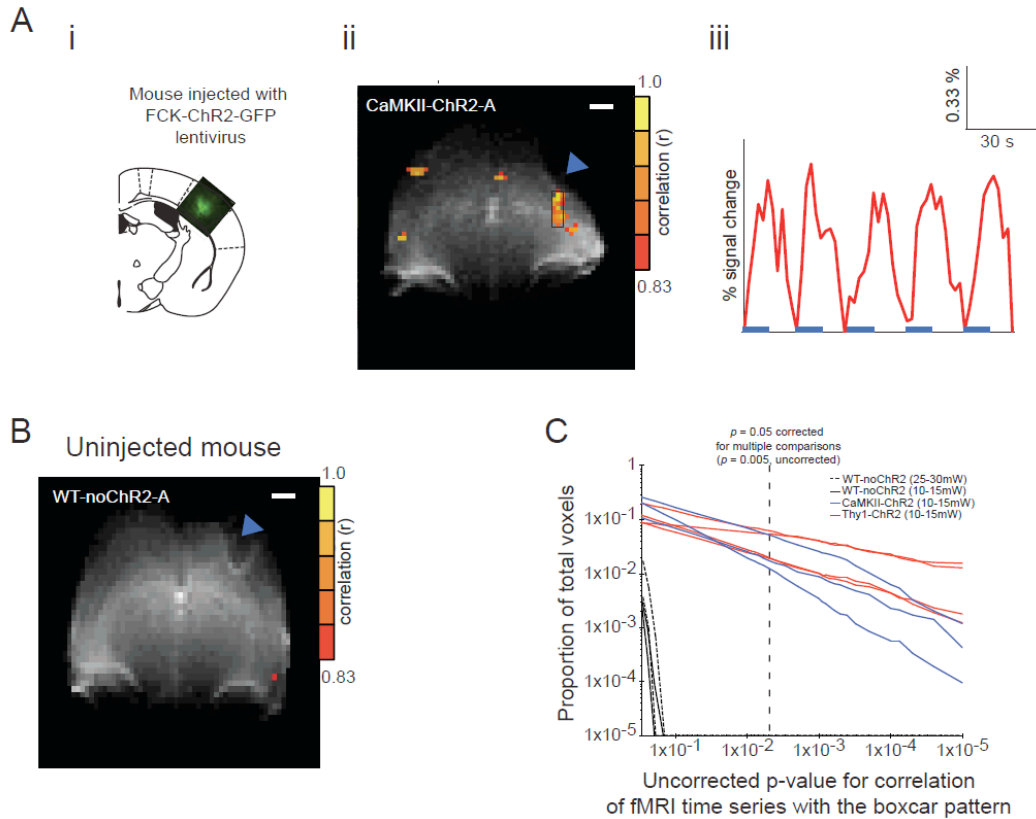


**Figure 4.4. Demonstration of ‘Opto-fMRI’ methodology.** *A*, Voxels with significant increases in signal (*ii*) are indicated for a mouse injected with FCK-ChR2-GFP lentivirus in unilateral SI (*i*, mouse atlas overlaid with histology showing ChR2-GFP expression) and undergoing Opto-fMRI. The image in *ii* was maximum-intensity projected across 4 coronal slices (2 mm). Black rectangle indicates the region of interest (ROI) whose percent signal change is plotted in *Aiii*, for the first 5 pulse trains out of the 16 pulse trains, averaged across all 4 scans of a session. *B*, Voxels with significant increases in signal for a wild-type mouse undergoing Opto-fMRI. *C*, Plot of the proportion of voxels throughout the imaged brain volume (y-axis) that yield raw uncorrected boxcar correlation  $p$ -values (see **Fig. 4.1**, bottom right) below a given value (x-axis); both x- and y-axes are plotted on a log scale. Dashed line indicates the threshold value of the multiple comparisons corrected  $p$ -value of 0.05 (that is, uncorrected  $p = 0.005$ ).

We also observed a negative BOLD response in brain tissue, close to the optical fiber tip (**Fig. 4.5 A, C and D**). The negative BOLD response of ChR2-

expressing mice was indistinguishable from that in Chr2-negative mice (**Fig. 4.5 B and F**), and even appeared, albeit to a smaller extent, in an agarose phantom (**Fig. 4.5 E**). However, there was no difference between the peak reductions in BOLD signal between Chr2-virally transduced (n = 3 mice), non Chr2-expressing mice (n = 2 mice) and *Thy1*-Chr2 mice (n = 4 mice) (**Fig. 4.5 F**;  $p > 0.80$ ,  $F(2,6) = 0.225$  for peak reduction in BOLD signal, factor of mouse type, one-way ANOVA). The fact that lack of Chr2 did not alter the BOLD signal reduction, despite its elimination of the BOLD signal increases observed (**Fig. 4.4 B and C**) led us to hypothesize that the BOLD signal reduction observed under illumination was not related to Chr2, but instead reflected a direct and local effect of light on the sample that was observable using MRI. In support of this hypothesis, we observed small but significant BOLD reductions even in plain agarose (**Fig. 4.5 E**), upon illumination.

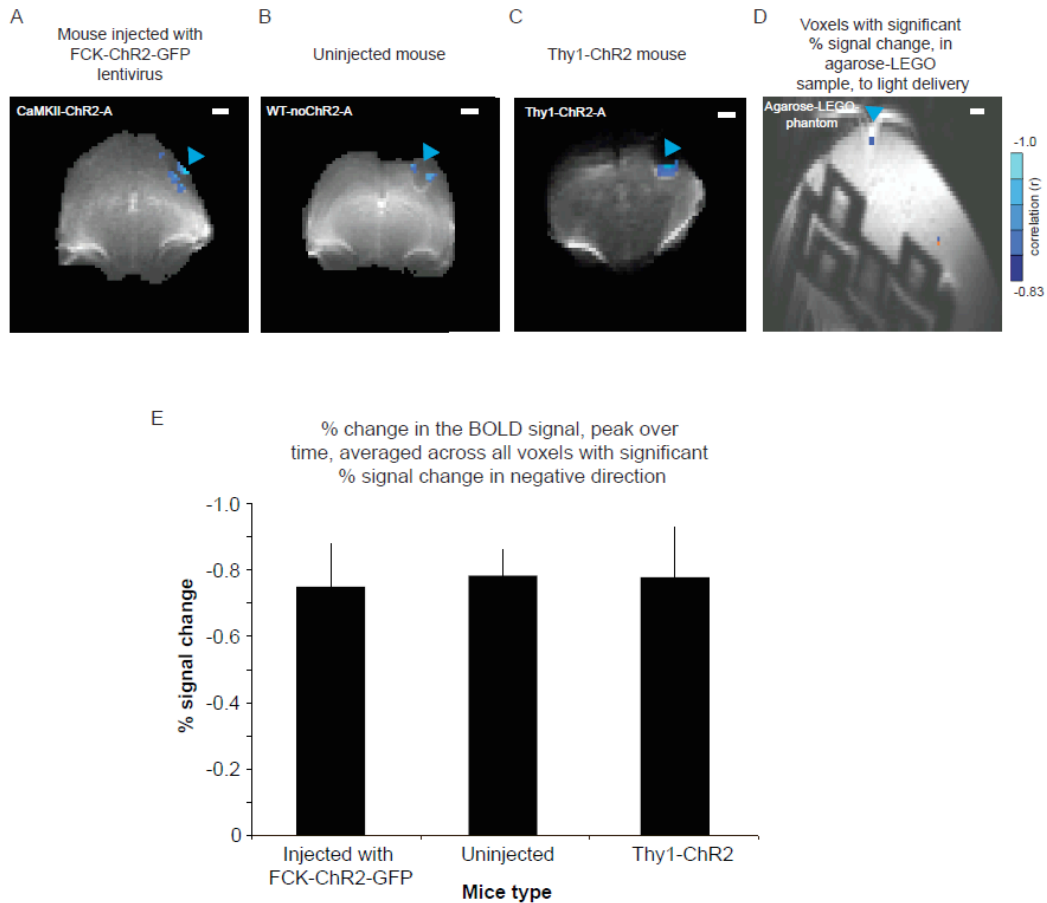


**Figure 4.5. Negative BOLD signal in mouse brain with and without ChR2, and in fMRI phantoms.** *A*, Voxels with significant decreases in BOLD signal, for a wild-type mouse injected with FCK-ChR2-GFP lentivirus, undergoing opto-fMRI, and superimposed upon the corresponding single-slice EPI image. *B*, As in *A*, but for a wild-type mouse (non-ChR2 bearing) undergoing opto-fMRI. *C*, As in *A*, but for a *Thy1*-ChR2 transgenic mouse undergoing opto-fMRI. *D*, As in *A*, but for an MRI phantom, in this case a 2 cm-diameter plastic centrifuge tube (50 mL) filled with agarose and a LEGO brick. Shown here is a single coronal slice of SE-EPI collected at a voxel resolution of 200 mm x 200 mm x 500 mm. *F*, Negative BOLD signal (at the peak timepoint, averaged across all significantly-decreased voxels), for ChR2-virally transduced ( $n = 3$  mice), non ChR2-bearing ( $n = 2$  mice) and *Thy1*-ChR2 ( $n = 4$  mice).

Thus, these independent lines of experiments support the idea that BOLD signal reductions observed during light delivery to the brains of ChR2-expressing

mice are not due to ChR2-mediated neural activation, but instead reflect a direct effect of light on the sample. One possibility is that heating may play a role; MRI thermometry suggests that heating effects the MRI signal (De Poorter 1995; Ehses et al. 2008; Kahn et al. 1998; Olsrud et al. 1998; Yablonskiy et al. 2000), however there are conflicting reports on how brain temperature correlates to the fMRI signal (Trubel et al. 2004; Yablonskiy et al. 2000). Other effects of light on brain tissue and other samples exist as well. Accordingly, for the results here reported, we confine our observations to positive BOLD signals, and to network BOLD signals outside the immediately proximal tip area where these negative effects were observed.

#### **4.3.3. Consistency of Opto-fMRI outcomes across sessions and animals**

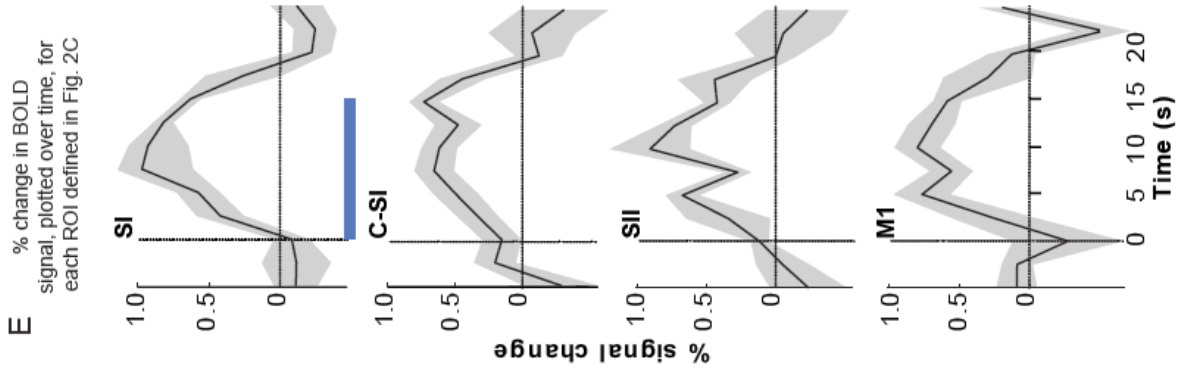
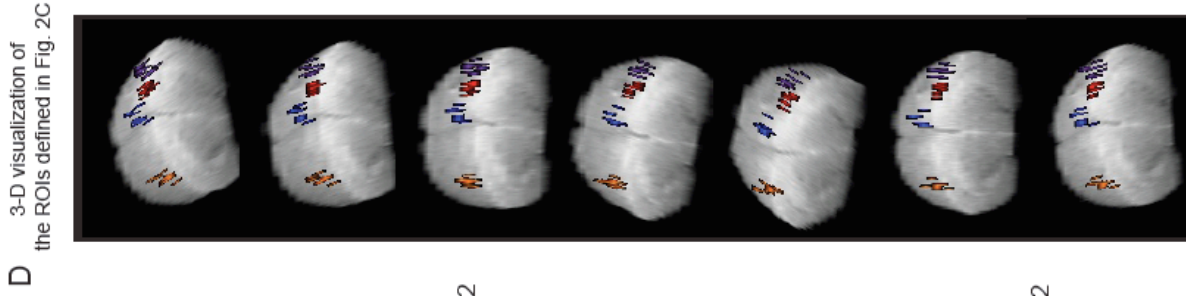
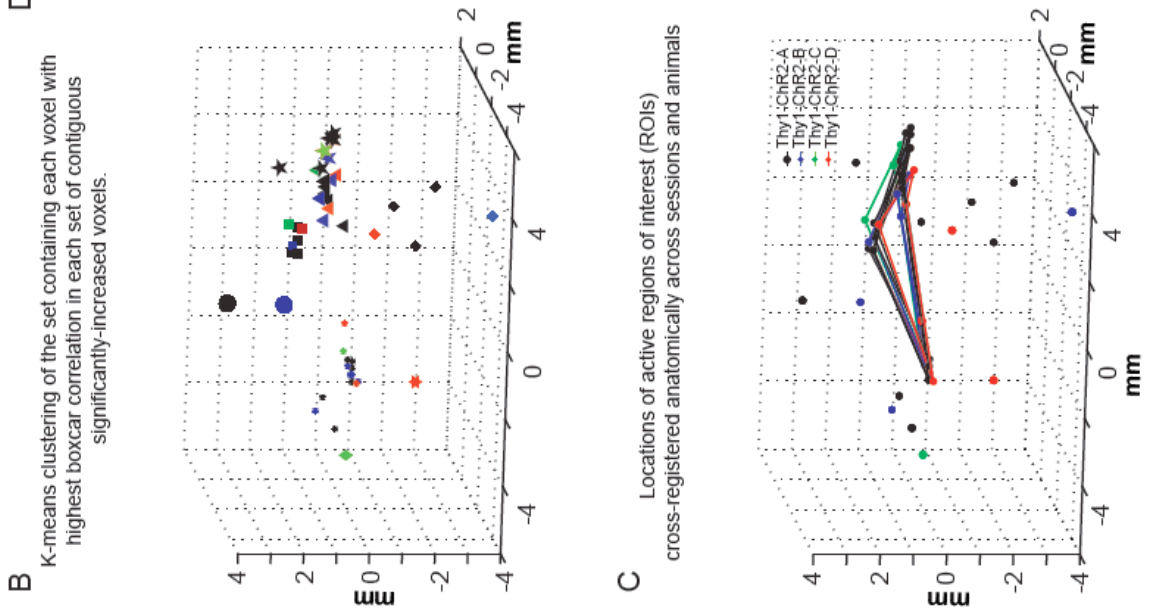
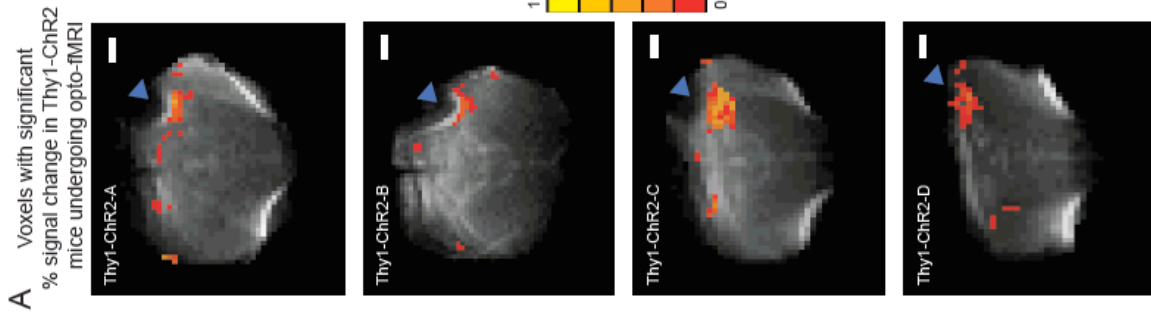


**Figure 4.6. Distributed neural activation patterns obtained via Opto-fMRI.**

As in Figure 4.4 A, the optical fiber is placed over SI, but in this case using Thy1-ChR2 mice (expressing ChR2 predominantly in layer 5 of cortex) for simplicity. A, Voxels with significant increases in signal, in Thy1-ChR2 mice undergoing Opto-fMRI; voxel color indicates the boxcar correlation of that voxel. Images are maximum-intensity projected across 4 coronal slices (2 mm), in each of four Thy1-ChR2 mice. (Only one session was performed for mouse Thy1-ChR2-C; for mice Thy1-ChR2-A, B, and D, we performed 5, 2, and 2 sessions respectively, over a period of weeks.) Shown are exemplar images with minimal craniotomy distortion; for completeness, all Thy1-ChR2 sessions performed on these mice are shown in raw single-slice form in **Figure 4.7**. B, The inputs to the clustering algorithm comprised the set of voxels that each possessed the highest boxcar correlation within a set of contiguous voxels with significantly-increased BOLD signal. Individual imaging sessions are cross-registered to each other, using EPI-assessed landmarks: the center of the medial ventricle in the EPI slice in which the craniotomy distortion is visibly maximal is set to (0, 0, 0) in this plot. Voxels are color coded to the identity of the mouse; symbols vary to delimit the different clusters obtained (8 clusters total were generated by the algorithm). C, Similar to **Figure 4.6 B**. Clusters of voxel location, showing significant activation in every session, are determined as region of interests (ROIs; the ROIs chosen were anatomically identified as SI barrel field, contralateral SI, SII, and M1; abbreviated SI, C-SI, SII, and M1 respectively). For each individual Opto-fMRI session plot, lines connect the voxels showing significant activation in every session, with color indicating the identity of the mouse. D, T2-anatomical images were 3D rendered and overlaid with colored points corresponding to the peak-correlated voxels for each ROI, anatomically cross-registered to each other as in C (in this panel, each ROI was given an arbitrary color for ease of visualization). E, Percent change in the BOLD signal, plotted over time, for each ROI of interest. The BOLD signal was, for this plot, pre-averaged across pulse trains within a scan, across sessions, and across voxels within each specified ROI. Black line, average across animals of the percent signal change; shaded area, standard error across animals of percent signal change;  $n = 4$  mice.

To characterize the consistency of the elicited network dynamics across mice and imaging sessions, we imaged four *Thy1-ChR2* transgenic mice, in which pyramidal cells in the barrel cortex, chiefly in layer V, are labeled (Wang et al.

2007). These Thy1-ChR2 mice were imaged repeatedly over a period of several weeks. All four animals exhibited similarly distributed BOLD activation patterns (**Fig. 4.6 A**), presenting sets of contiguous significantly activated voxels local and distant from the fiber illumination point, and following the patterns seen in the virally-injected mice (**Fig. 4.4 Aii**; single-slice images for all Thy1-ChR2 mouse opto-fMRI sessions are included, for completeness, in **Fig. 4.7**). The BOLD activations in SI ipsilateral to the fiber were observed in all sessions in all animals. Visual inspection suggested the existence of other sets of contiguous significantly activated voxels in the neocortex that appeared in all mice and across multiple imaging sessions (**Fig. 4.6 A**; **Fig. 4.7**), and that therefore could be considered as regions of interest. To assess the identity of these regions of interest, we first cross-registered data across animals and sessions, using anatomical markers in the EPI images to align the sets of contiguous activated voxels to a single coordinate frame. To visualize the reliability of activation patterns, we then identified through two independent means – a k-means analysis (Duda et al. 2000 2001) (**Fig. 4.6 B**), and a direct comparison of identified sets of significantly activated voxels to the mouse atlas facilitated by our knowledge of the SI circuit (**Fig. 4.6 C and D**) – three additional regions of interest, two ipsilateral to SI and one contralateral, which were represented on nearly all imaging sessions and all mice (see section **4.2. Methods** for details of these two analysis techniques). Both analyses yielded the same three major clusters in addition to ipsilateral SI (**Fig. 4.6 B, C and D**). Using the mouse atlas comparison method, we visually identified the contralateral region as contralateral SI, and the

two ipsilateral regions as MI and SII. We plotted the time series of BOLD activation responses, averaged across all the contiguous significantly activated voxels within each of these four regions of interest, and found similar time series of activation in each (**Fig. 4.6 E**), consistent with the idea that a connected network of cortical areas is begin activated upon SI illumination.

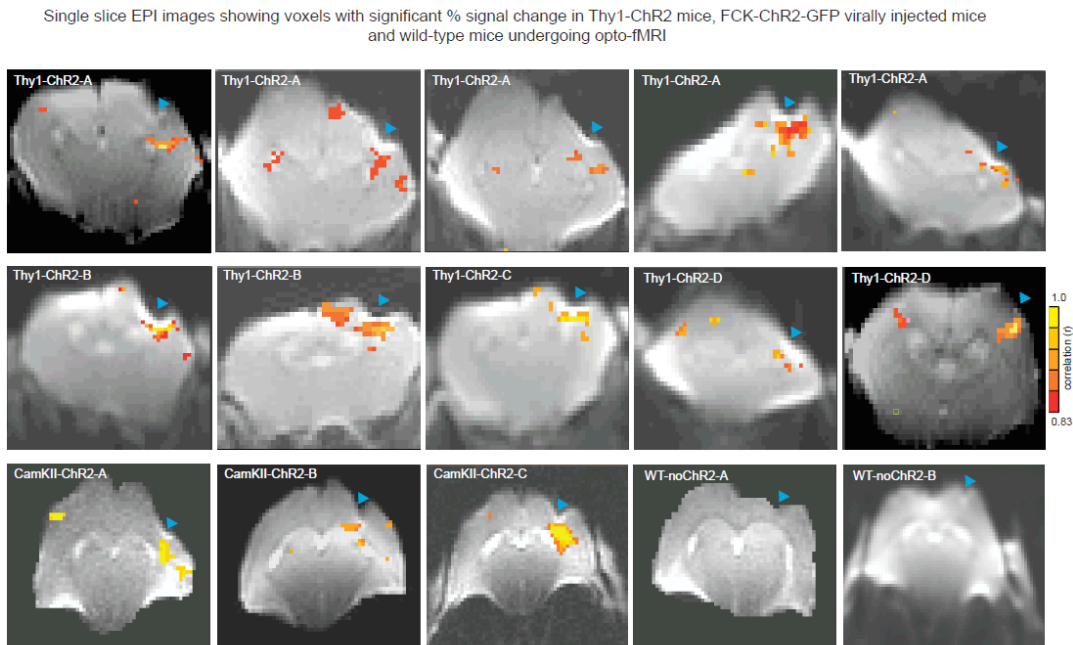


**Figure 4.7. Raw single-slice EPI images in Thy1-ChR2 mice undergoing opto-fMRI.** Voxels with significant increases in signal, for four *Thy1*-ChR2 mice in 10 imaging sessions, three FCK-ChR2-GFP lentivirally injected mice in one session each, and two wild-type mice in one imaging session each, undergoing opto-fMRI at the voxel resolution of 200  $\mu$ m x 200  $\mu$ m x 500  $\mu$ m. Voxel color indicates the boxcar correlation (see **Fig. 4.1** and **Section 4.2** for definition) for each significantly-increased voxel. Voxel statistics are superimposed upon corresponding single-slice EPI images.

The k-means algorithm also reported clusters of contiguous significantly activated voxels that were less consistent across imaging sessions and individual mice (**Fig. 4.6 B**). Atlas-based comparisons (**Fig. 4.6 C**) suggested that these clusters might represent additional activated circuits, whose reliability of observation was modulated by one or more experimental parameters. For example, in 5 out of 10 sessions, each from a different mouse, we observed significant clustered activation (cluster denoted by the ‘+’ symbol in **Fig. 4.6 B**) in a region that appeared, upon comparison to the mouse atlas, to be subcortical, e.g. in the thalamus or striatum (these activated regions are also visible in the raw EPI slices of **Fig. 4.7**). An experimental parameter that may have modulated the reliability of the subcortical responses is of the use of a surface coil, here optimized for cortical observation, but incurring the tradeoff of sacrificing SNR for deep targets (**Fig. 4.8**). We therefore focused our remaining analyses on the most stable four neocortical clusters – ‘ipsilateral’ SI (directly driven), contralateral SI, ipsilateral SII, and ipsilateral MI, as defined by the atlas coordinates of the activated areas.

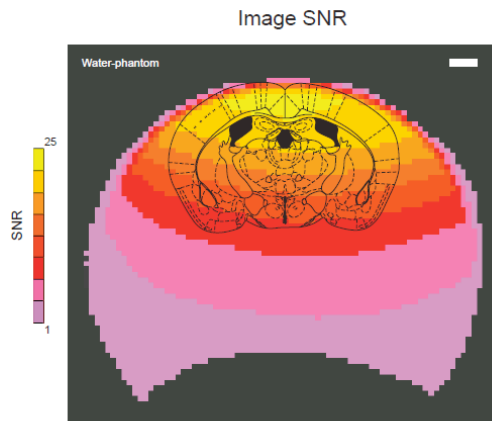


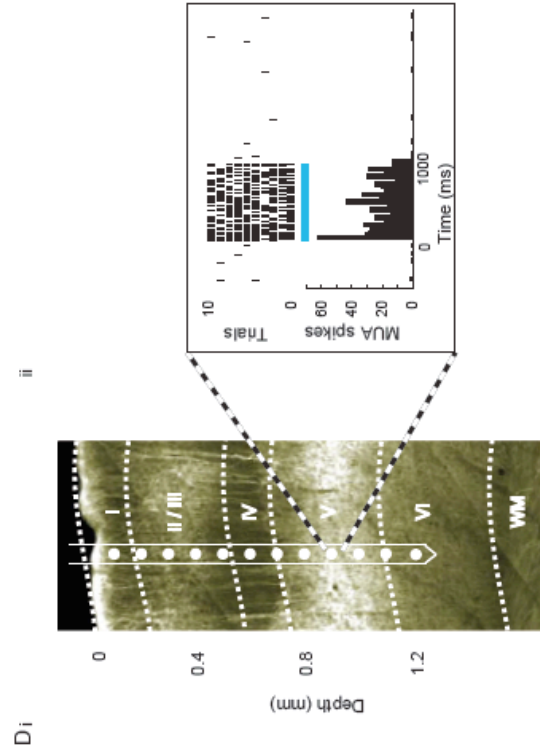
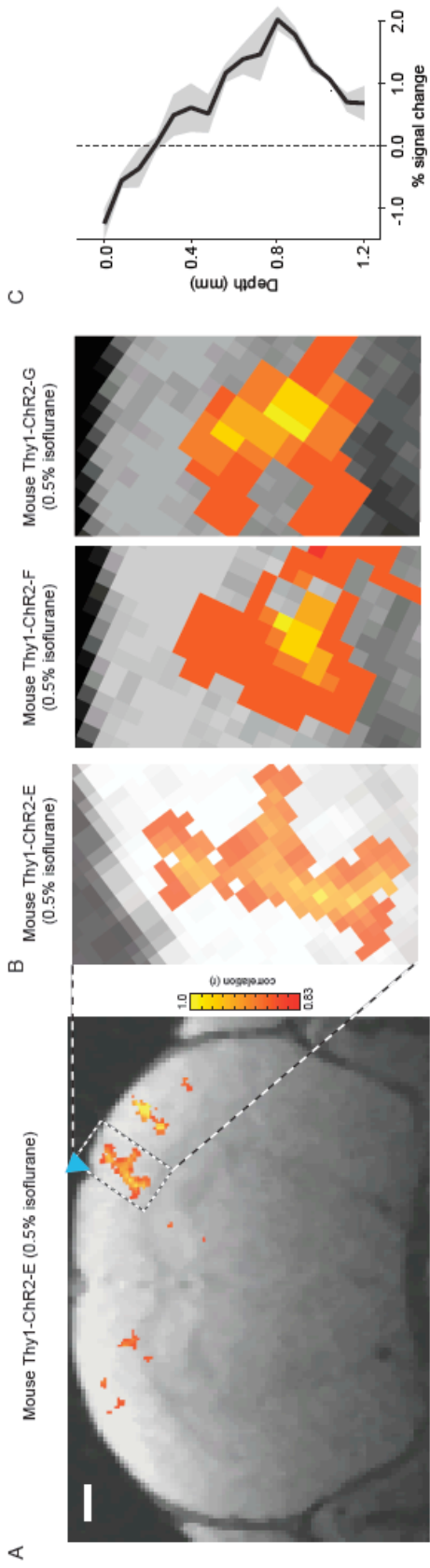
**Figure 4.8. Signal to noise (SNR) map for mouse RF coil.** An MRI phantom, in this case a 2 cm diameter plastic centrifuge tube (50 mL) filled with water, was imaged using the mouse RF surface coil (as depicted in **Fig. 4.2 A**). The MRI phantom was imaged at a voxel resolution of 200 mm x 200 mm x 500 mm. The image SNR color map, defined as (mean signal)/(thermal noise), was computed and then overlaid, for illustration purposes, over a mouse atlas image to estimate SNR drop going deeper in a mouse brain. The thermal noise was computed by picking a random timepoint of the raw EPI signal at each of 1024 voxels outside the phantom (shown in black), and then computing the standard deviation across those voxels, as described earlier (Triantafyllou et al. 2005).

#### 4.3.4. High-resolution imaging with Opto-fMRI

We anticipate that Opto-fMRI will continue to improve, riding on technological developments such as the increasing field strength of MRI scanners, continual improvements in optics, the discovery and invention of novel reagents (e.g., ref. (Chow et al. 2010)), improvements in fMRI coil design and pulse sequences, and other areas of neuroengineering innovation. As an example, we adapt a strategy from diffusion tensor imaging (DTI) (Wang et al. 2004; Wilm et al. 2007) for functional MRI, namely the use of saturation slices to reduce artifacts and to improve imaging resolution, to achieve high-resolution, near-microscopic, images (**Fig. 4.9 A–C**). We imaged at an in-plane resolution approaching 100 microns (**Fig. 4.9 A and B**), sufficient to begin resolving sub-columnar and layer-specific activity patterns (**Fig. 4.9 C**), in virally transduced and *Thy1*-ChR2 mice that express ChR2-YFP in the neocortex in layer 5 pyramidal neurons (Arenkiel et al. 2007) (**Fig. 4.9 Di**). In this mouse strain, multi-unit neural activity appeared predominantly in layer 5 (**Fig. 4.9 Dii and E**); local

field potential (LFP) power was broadly distributed in these mice, perhaps due to the extensive ChR2-positive dendrites (**Fig. 4.9 F**).

**Figure 4.9. Sub-columnar resolution Opto-fMRI (next page)** **A**, Voxels with significant increases in BOLD signal are indicated, color coded by boxcar correlation, for a representative Thy1-ChR2 mouse undergoing high-resolution ( $100\ \mu\text{m} \times 100\ \mu\text{m} \times 500\ \mu\text{m}$ ) opto-fMRI (here performed under 0.5% isoflurane anesthesia; blue laser pulse power, 10 mW). The data is shown for a single EPI slice, overlaid over a corresponding 0.5 mm thick single slice T1 anatomical image. Scale bar in the figure is 1 mm. Blue triangle indicates illumination site. **B**, Voxels in SI with significant increase in BOLD signal, for three Thy1-ChR2 mice undergoing high-resolution opto-fMRI; the leftmost of the three images is a zoomed-in subpicture of **Fig. 4.9 A**. **C**, Peak percent change in the BOLD signal (x-axis) is plotted as a function of cortical depth (y-axis, measured relative to the pia). Solid line indicates the average of the percent signal change taken across the mice shown in **B**; shaded areas indicate the standard error of percent signal change (across  $n = 3$  Thy1-ChR2 mice). **Di**, Epifluorescence image of a section (50 microns thick) of the brain of a Thy1-ChR2 mouse; the ChR2 is fused with YFP. Multiunit activity (MUA) recorded across neocortical layers was measured using a laminar silicon electrode array (contacts spaced  $100\ \mu\text{m}$ ). A representative episode of multiunit activity (MUA) recorded from an electrode contact in layer V of cortex during 1 s pulse train (40 Hz, 8 ms pulses) illumination is plotted in **Dii**. MUA firing rate (**E**) and local field potential (LFP) power (**F**) during the illumination period (x-axis; LFP power is normalized to the power in the 1 s preceding the illumination period) are plotted as a function of cortical depth (0 to  $1200\ \mu\text{m}$ ; y-axis). Solid line indicates the average of the MUA firing rate and the LFP power; shaded areas indicate the standard error ( $n = 2$  Thy1-ChR2 mice).



## 4.4. Discussion

We demonstrate here strategies that combine fMRI with optical control of neural activity in order to enable, in acute and chronic settings, the characterization of neural networks driven by optical activation. These innovations include the hardware, surgical strategies, pulse sequences, and clustering and cross-correlation data analytic methods appropriate for determining how the activity in a neural network is influenced by optically-controlled stimulation of a defined node in the circuit. We demonstrate, with the case example of optical stimulation of the excitatory neurons in SI barrel cortex, the use of this technology to delineate how different parts of a neural network are modulated by a single upstream target site, and we also use this technology to explore how such network coupling is influenced by isoflurane anesthesia level. The opto-fMRI method we describe here provides a general strategy for characterizing the strength of connections in a fashion that is amenable to repeated assessment, potentially over long time periods. Opto-fMRI thus enables the monitoring of functional connectivity throughout neural development, during learning and plasticity, and during aging and the course of neurological disease and candidate disease treatments. We characterized activity in a circuit of relatively well-known connectivity. In principle, this strategy can also be used to detect new targets of a given neural pathway or cell class, although in such cases, it will be important to validate discoveries with traditional means, such as tract tracing and electrical recording.

Several innovations were critical to this deployment of opto-fMRI. RF surface coils were custom- designed for mouse and rat brain imaging, and these provided for high signal to noise ratios in the cortical signals and enabled high spatial resolution. We used SE-EPI for BOLD contrast instead of the widely used GE-EPI, as SE-EPI minimizes magnetic susceptibility artifacts and suppresses contributions from large draining vessels (Kim et al. 2000; Lee et al. 1999), therefore providing for high spatial resolution of the BOLD response (Duong et al. 2003; Moon et al. 2007). Minimization of magnetic susceptibility by coating the skull with dental acrylic and minimizing craniotomy size, with the extreme of shining light through the skull, was crucial to eliminating EPI distortion artifacts. The use of saturation slices also augmented resolution. Further, the algorithms described, especially the set of clustering and normalized cross-correlation analyses, were especially useful for analyzing the data obtained with the opto-fMRI method.

Opto-fMRI enables a functional definition of a neural network, akin to a 3-dimensional slice experiment in which activation of a defined class of cells is performed in conjunction with recording of activity in connected areas, but because of its minimally invasive nature, opto-fMRI enables longitudinal assessments of function as well as characterizations of acute brain state. Importantly, because the assessment is not only of anatomical connectivity but also of functional coupling (e.g., a given pathway may anatomically appear sparse but actually be strong functionally), the strength and excitability of a pathway or set of pathways can be assessed. We thus anticipate that the opto-fMRI method

presented here will enable a broad range of new studies, such as the monitoring of normal and pathologic plasticity during disease progression and treatment or learning task acquisition. This approach should also help improve our understanding of the basis of fMRI signals in neural networks.

Limitations are also present in the opto-fMRI method introduced here. First, none of the protocols described allow conclusive identification of a monosynaptic connection. Also, weak, ‘modulatory’ functional connections (Guillery and Sherman 2002) or transient connections may not be detectable because of the slow temporal response of the BOLD signal and the nature of neural to hemodynamic coupling. This limitation of poor temporal resolution is in part offset by the great utility of this approach for planning the precise targeting of electrodes to parts of a circuit that are identified functionally and spatially as important by this method.

A major point of concern regarding characterizing functional connectivity in a circuit was one that of antidromic spiking observed in Thy1 mouse model (Gradinaru et al. 2009). The concern is that perhaps we were falsely characterizing the distal response as downstream to the optogenetically stimulated SI network response. When in fact, the distal response could be antidromically recruited by optical stimulation of SI neurons.

Another point of concern in these experiments was the instability of subcortical activation patterns here observed. This may be due to isoflurane use, which suppresses somatosensory-evoked information transfer to subcortical

regions, as previously reported using electrophysiological recording (Detsch et al. 2002; West 1998) as discussed in **Chapter 3**.



## Chapter 5. Opto-fMRI: Mapping Brain Networks in Awake Mice

This chapter is adapted from:

Published conference proceedings; Mitul Desai, Itamar Kahn, Jacob Bernstein, Hisham Atallah, Nancy Kopell, Randy L. Buckner, Christopher I. Moore, Ann M. Graybiel, & Ed S. Boyden; “Opto-fMRI: Ultra-High Resolution Causal Circuit Mapping, and Application to Analysis of Network Dynamics.”, 40<sup>th</sup> annual Society for Neuroscience meeting, San Diego, CA.

A published paper; Mitul Desai\*, Kahn I.\*, Knoblich U., Bernstein J., Atallah H., Yang A., Kopell, N., Buckner R.L., Graybiel A. M., Moore C. I.1, & Boyden E. S.; “Mapping Brain Networks in Awake Mice Using Combined Optical Neural Control and fMRI”, *Journal of Neurophysiology* 2011 Mar;105(3):1393-405.

\* These authors contributed equally

### 5.1. Introduction

Functional magnetic resonance imaging (fMRI) based on the blood oxygenation level-dependent (BOLD) signal (Kwong et al. 1992; Ogawa et al. 1990b; Ogawa et al. 1992) is widely used to indirectly measure neural activity in distributed brain networks in humans and non-human primates. As we saw in **Chapter 4** and also revealed in another recently published study, optogenetic strategies, using activation of channelrhodopsin-2 (ChR2) expressing neurons, can be used with high-field MRI imaging to evoke BOLD signals in the anesthetized rodent (Lee et al. 2010). We here present data obtained using optogenetic activation of a specific cell class in the awake animal, mapping and characterizing the distributed network responses that result. These opto-fMRI studies collectively open up a wide array of opportunities for exploring the relation

between BOLD responses and neural activity, and to use rodent models to assess the impact of causal manipulations on distributed brain networks.

The works presented in **Chapter 4** and the work by (Lee et al. 2010) illustrates the potential of optical neural control and fMRI in the anesthetized state. The study from (Lee et al. 2010) demonstrate that a BOLD response to light-driven epochs of stimulation in MI in anesthetized rats transfected with ChR2 in Ca<sup>2+</sup>/calmodulin-dependent protein kinase II $\alpha$  ( $\alpha$ CaMKII)-expressing neurons. Like prior analyses of sensory evoked responses in the humans (Boynton et al. 1996), the measured BOLD response began a few seconds after stimulation and decreased about 6 seconds following stimulation offset. (Lee et al. 2010) also revealed downstream effects of optical stimulation by demonstrating a robust BOLD response in the thalamus during local MI stimulation.

These results raise the possibility that opto-fMRI could serve as a tool to explore properties of distributed brain networks – for example enabling researchers to focus their electrophysiological or anatomical experiments on opto-fMRI-identified sets of brain regions or to examine how large-scale brain network properties are affected by molecular genetic manipulations. By providing a bridge between the increasingly widespread use of optical methods to probe causal neural circuit functions in animals and fMRI, which in humans is typically performed in the awake state, opto-fMRI in the awake mouse may play an important role in the translation of neural circuit insights derived from animal experimentation towards basic and clinical neuroscience in the human.

In this paper we describe an initial exploration of an awake mouse model of optogenetic stimulation performed during fMRI, thus enabling measurement of large-scale circuit dynamics in a behaviorally-relevant state. Using awake mice expressing ChR2 in pyramidal cells in the primary somatosensory (SI) barrel cortex as a model system, we demonstrate the detection, in individual mice, of cortical and striatal structures known to be connected to SI (Aronoff et al. 2010; Carvell and Simons 1986; 1987; Chakrabarti and Alloway 2006; Diamond et al. 2008; Ferezou et al. 2007; Megevand et al. 2008; White and DeAmicis 1977). We also demonstrate the use of opto-fMRI to assess how the administration of the common anesthetic isoflurane modulates the set of recruited structures downstream of a cell type, as well as the connectivity between them.

## **5.2. Materials and Methods**

### **5.2.1. Animals and surgery.**

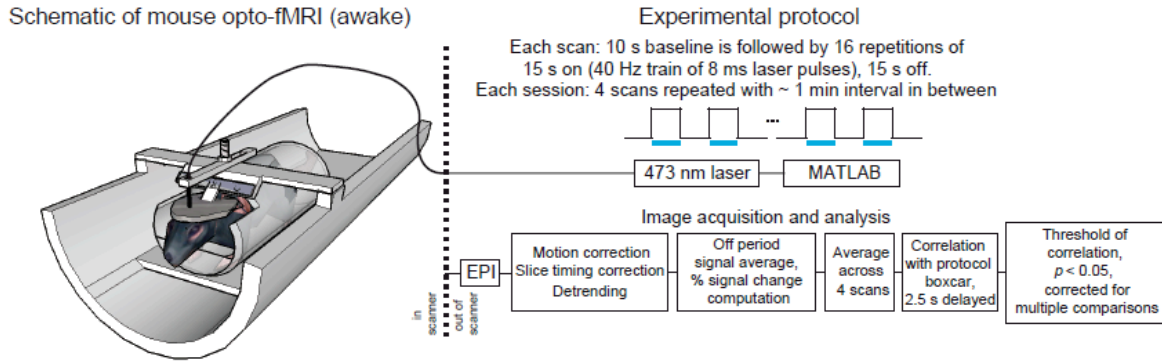
All procedures were conducted in accordance with National Institutes of Health guidelines and with the approval of the MIT Committee on Animal Care. 5 wild-type mice (C57BL/6, purchased from Charles River), and 4 transgenic ChR2 mice (line 18, stock 007612, strain B6.Cg-Tg (Thy1-COP4/EYFP)18Gfng/J from Jackson Labs, Bar Harbor, ME; bred in-house with wild-type mice) were used. A summary of animals used for the different experiments throughout this study is presented in **Table 5.1**.

Table 5.1.

Experiment type	Mice			fMRI parameters		Referenced in...
	Animal type	Number of animals	Animal IDs	Voxel resolution	Number of slices	
<b>Opto-fMRI</b>						
Awake followed by 0.7% isoflurane	Virally injected wild types	5	CamKII-ChR2-1 thru 5	150 $\mu\text{m}$ $\times$ 150 $\mu\text{m}$ $\times$ 500 $\mu\text{m}$	5	Fig. 5.2, Fig. 5.3, Fig. 5.4 C, Fig. 5.5 - 5.11, and Fig. 5.13
0.5% isoflurane	Un-injected wild types	2	WT-noChR2-1 and 2	200 $\mu\text{m}$ $\times$ 200 $\mu\text{m}$ $\times$ 500 $\mu\text{m}$	10	Fig. 5.4 A and B
0.5% and 1.0% isoflurane	Thy1-ChR2 mice	4	Thy1-ChR2-1 thru 4	200 $\mu\text{m}$ $\times$ 200 $\mu\text{m}$ $\times$ 500 $\mu\text{m}$	10	Fig. 5.4 D, Fig. 5.12, and Fig. 5.14

**Table 5.1. Summary of animal usage and fMRI parameters for different experiments throughout this chapter.** The table presents a summary of all the animals that are used throughout this study and the kind of experiments they are used for. The summary also presents the fMRI parameters (resolution and number of slices) employed for a specific experiment and the figure it represents in this chapter.

For viral injection, 5 wild-type mice were first anesthetized with isoflurane (~1-2% mixed with oxygen), then craniotomized (~0.5 mm wide) and injected with lentivirus encoding for ChR2-GFP under the CaMKII promoter (FCK-ChR2-GFP, 1  $\mu\text{L}$ , as utilized in (Han et al. 2009), over a 30-minute period, into the left SI barrel field). Injections were performed using an injection pump (Quintessential Stereotaxic Injector, Stoelting Co., Wood Dale, IL) driving a 10  $\mu\text{L}$  Hamilton syringe connected to a glass micropipette (100  $\mu\text{m}$  tip) via polyethylene tubing. The system was filled with mineral oil. The coordinates of viral injection relative to bregma were as follows: 1.0 mm posterior, 3 mm lateral, 0.7 mm ventral.



**Figure 5.1. Design of ‘Opto-fMRI’ setup. Left, schematic of Opto-fMRI setup for measuring distributed neural activation patterns due to optical perturbation of an opsin-expressing cell type.** The setup is similar to the one shown in **Chapter 4 (Fig. 4.1)**, except for the body restraint tube used for awake mouse imaging. A mouse bearing an MRI-compatible head post was attached to a head post holder, which is in turn attached to a cradle with RF coil attached. An optical fiber holder orients an optical fiber (200 microns wide) into the craniotomy, above the cortical surface. The cradle is inserted into a 9.4T MRI scanner. *Top right*, boxcar-pattern protocol for delivery of a series of 15 second periods (indicated by blue bars, in this and subsequent figures) of 40 Hz pulse trains of 8 ms blue laser pulses (473 nm, 10-15 mW unless otherwise indicated), driven by a PC running MATLAB. *Bottom right*, images (EPIs) are motion-corrected, slice-timing corrected, detrended, converted into percent signal change by subtracting the average signal from the “laser off” periods, and averaged across scans. Then, the percent signal change is correlated, voxel-wise, to the boxcar pattern of the protocol, shifted forwards by 2.5 seconds to compensate for the BOLD delay, in order to determine the voxels that are significantly changing. Significance was judged with respect to a Monte Carlo simulation, as having a multiple comparisons corrected p value of 0.05 for the boxcar correlation (uncorrected p-value  $< 0.005$ ;  $r > 0.83$ )

For opto-fMRI, animals were surgically implanted – with a headpost (**Fig. 5.1**) atop their skulls using dental cement (C&B-Metabond, Parkell, Inc.). The headpost (weighing ~250 mg) and the headpost holder were custom made from Accura 55 plastic, an ABS-like plastic (**Fig. 5.1**). For virally injected animals, the headpost surgery was done at least three weeks after the surgery for viral

injection. For Thy1-ChR2 mice, a small craniotomy (~ 0.5 mm) was also drilled at this time through the skull over SI to allow positioning of the optical fiber above the cortical surface. At the end of each surgery, exposed skull (except for that which was thinned) was covered with a thin and uniform layer of dental cement to minimize echo-planar image (EPI) distortion caused by susceptibility mismatch in fMRI.

### **5.2.2. Awake and anesthetized opto-fMRI of mouse: Experimental setup and protocol**

Opto-fMRI data were acquired on a 9.4 Tesla (Bruker BioSpin MRI GmbH, Ettlingen, Germany), 20 cm inner diameter, horizontal bore magnet. Custom-built radio frequency (RF) transmit-receive surface coils, specifically designed for mouse, were used for imaging.

Opto-fMRI experiments were performed on 5 virally injected wild-type mice, 4 Thy1-ChR2 mice. 5 virally injected mice underwent awake imaging followed by 0.7% isoflurane anesthetized imaging. 4 Thy1-ChR2 mice were imaged at 0.5% and 1.0% isoflurane.

For animals that underwent awake imaging, three consecutive days of acclimation to head restraint and scanner noise were first performed, followed by fMRI data collection starting on the 4<sup>th</sup> day. Past experiments in awake head-restrained mice have shown that after a few days of such acclimation, overt stress is greatly reduced, as observed behaviorally (e.g., little or no struggling, eye secretions indicative of stress in mice, or excessive vocalizations or other signs of

stress) (Boyden et al. 2006; Boyden and Raymond 2003). Each session was performed at approximately the same time of day, around 2 PM, to minimize the influence of circadian rhythm. The headposted animal was inserted into the custom built G-10 fiberglass MRI cradle and then restrained for about 20 minutes to acclimate the animal to this head restrained position. The animal was given chocolate sprinkles while restrained on the MRI cradle. After 20 minutes of head restraint acclimation, the cradle was then inserted into the 9.4T MRI scanner. The cradle was locked to the MRI scanner stage so as to position the head of the animal in the center of the magnet bore. A SE-EPI sequence, similar to the one used for fMRI data collection, was run for 40 minutes to acclimate the animal to scanner noise. Then the animal was taken out of the scanner and given 2 more chocolate sprinkles before finally being taken out of the body restraint tube and the headpost holder.

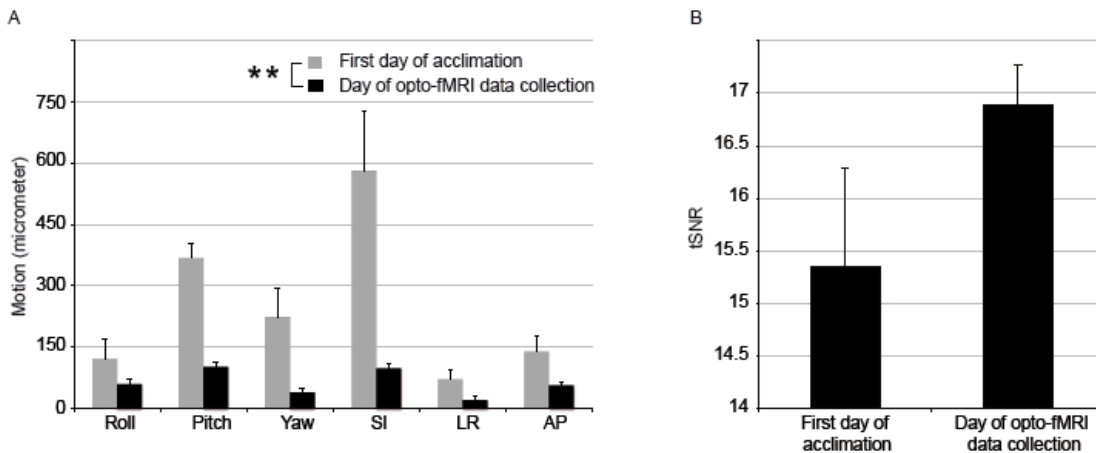


**Figure 5.2. Signal-to-noise characteristics pre- and post-acclimation. A,** Average ( $n = 5$  mice) measurements of motion (estimated from EPI scans) while the animals are in the fMRI scanner. The measurements are from the first day of acclimation (grey bars) and the day opto-fMRI data was collected, following 3

days of acclimation sessions (black bars). Motion ( $\mu\text{m}$ ) is measured in three orientations (Superior-Inferior (SI), Left-Right (LR) and Anterior-Posterior (AP)) and three rotational directions (roll, pitch, yaw). \*\*,  $p < 0.0001$ , factor of acclimation (two-way ANOVA of acclimation  $\times$  orientation of motion). **B**, Average ( $n=5$  mice) SNR measurements from the first day of acclimation (grey bar) and the day opto-fMRI data were collected (following 3 days of acclimation sessions). Temporal SNR (tSNR) was computed from the scans without optical illumination and from 100 voxels in the S1BF region (contralateral to the optical illumination). tSNR was determined from the mean pixel value across the 200 time points divided by its temporal standard deviation.

fMRI data were collected during all three acclimation sessions were used to estimate head motion of the animal being scanned. Animal head motion was computed using the 3dvolreg program in AFNI. The 3dvolreg program assumes a rigid body transformation and minimizes a least squares difference between each source sub-brick volume and the base. We find the animal head motion reduced significantly (**Fig. 5.2 A**;  $F(1,48) = 261.82$ ,  $p < 0.0001$ , main effect of acclimation in a two-way ANOVA of acclimation  $\times$  orientation of motion;  $F(5,48) = 59.38$ ,  $p < 0.0001$ , main effect of orientation of motion in a two-way ANOVA of acclimation  $\times$  orientation of motion;  $F(5, 48) = 34.122$ ,  $p < 0.001$ , interaction between acclimation and orientation of motion) following three days of acclimation when compared to unacclimated animal (first day of acclimation). Changes in signal-to-noise ratio for EPI scans were also computed for all three days of acclimation. Temporal SNR (tSNR) was computed from the scans without optical illumination, from 100 voxels in the S1BF region (contralateral to the optical illumination). tSNR was determined from the mean voxel value across 200 time points, divided by temporal standard deviation of that voxel's signal.

The change in average tSNR following three days of acclimation compared to the first day of acclimation is plotted in **Figure 5.2 B**. There was a trend towards an increase in tSNR following three days of acclimation (paired *t*-test,  $n = 5$  mice;  $p = 0.12$ ).

During awake opto-fMRI, a RF transmit-receive coil (single copper loop, milled out from a copper plated 1/16" epoxy material [FR-4, T-Tech, Inc., Norcross, GA]) was positioned over the animal's head, surrounding the headpost. The animal was attached by its headpost to the headpost holder, which was in turn attached to the MRI cradle. The animal was then positioned in a body restraint tube – a 4.5 cm diameter, 2 mm wall thickness, plastic tube with an enclosed end at the tail end of the tube, padded with an absorbent material – that lightly fits around the animal's body and restricts motion during opto-fMRI experiments. The restraint tube was bolted to the MRI cradle. A 200  $\mu\text{m}$  optical fiber (Ocean Optics, Dunedin, FL) attached to an adjustable optical fiber holder was also, at this time, positioned directly on the target (i.e., into the craniotomy, right above the brain), passing through the RF coil. A nose-cone for isoflurane delivery was positioned around the animals' snout. The MRI cradle was then slid into the magnet bore. The cradle was then locked to the MRI scanner stage so as to position the head of the animal in the center of the magnet bore. Animals were anesthesia induced with isoflurane right after the awake functional imaging experiment. The anesthesia level for these animals was maintained, as indicated by end-tidal isoflurane level (see below), at 0.7%.

For purely anesthetized imaging, animals were anesthetized with isoflurane (2-3% in oxygen) before positioning them on the MRI cradle. The MRI cradle was then slid into the magnet bore. The cradle was locked to the MRI scanner stage so as to position the head of the animal in the center of the magnet bore. Breathing rate (Small Animal Monitoring 1025, SA Instruments, Stony Brook, NY) and end-tidal expired isoflurane (V9004 Capnograph Series, Surgivet, Waukesha, WI) were continuously monitored during awake and anesthetized imaging experiments. The anesthesia level was set at 0.5% or 1.0%, as indicated by end-tidal isoflurane level.

Functional images were collected at voxel resolution  $150\ \mu\text{m} \times 150\ \mu\text{m} \times 500\ \mu\text{m}$  (5 slices; mouse images in **Fig. 5.3–5.11** and **Fig. 5.13**), or  $200\ \mu\text{m} \times 200\ \mu\text{m} \times 500\ \mu\text{m}$  (10 slices; mouse images in **Fig. 5.12** and **Fig. 5.13**). For simplicity, a summary of fMRI parameters used for different experiments throughout this study is presented in **Table 5.1**. Functional data were acquired using a SE-EPI; 2.5 s repetition time ( $T_R$ ) and 25 ms Echo time ( $T_E$ ). High-resolution T1-weighted anatomical images ( $78\ \mu\text{m} \times 78\ \mu\text{m} \times 500\ \mu\text{m}$ ) were acquired using a rapid acquisition process with relaxation enhancement (RARE) sequence in the coronal orientation, after physiological data acquisition was complete. Statistical maps of the correlation of BOLD percent signal change to the boxcar pattern of light delivery (aka boxcar correlation maps) were aligned to the high-resolution T1-weighted structural volumes using AFNI's `align_epi_anat.py` program.

The optical protocol used for opto-fMRI in this paper was a 10 s baseline period of darkness followed by 16 repetitions of 15 s on, 15 s off periods of 40 Hz trains of 8 ms laser pulses (the boxcar pattern shown in **Fig. 5.1**, *top right*), applied to the SI cortex. Light was delivered with a 473 nm blue laser (Shanghai Dream Lasers, Shanghai, China), placed outside the magnet room and coupled to a 200  $\mu\text{m}$  optical fiber ( $\sim 5$  m in length), which was passed inside the magnet room through a small duct. A MATLAB program and a USB Data Acquisition Module (Cole-Parmer, Vernon Hills, IL) were used to control the laser to deliver the protocol boxcar pattern (**Fig. 5.1**, *top right*).

For mapping experiments in the 5 virally injected mice and 4 Thy1-ChR2 mice the laser power out the fiber was 5 mW-10 mW (fiber tip irradiance, 150-300  $\text{mW}/\text{mm}^2$ ).

### **5.2.3. Opto-fMRI of mouse: data analysis**

The data analysis pipeline used for the awake and anesthetized opto-fMRI data was identical to the one described in **Chapter 4.2.4**. Once again, the analysis pipeline is outlined in the lower right hand part of **Figure 5.1**. Boxcar correlation maps for EPI functional data were generated using AFNI(Cox 1996; Nelson et al. 2006) (NIH, <http://afni.nimh.nih.gov/afni>, Bethesda, MD) and MATLAB (The Mathworks, Natick, MA).

#### **5.2.4. Region of interest (ROI) identification and cross-registration**

To identify regions showing positive BOLD responses, boxcar correlation maps (that is, the correlation of BOLD percent signal change to the boxcar model, as described above) were aligned to the high-resolution T1-weighted structural volumes using AFNI's `align_epi_anat.py` program. High-resolution T1-weighted structural images were cross-registered between mice using AFNI's `3dAllineate` program; then this alignment was used to bring the boxcar correlation maps into a standard coordinate space.

To identify the regions that show consistent BOLD responses across different animals, we once again use k-means clustering analysis that was described in **Chapter 4.2.5**. Key ROIs were named overlaying T1 anatomical images onto corresponding atlas plates from the Paxinos and Watson (1998) atlas, by matching their anteroposterior coordinates and scaling atlas plates along the x and y axes until the borders of the T1 anatomical images and the atlas plate corresponded.

As a test of robustness, the k-means clustering analysis was repeated on correlation maps obtained for two different values of boxcar correlation  $p$ -value threshold (5x higher and 5x lower than the one objectively chosen via Monte Carlo simulation to result in a multiple comparisons corrected type I error of 5%; **Fig. 5.8**).

### 5.2.5. ROI time series analysis.

Extracted time series from each key ROI were signal averaged across the contiguous significantly activated voxels associated with each key ROI, then averaged across pulse trains within a session (consisting of 4 scans, of 16 pulse trains each), to generate an average time series of percent change in the BOLD signal for each key ROI (**Fig. 5.11** and **5.12**). The peak percent change in the BOLD signal, across time, was then extracted from these thus-averaged traces.

We assessed the extent to which BOLD signal time series could be fit with a human-derived canonical hemodynamic response function (HRF). We produced a goodness-of-fit ( $R^2$ ) measure, and probability that the fit is statistically significant, by applying a least squares linear regression for each key ROI, in each of the awake and anesthetized (0.7% isoflurane level) states, each time taking into account data from each of the 5 animals to compare against the canonical HRF. In a separate analysis, we sought to test whether the goodness-of-fits themselves differed between the awake and anesthetized states or between regions. For this analysis, the goodness-of-fit ( $R^2$ ) for the default value of delay of response (6 s, relative to onset) was first computed on each animal's individual time series (averaged across scans within a session) and then through Fisher's z-transform computed the z-score for the goodness-of-fit to the HRF. The resultant set of z-scores was subjected to a two-way ANOVA with factors of brain state and ROI. In a second analysis, we varied the delay of response parameter from 1 to 12 s. The delay of response for which the  $R^2$  value was maximum, was computed for each animal independently, and the resultant set of delay of responses that

resulted in peak  $R^2$  values was subjected to a two-way ANOVA with factors of brain state and ROI.

Normalized cross-correlations of BOLD percent signal change time series were computed between pairs of key ROIs (**Fig. 5.13** and **5.14**) (Haralick and Shapiro 1992). We computed, for each key ROI, the average of all the normalized cross correlations between that ROI and all the other key ROIs; this average was then termed the “total connectivity” of that region.

We utilized t-tests and ANOVA (e.g., StatView) throughout, e.g. to analyze the dependence of BOLD signal change or significantly activated brain volume upon anesthesia level and brain region.

## **5.3. Results**

### **5.3.1. Optimization of opto-fMRI methods for awake mice**

A diagram of the opto-fMRI hardware for awake mouse imaging is shown in **Figure 5.1**. This equipment consists of a blue laser coupled to a long optical fiber, a custom-engineered MRI cradle for holding an awake mouse (CAD design available on request), a body restraint tube within the cradle for minimizing body motion, an RF coil, and an optical fiber and holder (which passes through the open loop of the RF coil) over the desired neural target. To facilitate placement of the animal in the MRI cradle, the animal is surgically prepared in advance with a plastic head post that is bolted into the cradle at the beginning of an experiment. The animal is also prepared with a craniotomy or thinned skull over the area of interest (in this case, the SI barrel cortex, which has been transgenically or virally

labeled to express ChR2 in pyramidal neurons). The experimental opto-fMRI protocol (**Fig. 5.1, right**) used echo planar imaging (EPI) in conjunction with a boxcar protocol of light delivery (15 s periods of 40 Hz delivery of 8 ms laser pulses, separated by 15 s periods of no illumination). Significantly activated voxels in images were identified by correlating the percent signal change of the BOLD response with a boxcar function that corresponded to the periods of light delivery, then selecting the voxels whose correlation coefficients were significant at a family-wise multiple comparisons-corrected  $p$ -value level of  $< 0.05$  (equivalent to an uncorrected  $p$ -value of 0.005), and had 5 or more significant neighbors (i.e., a cluster threshold of 6). The uncorrected  $p$ -value of 0.005 and the cluster threshold of 6 were objectively determined using the Monte Carlo simulation program of AFNI (Forman et al. 1995a; Xiong et al. 1995b).

Our method was optimized along a number of experimental axes. First, to enable fMRI in awake mice, it was critical to acclimate mice to head restraint and scanner noise over a multi-day period under conditions similar to actual opto-fMRI experimentation. In addition, the body restraint tube was important for reducing body motion. Although the body was not in the fMRI field of view, motion can cause susceptibility artifacts in brain images by changing the magnetic environment.

### 5.3.2. BOLD signal changes downstream of SI pyramidal cell activation

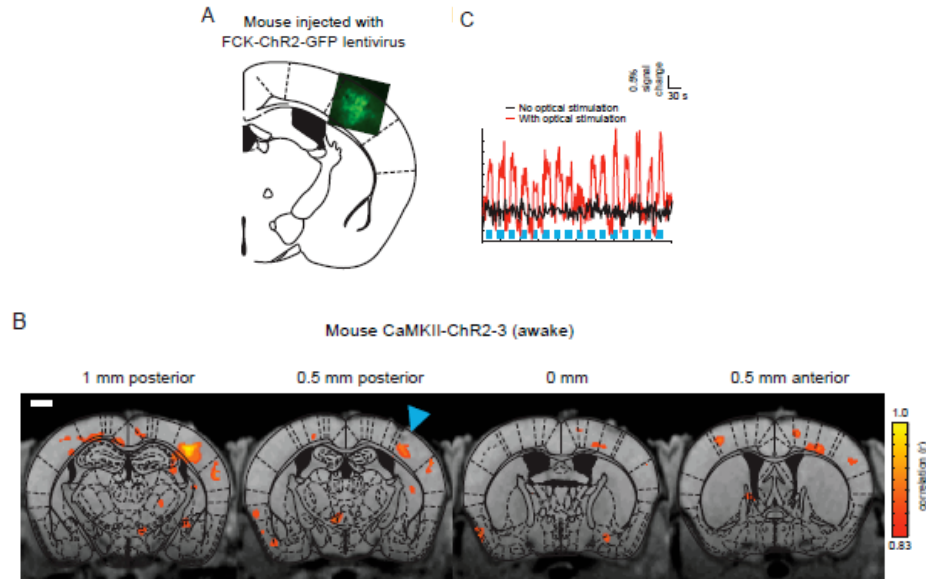


**Figure 5.3. Demonstration of ‘Opto-fMRI’ methodology in awake mice. A,** Chr2-GFP expression, overlaid on a mouse atlas (Paxinos and Watson, 1998) in a representative mouse injected with FCK-ChR2-GFP lentivirus in left hemisphere SI (bregma AP -1.0 mm, ML 3 mm, DV -0.7 mm). **B,** Voxels with significant increases in BOLD signal are indicated for the representative mouse (same as **A**) undergoing opto-fMRI. The image in **B** shows the voxels with significant increases in signal; voxel color indicates the boxcar correlation of the voxel; the data are shown for each of four 0.5 mm thick EPI slices ( $150 \mu\text{m} \times 150 \mu\text{m} \times 500 \mu\text{m}$  voxel resolution), overlaid over corresponding 0.5 mm thick single slice T1 anatomical images (these slices are shown from posterior to anterior, displayed from left to right). Scale bar in the figure, and subsequent figures, is 1 mm. Blue triangle indicates illumination site. The time course of SI activation for the representative mouse in **B** is plotted in **C** (red trace), averaged across all 4 scans of an opto-fMRI session. The black trace in **C** is the time course of SI activation (same set of contiguous voxels as for the red trace), when the laser was not on.

Opto-fMRI was performed on awake mice that had undergone viral infusion of the excitatory neuron-targeting lentivirus FCK-ChR2-GFP (Han et al. 2009) into the SI barrel cortex. These mice expressed ChR2-GFP in pyramidal neurons within a spherical volume between 700 and 1000  $\mu\text{m}$  in diameter, containing neurons distributed in layers 2/3 and layer 5 (**Fig. 5.3 A**). On illumination of SI pyramidal cells, we observed robust, distributed BOLD responses in the brain ipsilateral and contralateral to the fiber illumination site, time locked to the illumination period. **Figure 5.3 B** shows the results from a representative awake mouse. The time series of evoked BOLD signals in SI is plotted for this mouse in **Figure 5.3 C** (red trace). When the laser was not on, there was no visible change in the SI BOLD signal (**Fig. 5.3 C**, black trace).

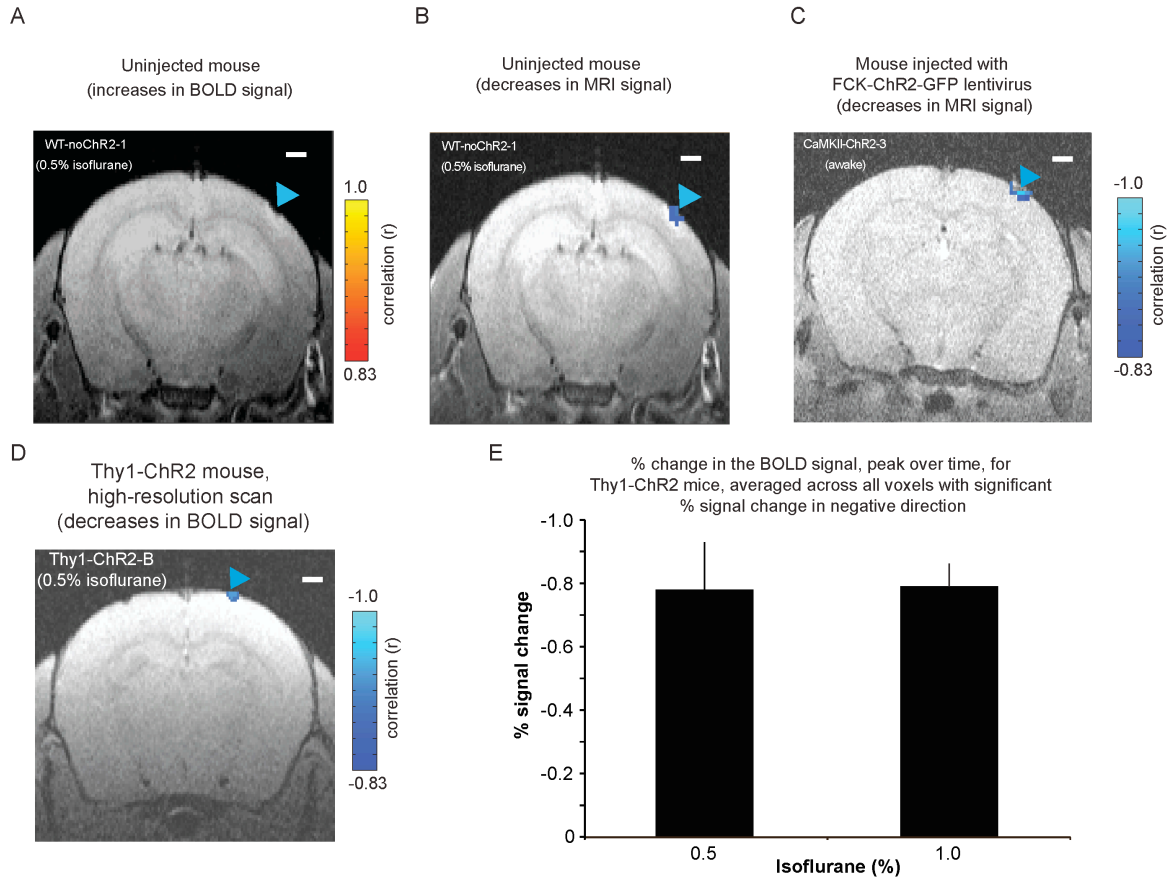


**Figure 5.4. Positive and negative signals revealed by opto-fMRI in the presence and absence of ChR2.** **A**, Voxels with significant increase in BOLD signal, colored according to boxcar correlation, for a wild-type mouse (non-ChR2 bearing) undergoing opto-fMRI under 0.5% isoflurane and a laser power of 10 mW, superimposed upon the corresponding single-slice T1-anatomical image. Images were collected at 200  $\mu\text{m}$  x 200  $\mu\text{m}$  x 500  $\mu\text{m}$  voxel resolution. **B**, **C** and **D**, voxels with significant decreases in signal, colored according to boxcar correlation, for a wild-type mouse (non-ChR2 bearing; the same mouse as in **A**), for an FCK-ChR2-GFP lentivirus injected mouse undergoing opto-fMRI (150  $\mu\text{m}$  x 150  $\mu\text{m}$  x 500  $\mu\text{m}$ ; 5 mW laser power), and for a Thy1-ChR2 transgenic mouse undergoing opto-fMRI under 0.5% isoflurane (200  $\mu\text{m}$  x 200  $\mu\text{m}$  x 500  $\mu\text{m}$ ; 10 mW laser power). Scale bar is 1 mm. Blue triangle indicates illumination site. **E**, Negative signal, (at the peak, after timecourses of BOLD signal change were averaged across all significantly-decreased voxels within SI), for four Thy1-ChR2 mice for which isoflurane was varied (0.5% and 1.0%).

Once again (as in **Chapter 4**), we did not detect positive BOLD responses in control mice not expressing ChR2, undergoing opto-fMRI (**Fig. 5.4 A**; n = 2 mice; representative mouse shown). This control experiment mitigates the possibility that positive BOLD responses were produced by non-ChR2 related effects of cortical laser illumination, such as any potential temperature changes induced by illumination. As reported in **Chapter 4**, a putative negative BOLD response was observed in the brain during opto-fMRI in the SI barrel cortex immediately under the optical fiber tip (**Fig. 5.4 C**). This negative signal response was similar in ChR2-negative mice (**Fig. 5.4 B**). MRI signal reductions were also observed in Thy1-ChR2 mice (**Fig. 5.4 D**), localized to the region of the brain just under the fiber tip. In Thy1-ChR2 mice we varied the isoflurane concentration from 0.5% to 1.0% while illuminating SI in ChR2-expressing Thy1 mice. We saw no effect of isoflurane level on the peak percent change in the BOLD signal for voxels that significantly decreased in MRI signal (**Fig. 5.4 D**;  $p > 0.90$ , paired t-test; n = 4 mice) in Thy1-ChR2 mice where isoflurane is changed from 0.5% to 1.0%. Thus, multiple independent lines of experiments support the idea that MRI signal reductions observed during light delivery to the brains of ChR2-expressing mice are not due to ChR2-mediated neural activation, but instead reflect a direct effect of light on the sample.

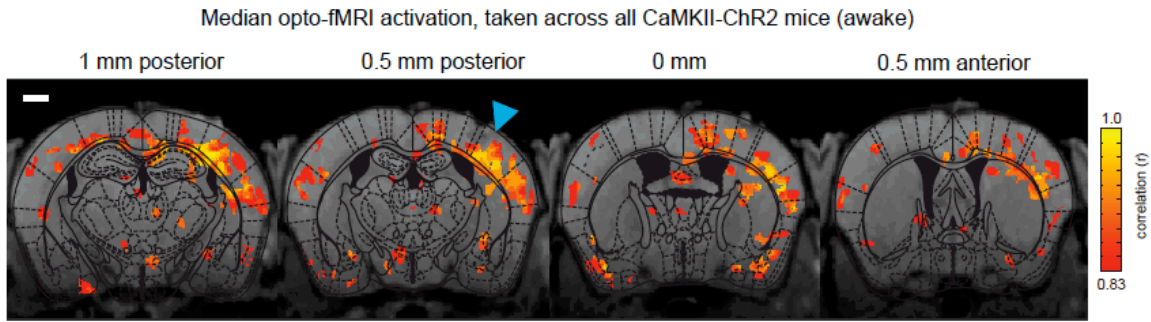


**Figure 5.5. Mapping of neural targets recruited by SI pyramidal cell activation in the awake mouse brain.** Population data for 5 mice undergoing awake opto-fMRI. The image in **A** shows the voxels with significant increases in signal in any animal. Voxel color indicates the median of the boxcar correlation, taken across all animals for which that voxel exhibits a statistically significant increase, for the voxel. The data are shown for each of four 0.5 mm thick EPI slices ( $150\ \mu\text{m} \times 150\ \mu\text{m} \times 500\ \mu\text{m}$  voxel resolution), overlaid over corresponding 0.5 mm thick single slice T1 anatomical images (these slices are shown from posterior to anterior, displayed from left to right). Scale bar in the figure is 1 mm. Blue triangle indicates illumination site.

To characterize the consistency of the opto-fMRI map across different mice, we performed opto-fMRI on five awake mice, each injected with 1 mL FCK-ChR2-GFP lentivirus in SI of the left hemisphere. To facilitate this comparison, the resultant functional scans were aligned for each mouse to its respective T1 anatomical scan, and then these datasets were cross-registered across all mice. All mice exhibited BOLD activations in the illuminated SI, and also displayed activations in nearby cortical regions, subcortical regions, and in the contralateral cortex. Voxels that were significant in any of the five mice are color-coded according to the median (taken across mice) boxcar correlation value in **Figure 5.5** (raw datasets for all five mice are shown in **Fig. 5.6**).

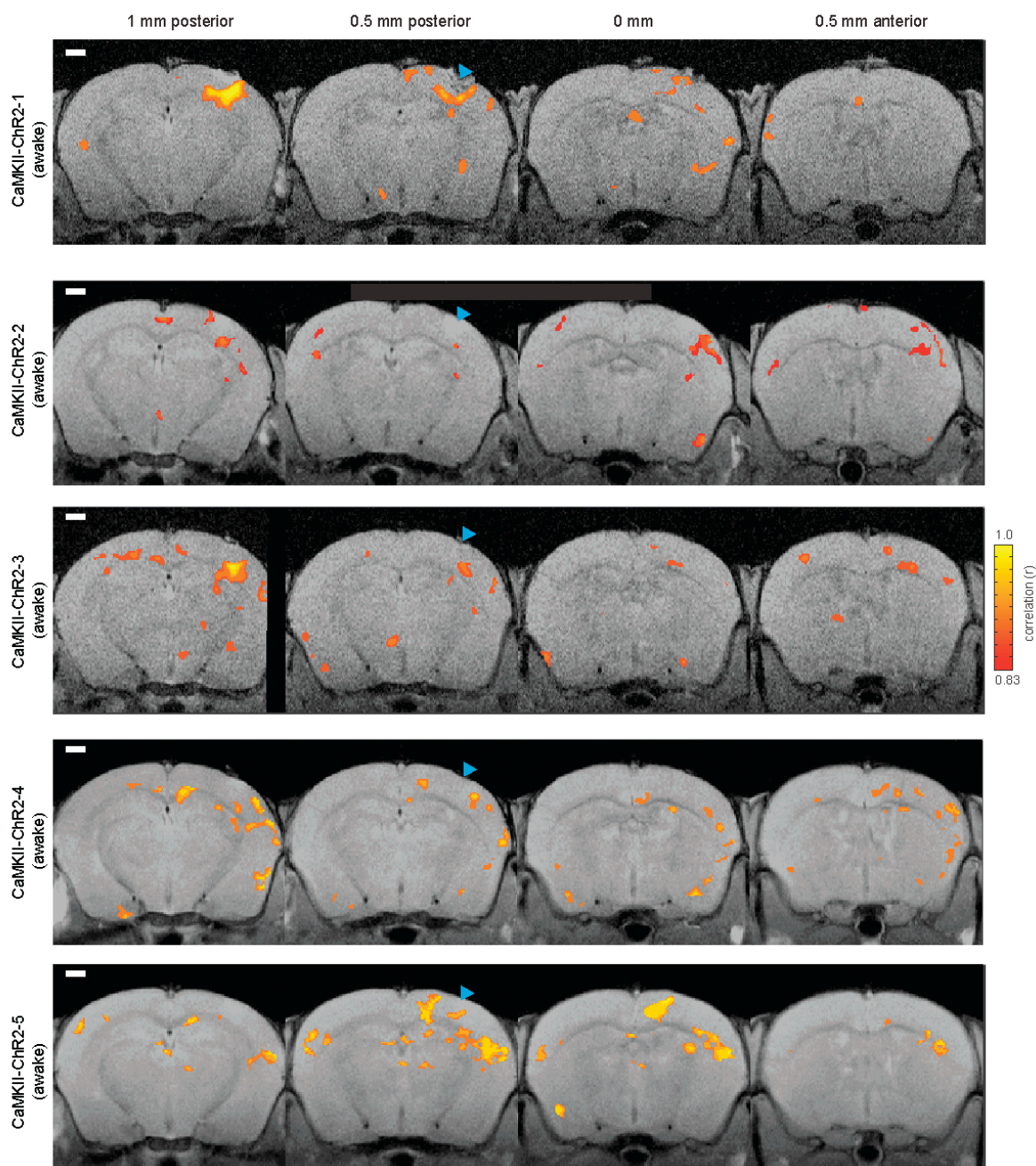


**Figure 5.6. Raw opto-fMRI data for all 5 individual mice expressing ChR2 in SI and imaged awake.** Four boxcar correlation+T1 anatomy images, plotted as in Fig. 1Bii, are shown, for each mouse (shown from posterior to anterior, displayed from left to right), for each of the five FCK-ChR2-GFP lentivirus injected mice. Functional images are collected at a resolution of  $150\ \mu\text{m} \times 150\ \mu\text{m} \times 500\ \mu\text{m}$  (5 mW laser power). Scale bar in the figure is 1 mm. Blue triangle indicates illumination site.

### **5.3.3. Neural targets recruited by SI pyramidal cell activation can be automatically identified**

To identify, in an unbiased manner, the brain regions downstream of SI activation, we developed an unsupervised algorithm that first clusters sets of contiguous significantly activated voxels into regions of interest (ROIs), and then localizes the centroid of each ROI to a reference mouse atlas. The clustering algorithm was identical to the one described in **Chapter 4.2.5** and based on an automated variant of the k-means clustering algorithm, which adjusts the number of clusters according to objective statistical criteria, and revealed for the five opto-fMRI experiments here conducted, 11 ROIs (**Fig. 5.7 A**). Of these 11 ROIs, we designated five as key ROIs, which were robustly activated in all five mice (**Fig. 5.7 B**). The centroid-atlas alignment revealed these key ROIs as ipsilateral SI, contralateral SI (c-SI), ipsilateral primary motor cortex (MI), ipsilateral secondary somatosensory cortex (SII), and the caudoputamen (CP), regions known to be targets of SI pyramidal neurons (Aronoff et al. 2010; Carvell and Simons 1986; 1987; Chakrabarti and Alloway 2006; Diamond et al. 2008; Ferezou et al. 2007; Megevand et al. 2008; White and DeAmicis 1977). The algorithm also reported ROIs that were less consistent across individual mice (**Fig. 5.7 B**). These ROIs might represent additional activated circuits, for which the reliability of observation was not as high as the selected five key ROIs. For example, in a subset of the five opto-fMRI experiments, clusters emerged in

regions that were atlas-aligned to thalamus and contralateral SII (**Fig. 5.7 A**; these activated regions were also visible in the raw datasets shown in **Fig. 5.6**). This variability could result from natural variations in the strength of connectivity of circuits from one brain to another, from subtle variations in the location of virally labeled neurons or of the placement of the optical fiber across mice, or from the fact that in our algorithm, the choice of a boxcar correlation statistical threshold could admit significant voxels for some mice but reject others, leading to a perceived heterogeneity across mice.

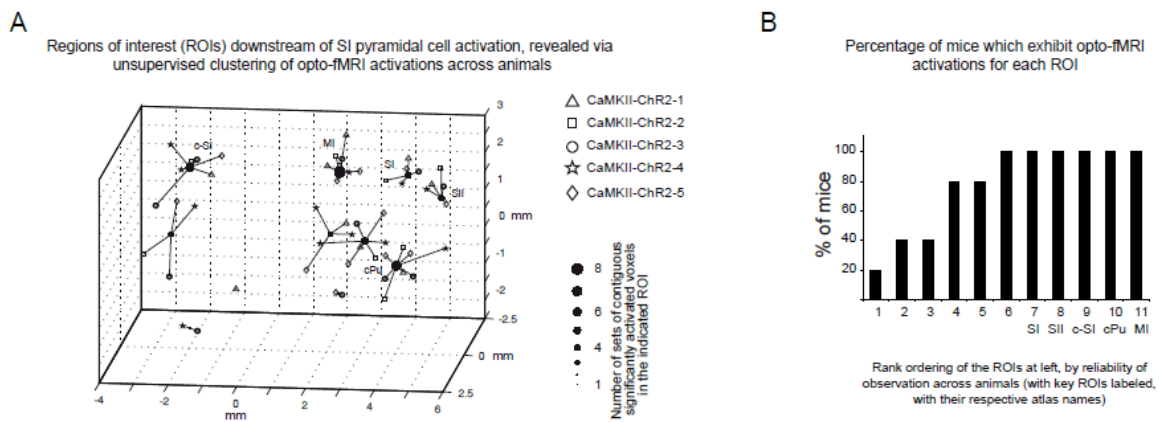


**Figure 5.7. Unbiased algorithmic mapping in the awake mouse brain. A,** Plot of regions of interest that are consistently activated across mice during SI pyramidal cell activation, generated by an unsupervised k-means clustering of all sets of contiguous significantly activated voxels obtained during the opto-fMRI experiment performed in **Figure 5.5**. Each filled circle indicates the centroid of a k-means derived cluster, and is connected to the sets of contiguous significantly activated voxels that make up this cluster; each of these sets of contiguous significantly activated voxels is marked by an open symbol, localized to the location of the peak correlation voxel for that set of contiguous significantly activated voxels. The shape of the open symbol indicates which animal the set of contiguous significantly activated voxels is from. K-means derived clusters were considered as regions of interest (ROIs), with key ROIs (annotated based upon what they correspond to in the atlas) labeled as SI (SI barrel field), c-SI (contralateral SI), SII (secondary sensory cortex), MI (motor cortex), and CP

(caudoputamen). **B**, Percentage of mice which exhibit opto-fMRI activations for each of the 11 ROIs generated in the k-means clustering of **A**, rank ordered, from left to right, by reliability of observation across animals.

To assess statistical robustness, we repeated the opto-fMRI algorithm on boxcar correlation maps obtained by varying the uncorrected boxcar correlation  $p$ -value to values 5x higher and 5x lower than that used in **Figure 5.7**. We found that varying the uncorrected boxcar correlation  $p$ -value to 0.001 or 0.025 resulted in few qualitative changes in the appearance of the correlation maps (representative mouse shown in **Fig. 5.8 Ai**; median boxcar correlation map shown in **Fig. 5.8 Aii**). When we ran the unsupervised neural target identification algorithm on the opto-fMRI data, few differences emerged in the cluster map, with key ROIs preserved (**Fig. 5.8 B** and **C**), and with most clusters remaining centered at the same location but expanding or contracting as the  $p$ -value was relaxed or made stricter. Our algorithm thus exhibits robustness to variations in the specific  $p$ -value chosen for the initial boxcar correlation threshold, indicating its utility in comparing neural maps across animals and across experiments.

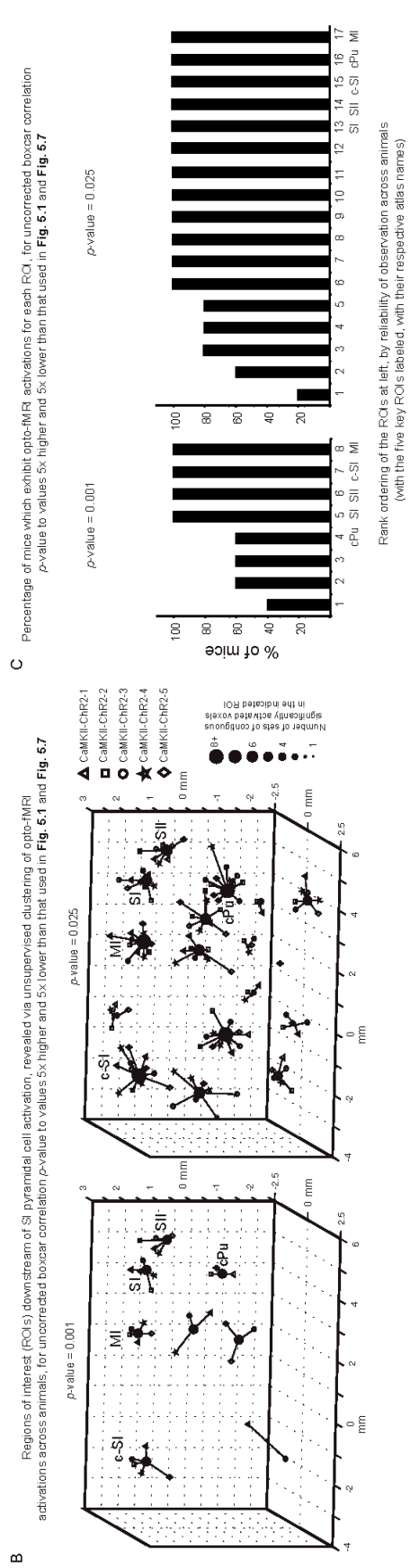
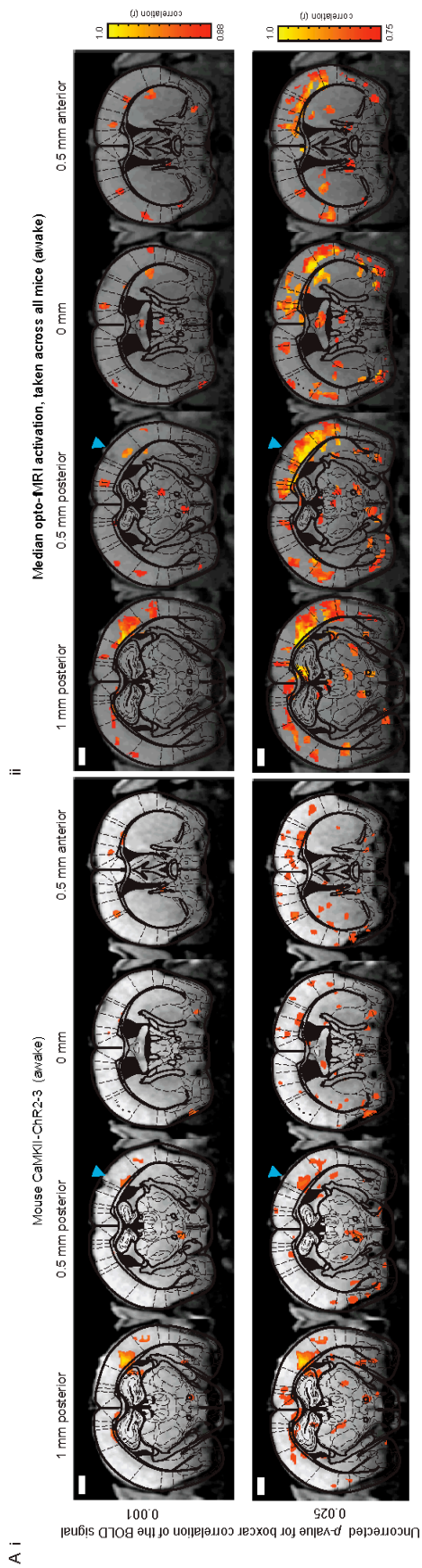


**Figure 5.8. Robustness of the algorithmic component of the opto-fMRI mapping process.** **A, i**, voxels with significant increases in BOLD signal are indicated for the representative mouse displayed in **Fig. 5.3**, but varying the boxcar correlation  $p$ -value to different levels. Shown in **Aii** is the population data ( $n = 5$  mice) similar to **Fig. 5.5**, but varying the boxcar correlation  $p$ -value to different levels. Scale bar in the figure is 1 mm. Blue triangle indicates illumination site. **B**, Regions of interest (ROIs) downstream of SI pyramidal cell activation, revealed via unsupervised clustering of opto-fMRI activations across animals, for uncorrected boxcar correlation  $p$ -value to values 5x higher (0.025) and 5x lower (0.001) than that used in **Fig. 5.7**. **C**, Percentage of mice which exhibit opto-fMRI activations for each of the ROIs generated in the k-means clustering for the two uncorrected  $p$ -values in **B**, rank ordered, from left to right, by reliability of observation across animals.

#### **5.3.4. Opto-fMRI evokes a greater BOLD response in awake than anesthetized animals**

We anticipate a major use of opto-fMRI will be in awake animals, given the potential for comparing animal opto-fMRI data to human fMRI data (which is predominantly collected in the awake state) and for understanding behavior in head-posted rodents, an approach that has recently been optimized for a variety of imaging modalities (e.g. (Andermann et al. 2010)Andermann et al. 2010). To demonstrate the use of opto-fMRI in analyzing how light-activated neural networks can be modulated, we compared, for the five mice analyzed in **Figure 5.5**, how administration of 0.7% isoflurane varied the network impact of SI illumination. Isoflurane was chosen because it is commonly used in small animal fMRI to prevent motion artifacts and immobilization stress (King et al. 2005; Lahti et al. 1998; Sicard et al. 2003), and it was also the anesthetic used in an earlier opto-fMRI study ((Lee et al. 2010)). The role that isoflurane anesthesia (or

any anesthesia) has on local versus global network dynamics, and on the coupling of these neural signals to blood flow, is controversial (Corfield et al. 2001; Matta et al. 1999; Tsurugizawa et al. 2010).

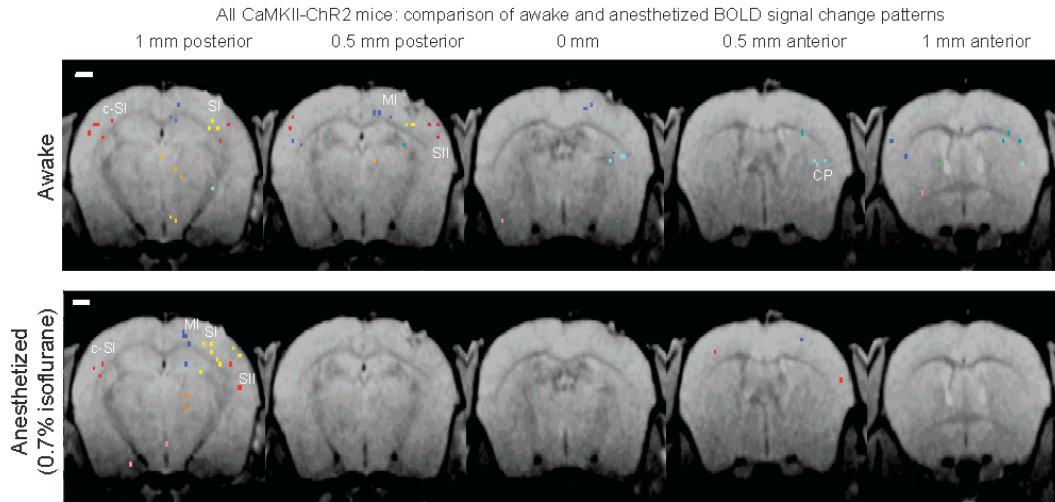


**Figure 5.9. Opto-fMRI analysis of brain state modulation of causal network dynamics: effects of anesthesia on SI network recruitment.** Overlay of the sets of contiguous significantly activated voxels, color-coded by ROI membership, onto T1 anatomical images, in the awake (*Top*) and 0.7% isoflurane anesthetized (*Bottom*) state (see Supp. Fig. 3 for raw datasets). For each set of contiguous significantly activated voxels, a colored point is displayed, localized to the location of the peak correlation voxel for that set of contiguous significantly activated voxels. Scale bar, 1 mm.

To visualize the effects of anesthesia on the set of regions causally recruited by SI, we plot in **Figure 5.9** the clusters or ROIs identified by the algorithm described above, for the awake (*top*) and anesthetized (*bottom*) states. Datasets leading up to these ROI plots, akin to those shown for the awake state in **Figure 5.5**, are shown in **Figure 5.10**. In the anesthetized state, only 6 ROIs were activated, as compared to the 11 ROIs in the awake state. Of the five key ROIs

identified in the awake state (SI, c-SI, SII, MI and CP), four were represented in the anesthetized state, but the striatal response was less prominent. This finding is consistent with previous studies using electrophysiology (Detsch et al. 2002; West 1998) reporting that anesthesia suppresses somatosensory-evoked information transfer to subcortical regions.

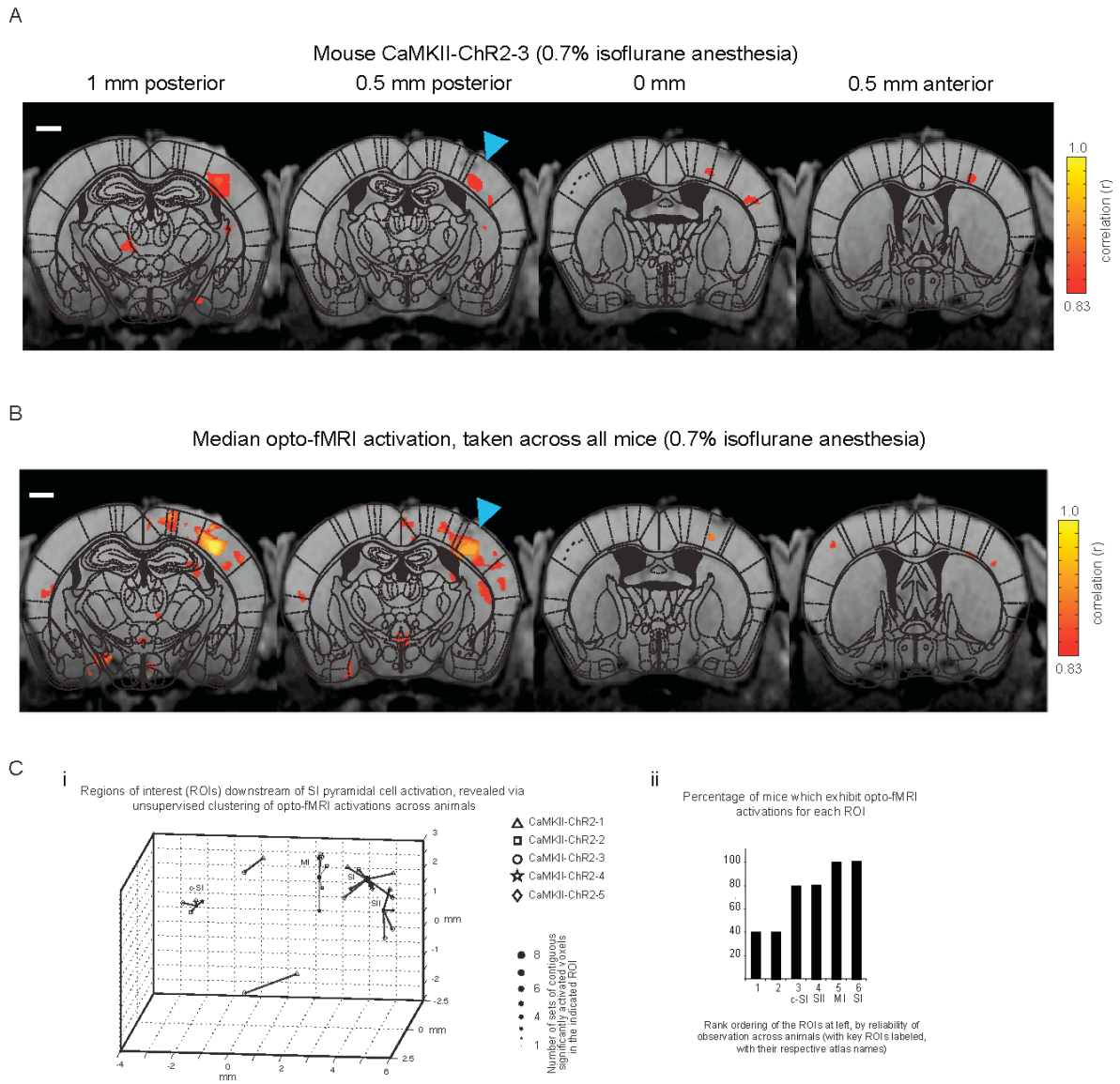


**Figure 5.10. Unbiased algorithmic mapping of neural targets recruited by SI pyramidal cell activation in the anesthetised mouse brain. A. Voxels with**

significant increases in BOLD signal are indicated for the representative mouse (same as in **Fig. 5.3**) that is anesthetized (0.7% isoflurane concentration) and undergoing opto-fMRI. Voxel color in **A** indicates the boxcar correlation of the voxel. **B**, Population data for 5 anesthetised (0.7% isoflurane concentration) mice undergoing opto-fMRI (same mice as in **Fig. 5.3**). The image in **B** shows the voxels with significant increases in signal in any animal. Voxel color indicates the median of the boxcar correlation, taken across all animals for which that voxel exhibits a statistically significant increase, for the voxel. The data are shown for each of four 0.5 mm thick EPI slices (150  $\mu\text{m}$   $\times$  150  $\mu\text{m}$   $\times$  500  $\mu\text{m}$  voxel resolution), overlaid over corresponding 0.5 mm thick single slice T1 anatomical images (these slices are shown from posterior to anterior, displayed from left to right). Scale bar in the figure is 1 mm. Blue triangle indicates illumination site. **C, i**, Plot of regions of interest that are consistently activated across mice during SI pyramidal cell activation, generated by an unsupervised k-means clustering of all sets of contiguous significantly activated voxels obtained during the opto-fMRI experiment performed in **B**. Each filled circle indicates the centroid of a k-means derived cluster, and is connected to the sets of contiguous significantly activated voxels that make up this cluster; each of these sets of contiguous significantly activated voxels is marked by an open symbol, localized to the location of the peak correlation voxel for that set of contiguous significantly activated voxels. The shape of the open symbol indicates which animal the set of contiguous significantly activated voxels is from. K-means derived clusters were considered as regions of interest (ROIs), with key ROIs (annotated based upon what they correspond to in the atlas) labeled as SI (SI barrel field), c-SI (contralateral SI), SII (secondary sensory cortex), MI (motor cortex), and CP (caudate/putamen) respectively. **Cii**, Percentage of mice which exhibit opto-fMRI activations for each of the 11 ROIs generated in the k-means clustering of Supp. **Fig. 5.5**, rank ordered, from left to right, by reliability of observation across animals.

In the isoflurane anesthetized condition there was also a decrease in the BOLD response for the voxels in all five key ROIs identified in the awake state (**Fig. 5.11 A and B**;  $F(1,40) = 172.63$ ,  $p < 0.0001$ , main effect of anesthesia level in a two-way ANOVA of anesthesia level  $\times$  region;  $F(4,40) = 7.830$ ,  $p < 0.0001$ , main effect of region in a two-way ANOVA of anesthesia level  $\times$  region; no

interaction,  $F(4, 40) = 0.558$ ,  $p = 0.6943$ ). These contrasts show the potential utility of opto-fMRI for probing dynamics in network activation.

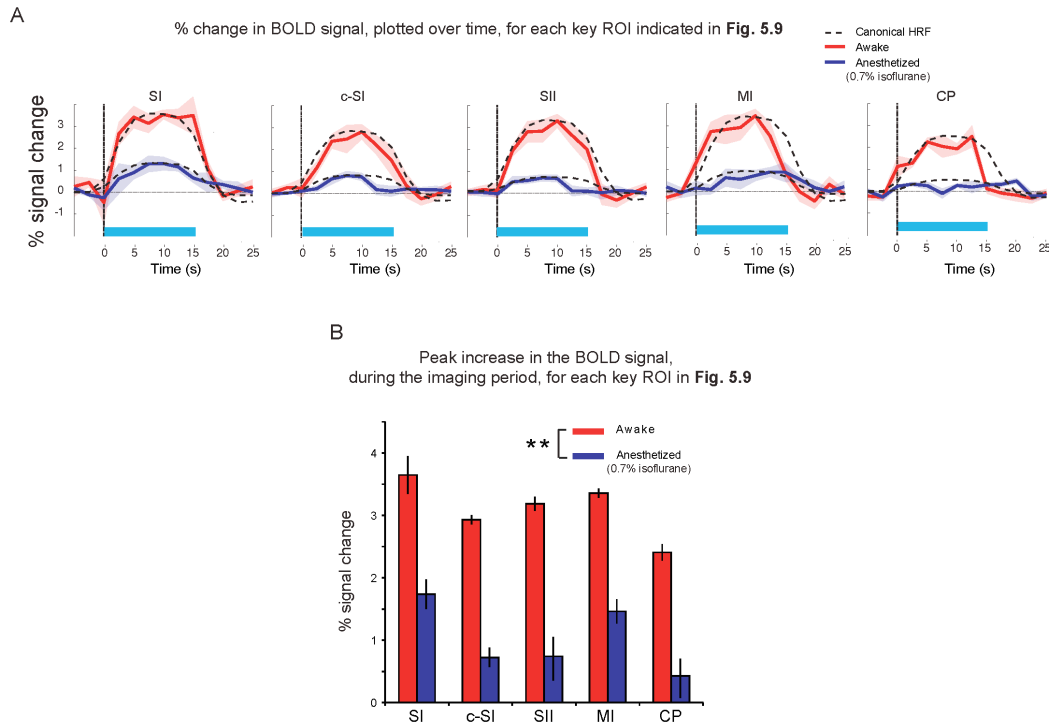


**Figure 5.11. Opto-fMRI analysis of brain state modulation of causal network dynamics: effects of anesthesia on induced BOLD response.** **A**, Percent change in the BOLD signal, plotted over time, for each key ROI indicated by a label in Fig. 5.3. The BOLD signal time course was averaged across all pulse trains within a session (consisting of 4 scans, of 16 pulse trains each), then across all the voxels within the contiguous significantly-activated voxels associated with each key ROI. Solid lines indicate the average of the percent signal change, taken across animals, for awake (red) and anesthetized (blue) states; shaded areas indicate the standard error of percent signal change ( $n = 5$  mice). The dashed curves in B represent scaled canonical hemodynamic response functions (HRFs) fitted to the BOLD signal time course for each of the ROIs, in either the awake (red) or anesthetized (blue) state. **B**, Peak percent change in the BOLD signal for the experiments plotted in **A**. \*\*,  $p < 0.0001$ , factor of anesthesia level (two-way ANOVA of anesthesia level  $\times$  region).

To address the question of how the timecourse of the BOLD response is altered by anesthesia administration, we examined the goodness-of-fit of BOLD responses in different regions under different levels of anesthesia to the canonical hemodynamic response function (HRF). The BOLD response in SI was well fit with the canonical HRF in the awake state (**Fig. 5.11 A**, dotted line superimposed upon red trace in left plot;  $R^2 = 0.94$ ,  $F(1,4) = 21.37$ ,  $p = 0.0002$ ,  $n = 5$  mice; least square linear regression, allowing only the amplitude scaling of the HRF to vary, as well as the amplitude offset, but not allowing for scaling or shifting of the HRF along the time axis). Indeed, all of the awake responses were well fit with the canonical HRF ( $R^2$  ranging from 0.78 to 0.94,  $F(1,4)$  ranging from 7.28 to 21.37,  $p$ -values ranging from 0.0002 to 0.009; dotted lines superimposed upon red trace in each plot of **Fig 5.11. A**). The anesthetized responses were less well fit by the HRF ( $R^2$  ranging from 0.15 to 0.90,  $F(1,4)$  ranging from 1.57 to 17.57,  $p$ -value ranging from 0.0008 to 0.27).

To apply a direct statistical comparison of the goodness-of-fit to the HRF for the awake and anesthetized BOLD signal changes, we computed an  $R^2$  for every opto-fMRI session BOLD signal vs. the HRF. In our first analysis we computed this  $R^2$  using the default value of delay in HRF (6 s relative to onset) and then through Fisher's z-transform computed the z-score for the goodness-of-fit to the HRF. We then ran an ANOVA to test how these z-scores varied across anesthesia level and region. We found that anesthesia significantly lowered the z-score for the goodness-of-fit to the HRF of the BOLD signal relative to the awake state ( $F(1,40) = 167.62$ ,  $p < 0.0001$ , main effect of anesthesia level in a two-way

ANOVA of anesthesia level  $\times$  region), and regions also differed in their match to the HRF ( $F(4,40) = 34.42, p < 0.0001$ , main effect of region in a two-way ANOVA of anesthesia level  $\times$  region). There was a significant interaction between anesthesia level and region ( $F(4,40) = 7.28, p = 0.0002$ ). Specifically, local SI activity was least affected in its BOLD signal response shape by anesthesia (z-score for the goodness-of-fit to the HRF decreased from 2.07 to 1.59), whereas the striatum was most affected (z-score for the goodness-of-fit to the HRF decreased from 1.48 to 0.35). In a second analysis we varied the delay parameter for the HRF from 1 to 12 s, and recomputed the  $R^2$  for each fit, to determine the delay that would result in the highest  $R^2$  value. We found that anesthesia significantly increased the delay in HRF that resulted in the peak  $R^2$ , relative to the best-fit delay seen for the awake state ( $F(1,40) = 98.33, p < 0.0001$ , main effect of anesthesia level in a two-way ANOVA of anesthesia level  $\times$  region), and regions also differed in their delay in HRF that would result in peak  $R^2$  ( $F(4,40) = 11.04, p < 0.0001$ , main effect of region in a two-way ANOVA of anesthesia level  $\times$  region). There was a significant interaction between anesthesia level and region ( $F(4,40) = 18.96, p < 0.0001$ ), in this delay computation.

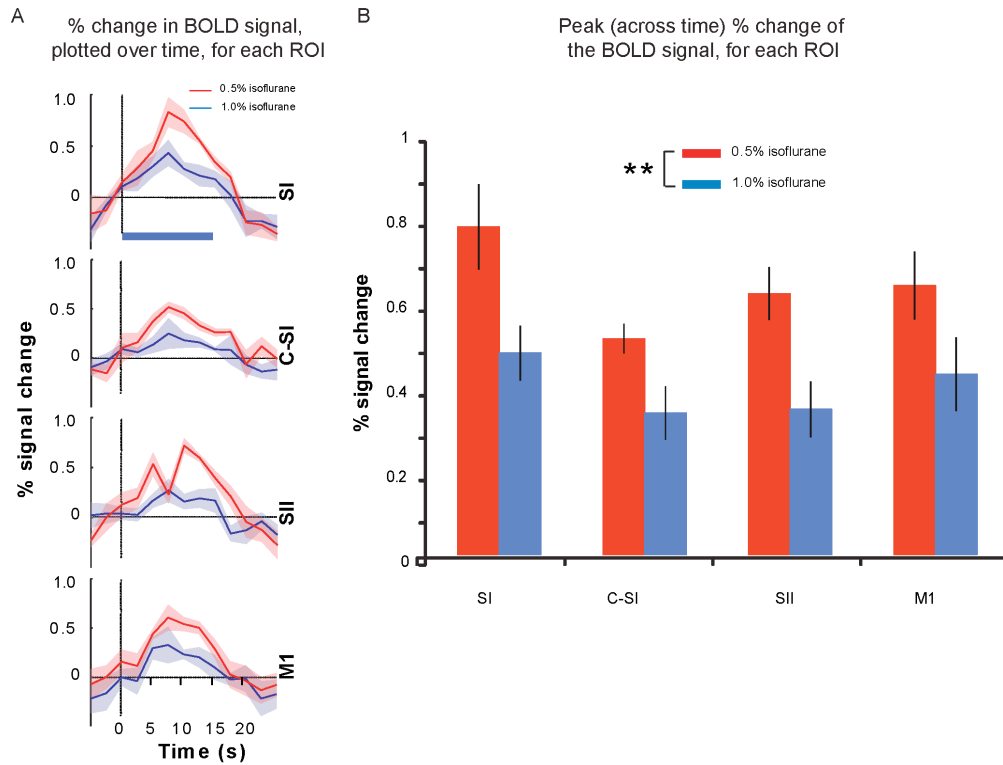


**Figure 5.12. Opto-fMRI analysis of brain state modulation of causal network dynamics: effects of anesthesia on induced BOLD response in Thy1-ChR2 mice.** **A**, Percent change in the BOLD signal, plotted over time, as in **Figure 5.11 A**. Solid lines indicate the average across animals of the percent signal change, for 0.5% isoflurane (red) and 1.0% isoflurane (blue); shaded areas indicate the standard error across animals of percent signal change;  $n = 4$  mice. **B**, Peak percent change in the BOLD signal for the timecourses plotted in **A**. \*\*,  $p < 0.005$ , factor of anesthesia level (two-way ANOVA of anesthesia level  $\times$  region).

We performed a similar experiment in Thy1-ChR2 mice ( $n = 4$ ), where the anesthesia level was set at 0.5% or 1.0%, as indicated by end-tidal isoflurane level. At increased isoflurane levels (1.0%, compared to 0.5%), we observed a decreased amplitude of the BOLD response for four ROIs under consideration, without overtly altering the shape or temporal dynamics of the response (**Fig. 5.12 A**), which is consistent with previously reported studies (Cohen et al. 2002; Nair

and Duong 2004). When we quantified the temporal peak of the Opto-fMRI assessed change in BOLD signal for each of the four mice, we find that the amplitude of this peak was not different across regions ( $p > 0.15$ ,  $F(1,24) = 1.675$ , factor of region in a two-way ANOVA of anesthesia level  $\times$  region), but was significantly downmodulated by increased anesthesia ( $p < 0.001$ ,  $F(1,24) = 15.265$ , factor of anesthesia level in a two-way ANOVA of anesthesia level  $\times$  region; no interaction between the two factors,  $p > 0.95$ ).

### **5.3.5. Anesthesia affects BOLD functional connectivity in the network recruited by pyramidal cell activation**

We applied opto-fMRI to probe the functional connectivity of the brain network downstream of SI as a function of brain state, again using isoflurane anesthesia as a model. We performed normalized cross-correlation analyses of the BOLD signal changes in different ROIs during opto-fMRI. This technique provides a measure of temporal correlation across regions while nullifying the effect of absolute changes in signal amplitude (as reported above), allowing focus on how anesthesia level modulates the coordination between regions. We found that the anesthetized state had generally lower normalized cross-correlations between pairs of regions than did pairs of regions in the awake state (**Fig. 5.13**,  $F(1,80) = 71.67$ ,  $p < 0.0001$ , main effect of anesthesia level in a two-way ANOVA of anesthesia level  $\times$  region pair). This measure of correlation also varied between different pairs of regions ( $F(9,80) = 4.76$ ,  $p < 0.0001$ , main effect

of region in a two-way ANOVA of anesthesia level  $\times$  region pair), and no interaction between the two factors,  $F(9, 80) = 1.22, p = 0.29$ ).

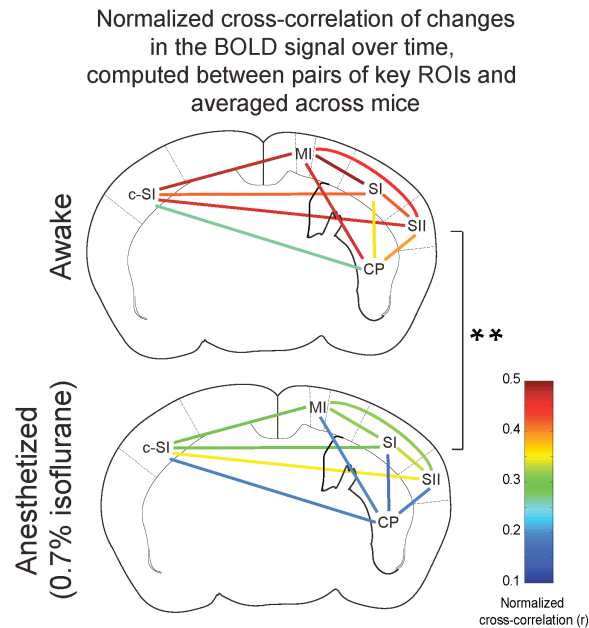


**Figure. 5.13. Opto-fMRI analysis of brain state modulation of causal network dynamics: effects of anesthesia on functional connectivity.** Normalized cross-correlations of the time series of percent change in the BOLD signal, taken between pairs of key ROIs in the awake (*Top*) and anesthetized (*Bottom*, 0.7% isoflurane) states; normalized correlations were computed for each animal, then averaged across animals, and plotted on a continuous color scale. \*\*,  $p < 0.0001$ , factor of anesthesia level (two-way ANOVA of anesthesia level  $\times$  pairs of ROI).

The striatum showed lower correlations with other regions than did other pairings. The 17 post-hoc tests of differences between the awake and anesthetized state that showed  $p$ -values using Fisher's PLSD test significant with respect to a 0.05 significance level, all involved the striatum. When we

computed, for each region, the average normalized cross-correlation between the striatum and all the other regions, we found that this “total connectivity” was lowered by anesthesia ( $F(1, 40) = 86.50, p < 0.0001$ , main effect of anesthesia level in a two-way ANOVA of anesthesia level  $\times$  region pair). Different regions also exhibited different total levels of connectivity with the rest of the network ( $F(4,40) = 3.39, p < 0.02$ , main effect of region in two-way ANOVA of anesthesia level  $\times$  region pair; no interaction,  $F(4,40) = 0.76, p > 0.55$ ), with the striatum exhibiting less total connectivity than the others ( $p < 0.02$ , Fisher’s PLSD, comparison with all other regions).

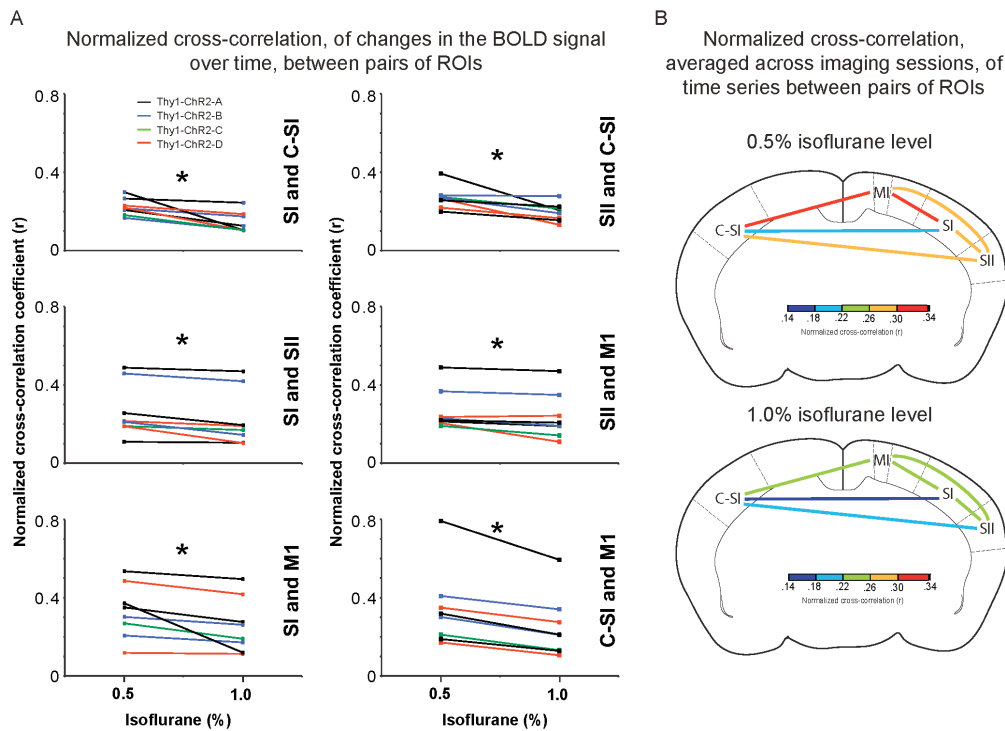


**Figure 5.14. Opto-fMRI analysis of brain state modulation of causal network dynamics: effects of anesthesia on functional connectivity in Thy1-ChR2 mice.** **A**, Normalized cross-correlation of the percent change in the BOLD signal

over time for four Thy1-ChR2 mice in which isoflurane was manipulated, analyzing pairs of ROIs at 0.5% and 1.0% isoflurane concentrations. \*,  $p < 0.01$ , factor of anesthesia level (two-way ANOVA of anesthesia level  $\times$  pairs of ROI). **B**, Normalized cross-correlation of time series between ROIs as in A, but now averaged across imaging sessions, and plotted for all 0.5% experiments (top) and all 1% experiments (bottom).

We performed normalized cross-correlation analyses of the time series of the BOLD signal changes, obtained in different regions of interest, for the four Thy1-ChR2 mice that underwent opto-fMRI at 0.5% and 1.0% isoflurane concentration. We found that increasing anesthesia level reduced the normalized cross-correlation of optically-driven activations, taken between pairs of regions (**Fig. 5.14 A**;  $p < 0.01$ ,  $F(1,84) = 6.957$ , factor of anesthesia level in a two-way ANOVA of anesthesia level  $\times$  region). We also found a trend towards regional differentiation of correlation strength with other parts of the network (**Fig. 5.14 B**;  $p < 0.1$ ,  $F(5,84) = 1.93$ , factor of region in a two-way ANOVA of anesthesia level  $\times$  region; no interaction between the two factors,  $p > 0.95$ ). These results suggest that anesthesia level modulates functional network connectivity, and demonstrate the ability of Opto-fMRI to resolve changes in network correlation due to brain state changes, in defined target networks of a site.

## 5.4. Discussion

Optogenetic strategies using ChR2 expression have previously been demonstrated to evoke a BOLD response in the anesthetized rat ((Lee et al. 2010) and **Chapter 4**). Here in this chapter we extend this work in three ways. First,

opto-fMRI is implemented on an awake mouse. The ability to perform opto-fMRI in the awake mouse opens up translational links between causal circuit studies in animals and behaviorally- and clinically-important human studies. Second, using photoactivation of cortical pyramidal cells of the mouse SI barrel cortex, which has well-characterized targets throughout the brain (Aronoff et al. 2010; Carvell and Simons 1986; 1987; Chakrabarti and Alloway 2006; Diamond et al. 2008; Ferezou et al. 2007; Megevand et al. 2008; White and DeAmicis 1977), we demonstrate that distributed regions of a network could be mapped by light stimulation and an unbiased, automated fMRI analysis. The network response included regions in the striatum, the motor cortex (MI), the contralateral primary sensory cortex (c-SI), and the secondary sensory cortex (SII). Third, functional connectivity measures demonstrated the BOLD response was correlated between regions within the network consistent with observations from evoked and intrinsic BOLD fluctuations in the human (Fox and Raichle 2007; Friston 1994; Hampson et al. 2006; Pezawas et al. 2005; Ramnani et al. 2004; Stephan et al. 2008; Van Dijk et al. 2010). The absolute magnitude of BOLD response in each region of the network and the functional correlation strengths between regions were attenuated by anesthesia. These results are again in line with the results obtained in **Chapter 3** where we see a dose dependent effect of isoflurane on the BOLD signal and the functional connectivity in the somatosensory network. The loss of CP response for 0.7% isoflurane condition is again corroborates with the observation made in Chapter 3, where there is a significant reduction in the functional connectivity between SI – putamen and SI –

caudate for higher depth of isoflurane. These collective results suggest that opto-fMRI provides an approach to map circuits in the awake mouse and thus complements fMRI approaches used *in-vivo* in humans.

The present chapter also provides a detailed account, intended to facilitate the implementation of this method by future researchers. A number of technical challenges were overcome to achieve the combination of optical neural activation and fMRI in the awake mouse. Specialized hardware for awake mouse imaging was implemented (**Fig. 5.1**) that enables positioning of optical fibers and immobilization without incurring significant motion artifacts, using a combination of head posts and restraint tubes. For the majority of the experiments in this paper, we chose to use  $150 \text{ mW/mm}^2$  irradiance, well within the range used for repeated stimulation (Ayling et al. 2009a; Cardin et al. 2009; Cardin et al. 2010; Kravitz et al. 2010; Zhang et al. 2010) and at the lower limit of what is needed to evoke EMG responses when targeting primary motor cortex (Ayling et al. 2009a); however, it will generally be useful to select the least dosage of light necessary for achieving a given scientific goal.

Opto-fMRI provides a strategy for characterizing the network downstream of a target in a fashion that is amenable to repeated assessment, potentially over extended time periods suitable to longitudinal study of learning and plasticity, and disease progression. Thus, this work complements recent studies by (Lee et al. 2010) in the rat discussed above and (Logothetis et al. 2010) in the monkey that used electrical stimulation to measure the BOLD response in distributed regions across the visual system. In the future, the addition of new technologies such as

optical neural silencing reagents (Chow et al. 2010; Han and Boyden 2007a; Zhang et al. 2007c; Zhao et al. 2008) or multisite illuminators, the targeting of different neuron types, and further improvements of fMRI, will augment the performance of opto-fMRI. Awake mouse opto-fMRI also opens up the possibility of implementing a psychophysical paradigm and assessing brain-wide effects of changing the psychometric threshold curves through optogenetically manipulating a specific subcircuit (e.g.,(Cardin et al. 2009).

There are also clear limitations to awake opto-fMRI studies - the need for a head-fixed animal. Head-fixed animals have been shown to have sparse firing rate in the sensory cortex when compared to freely moving animals (de Kock and Sakmann ; Sakata and Harris). The higher firing rate is thought be important for information processing in various ways, in a behaviorally relevant state (Vijayan et al. 2010).

Other approaches for mapping neural circuits in a causal fashion using fMRI exist. Electrical microstimulation has proven to be an important tool in combination with fMRI (Canals et al. 2008; Ekstrom et al. 2009; Logothetis 2003; Logothetis et al. 2010; Sultan et al. 2007; Tolias et al. 2005) for driving local circuits in the context of whole-brain mapping, but electrical activation can recruit a diversity of cell types within a microcircuit, as well as fibers of passage, smooth muscle, and other brain circuit elements (Ranck 1975). However, the passive spread of current can confound the analysis of functional connections (local and distal), as determined by fMRI, requiring indirect methods to characterize the current spread such as behavioral controls (Tehovnik et al. 2006). Future work

that directly compares stimulation methods will be valuable for understanding tradeoffs between methods, and resolve the uses of these tools in different spheres of neuroscience.



## Chapter 6. Characterization of the Functional MRI Response Temporal Linearity via Opto-fMRI

This chapter is adapted from a manuscript submitted:

Kahn I.\*, Mitul Desai.\*, Knoblich U.\*, Bernstein J., Graybiel A. M., Boyden E. S., Buckner R. L., & Moore C. I.; “Characterization of the Functional MRI Response Temporal Linearity via Optical Control of Neocortical Pyramidal Neurons”, *under review*.

\* These authors contributed equally

### 6.1. Introduction

The blood oxygenation level-dependent (BOLD) functional MRI (fMRI) signal (Kwong et al. 1992; Ogawa et al. 1990c) is widely used to study activity in the human brain. Because the BOLD response measures hemodynamic fluctuations, and not underlying electrophysiological signals directly, the relation between neural activity and the BOLD fMRI signal has been studied extensively (Boynton et al. 1996; Dale and Buckner 1997b; Heeger et al. 2000; Logothetis et al. 2001; Miezin et al. 2000; Mukamel et al. 2005; Rees et al. 2000; Shmuel et al. 2006; Viswanathan and Freeman 2007). With some caveats, most evidence links spike rate and the local field potential (LFP) with the BOLD response in the cortex (for reviews see, Heeger and Ress 2002; Logothetis 2008). Several studies have further demonstrated that, to a first approximation, the BOLD response has a linear relation to underlying spiking activity elicited by sensory stimulation (Boynton et al. 1996; Dale and Buckner 1997b; Logothetis et al. 2001; Miezin et al. 2000; Rees et al. 2000).

As demonstrated in **Chapter 4** and **Chapter 5**, we build on these prior studies by characterizing the somatosensory neocortical BOLD response in a mouse model that allows precise temporal control of neural activity, an ‘opto-fMRI’ approach. Some of the other recent demonstrations (Desai et al. 2010; Lee et al. 2010), has also combined activation of the microbial opsin channelrhodopsin-2 (ChR2), a light sensitive nonselective cation channel (Boyden et al. 2005b; Nagel et al. 2003), with high-field functional imaging (9.4 Tesla fMRI). In this chapter we employed the Thy1-ChR2-YFP mouse, in which ChR2 is predominantly expressed in layer V pyramidal neurons throughout the neocortex (Arenkiel et al. 2007). By targeting primary somatosensory (SI) cortex, we characterized the properties of the BOLD response as a function of pyramidal neuron spiking and tested the hypothesis that the local excitation of pyramidal neurons by optogenetic means recruits a BOLD response that can be modeled with a linear transform from underlying neural activity.

We tested whether the BOLD response evoked by closely temporally spaced short trains of optically driven pyramidal cell activity would summate linearly. We found that the BOLD response closely matched local pyramidal activity and added in an approximately linear fashion. These findings both inform our interpretation of the ‘classic’ sensory driven BOLD neocortical response, and provide a quantitative investigation of opto-fMRI BOLD signal.

## **6.2. Materials and Methods**

### **6.2.1. Animals**

All procedures were conducted in accordance with the National Institutes of Health guidelines and with the approval of the Committee on Animal Care at MIT. Channelrhodopsin-2 transgenic mice (Arenkiel et al. 2007) were purchased from the Jackson Labs (line 18, stock 007612, strain B6.Cg-Tg(Thy1-COP4/EYFP)18Gfng/J) and subsequently crossed with C57bl/6 mice. Electrophysiological recordings and fMRI were obtained in separate animals.

### **6.2.2. Animal Anesthesia and Surgery**

Animals were anesthetized with isoflurane mixed with oxygen for all procedures. During preparation and surgery anesthesia was kept at a level of 1-3%. Immediately prior to MRI scanning and electrophysiological recording the anesthetic level was reduced to 0.5-1% expired isoflurane. For the MRI experiments, the craniotomy was restricted to a burr-hole in the skull. For the electrophysiological recordings, the dura mater was opened after the craniotomy to allow positioning of the optical fiber and recording electrode.

### **6.2.3. Light stimulation**

Light stimulation was generated by a 473 nm laser (Shanghai Dream Lasers) controlled by a computer. Optical stimulation at 40 Hz frequency and 8 ms pulse duration was delivered via a 200  $\mu\text{m}$  diameter unjacketed optical fiber

with 0.48 NA (Thorlabs) at a range of 320-470 mW mm<sup>-2</sup> irradiance at the tip of the fiber, irradiance that can evoke EMG responses when targeting primary motor cortex (Ayling et al. 2009b). The fiber was positioned over SI barrel field (SIBF; Bregma AP -1.5, ML 2.5) at the cortical surface. We computed the dropout in light irradiance using a Monte Carlo simulation (Chow et al. 2010), with a simulated volume of 4 mm<sup>3</sup>, 20 μm<sup>3</sup> voxels, 5 million photons, scattering coefficient in gray matter at 473 nm of 10 mm<sup>-1</sup> (Yaroslavsky 2002), absorption coefficient of 0.07 mm<sup>-1</sup>, anisotropy factor of 0.88, and a uniform laser emission pattern over a half opening angle of 5 degrees, yielding blue light penetration to layer V of mouse cortex with about 90% irradiance loss, chiefly due to scattering of light (Bernstein et al. 2008). A 40 Hz train of stimulation with 8 ms pulse width was applied.

#### **6.2.4. Sensory stimulation**

A Piezoelectric (PZ) element (Noliac, Denmark: 5.0 cm × 0.78 cm × 0.18 cm) was used to deflect vibrissae. A glass capillary tube was used for extension (1 mm I.D. and 5 cm long) and a nylon thread was looped through the glass capillary tube. All the posterior vibrissae of the right facial pad were cinched at ~1 cm from the vibrissal pad. A 40 Hz sinusoidal wave was used to drive the PZ element, with a peak-to-peak motion amplitude calibrated to 347 ± 12 μm along the dorso-ventral direction.

### 6.2.5. MRI Procedures

Mice were fixed to an animal bed (Bruker BioSpin MRI GmbH) using a standard tooth-piece and ear bars. Breathing rate (Small Animal Monitoring 1025, SA Instruments) and expired isoflurane (V9004 Capnograph Series SurgiVet, Smiths Medical PM) were continuously monitored. Imaging was performed on a 9.4 Tesla BioSpec 94/20 USR MRI (Bruker BioSpin MRI GmbH) that operates at a maximum gradient strength of 675 mT/m, maximum slew rate 4673 T/m/s and a rise time of 130  $\mu$ s. A single transmit and receive surface coil consisting of a single copper loop and etched circuit board (20 mm diameter) was placed over the head. The fiber was placed on or  $\leq$  50 microns from the dura mater. In a subset of mice, the fiber slightly compressed the underlying neocortex. These animals produced data identical to that observed in other preparations, suggesting this slight compression did not appreciably impact the capacity of the optical stimulation to drive local cortical responses.

BOLD contrast scans were acquired using a spin-echo echo-planar sequence (repetition time = 2.5 s; echo time = 12.17 ms; 10 coronal slices, 200  $\mu$ m  $\times$  200  $\mu$ m  $\times$  500  $\mu$ m). High-resolution T<sub>1</sub>- and T<sub>2</sub>-weighted anatomical images were recorded using a rapid acquisition process with a relaxation enhancement (RARE) sequence in coronal orientations (10 coronal slices, 78  $\mu$ m  $\times$  78  $\mu$ m  $\times$  500  $\mu$ m). Image reconstruction was carried out using ParaVision 5.0 (Bruker BioSpin MRI GmbH). Preprocessing included compensation of slice-dependent time shifts, rigid body correction for motion within and across runs, and smoothing with a full-width half-maximum kernel of 600  $\mu$ m. For each

mouse in the fMRI component of the study, we conducted interleaved ‘localizer’ and ‘target’ runs. The SIBF region of interest (ROI) identified in the localizer runs was subsequently used to test temporal linearity in the target runs. For each localizer run, the images were detrended and percent signal change was computed by subtracting, from each voxel’s BOLD time series, the temporal average of all off periods for all scans in a session, dividing by the average of the signal across no-stimulation periods and then averaged across all localizer runs. Significant BOLD signal increases were determined by a voxel-wise time series correlation of the percent signal change with the protocol boxcar, delayed by one repetition time (TR; 2.5 s). Family-wise error corrected  $P$ -value of 0.05 was used. To achieve this threshold only clusters with at least six contiguous voxels and uncorrected  $P$ -values at  $P < 0.005$  were considered. The cluster size and  $P$  value threshold were determined via Monte Carlo simulations performed in AFNI using AlphaSim (Forman et al. 1995b; Xiong et al. 1995a).

To estimate the location of activated voxels in SIBF the EPI volumes were aligned to the T1 structural volumes using the AFNI `align_epi_anat.py` program. ROIs were identified by overlaying the structural images onto corresponding atlas plates (Paxinos and Franklin 2001), by aligning the anteroposterior coordinates and scaling the atlas plates along the x and y axes until the borders corresponded.

#### **6.2.6. Electrophysiology**

Mice were isoflurane anesthetized and held in place with a head post. A small craniotomy was made over SIBF. Stimulus control and single unit activity

(SUA) data acquisition were performed using software custom-written in LabView (National Instruments) and MATLAB (The Mathworks, Natick, MA). Glass-pipette pulled electrodes (10–14 M $\Omega$  resistance) were filled with saline and lowered under positive pressure while injecting small amplitude current pulses. Cell-attached recording configuration was achieved when a medium resistance seal ( $\geq 50$  M $\Omega$ ) was formed and spikes were observed (MultiClamp 700B, Molecular Devices). LFP and Multi-unit activity (MUA) recordings were obtained using 16 contacts (15  $\mu$ m diameter spaced 100  $\mu$ m apart) laminar electrodes (Neuronexus Technologies) connected to a Cheetah32 data acquisition system (Neuralynx). Recordings were performed under the most permissive filter settings (0.1–9000 Hz) and separated into LFP and MUA signals post hoc.

### **6.2.7. Electrophysiology Analysis**

Cell-attached recording data were band-pass filtered between 600 Hz and 6000 Hz and spike times were extracted where the potential exceeded 10 standard deviations of the signal calculated across the entire block. The MUA data were extracted from laminar recordings by band-pass filtering the signal between 600 Hz and 6000 Hz and spike times were extracted where the potential exceeded 4 standard deviations of the signal calculated across the entire block. All firing rate data were binned at 100 ms. The LFP amplitudes were calculated by subtracting any slow drift in the potential (piece-wise linear fit to the potential at the beginning of each trial) and averaging the negative of the signal during the entire stimulus presentation. For LFP power, the signal was low-pass filtered at 300 Hz.

Spectrograms were computed for each trial using a 250 ms Hamming window and frequencies from 7–200 Hz. Values reported represent the average over all frequencies and the entire stimulus presentation time.

### **6.2.8. Statistical Procedures**

We tested the data for normality with the Lilliefors test (Lilliefors 1967). The electrophysiological measures exhibited normal distributions, but the fMRI BOLD data exhibited non-normal distributions ( $P < 0.005$ ). Therefore, we conducted non-parametric tests throughout (Wilcoxon signed rank and rank-sum two-tail tests).

### **6.2.9. Histology**

Mice ( $n = 4$ ; 2 from the MRI experiment and 2 from the electrophysiology experiment) were transcardially perfused with 100 mM phosphate buffer (PB) followed by 4% formaldehyde in PB, and brains were post-fixed for 18 h at 4° C. Free-floating sections (50  $\mu\text{m}$ ) were cut using a freezing-microtome (American Optical Model 820), mounted on glass slides with Vectashield (Vector Laboratories), and coverslipped. Spread and labeling efficiency were estimated by examination of 50  $\mu\text{m}$  coronal sections near the somatosensory barrel cortex for the presence of YFP using a Zeiss LSM 5 Pascal (Carl Zeiss Light Microscopy) in wide-field fluorescence and laser scanning confocal modes.

### 6.3. Results

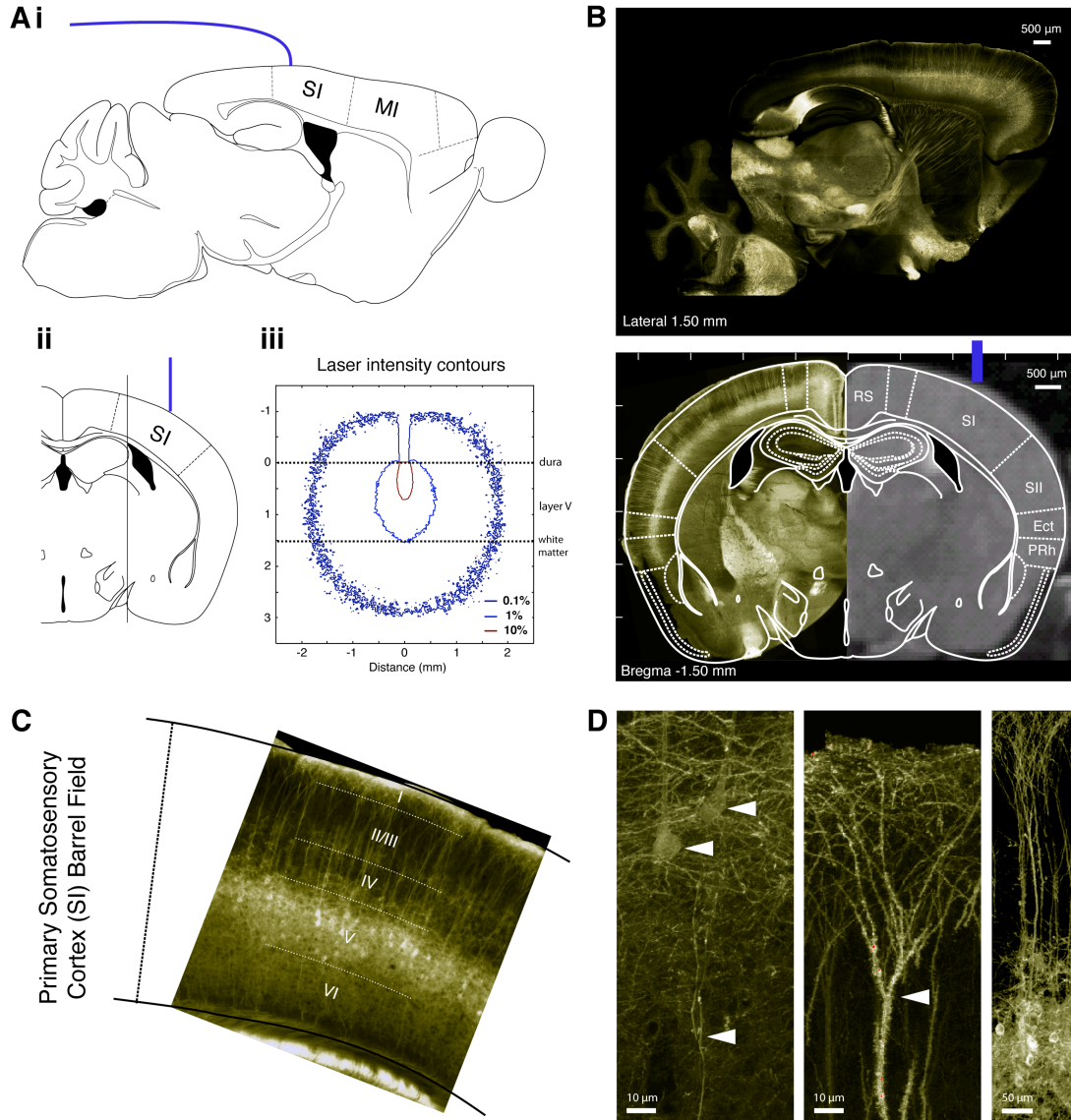


**Figure 6.1. Neural activation of layer V ChR2-expressing neurons by light stimulation evokes a reliable fMRI response.** **A**, Opto-fMRI experimental design. Atlas (Paxinos and Franklin, 2001) sagittal (i) and coronal (ii) sections depict the placement of the fiber optic (blue line) over primary somatosensory cortex (SI) barrel field. Monte Carlo simulation of laser intensity contours are plotted (iii) demonstrating that light intensity at 750 μm was 10 %, power sufficient to induce action potentials in layer V pyramidal neurons in vitro. **B**, Wide-field fluorescence depicts ChR2 expression of primarily layer V pyramidal

neurons in a transgenic Thy1-ChR2-YFP mouse. Sagittal slice depicts expression throughout the neocortex and an atlas section is superimposed on representative histological and anatomical MRI coronal sections, depicting the site of stimulation for a representative animal. **C**, A characteristic consistent expression is shown demonstrating fluorescence in layer V pyramidal neurons. **D**, Maximum intensity projection of confocal laser scanning microscopy demonstrates ChR2 expression. Denoted by white triangles are apical dendrites approaching the surface, the cell bodies, and axons.

Primary somatosensory cortex barrel field (SI; Bregma AP -1.5 mm, ML 2.5 mm in Paxinos and Franklin 2001) was chosen as the optical stimulation site. **Figure 6.1 A** and **B** shows typical fiber-optic placement. The light irradiance was at least  $300 \text{ mW mm}^{-2}$ , such that at layer V about 10% of the light was present (**Fig. 6.1 Aiii**), a power level that fully activates ChR2 (Boyden et al. 2005b; Wang et al. 2007). To confirm expression of ChR2-YFP fusion protein under the control of the Thy1 promoter in the stimulated site, we carried out histological experiments in four mice. Robust ChR2-YFP expression was observed in layer V pyramidal neurons (**Fig. 6.1 B-D**) with extensive expression in apical dendrites and cell bodies. The pattern was consistent with previously reported expression in Thy1 promoter-driven lines (Arenkiel et al. 2007; Ayling et al. 2009b; Feng et al. 2000).

We first tested whether a BOLD response could be observed in response to optical stimulation in neurons expressing ChR2 and the extent to which optical drive spatially corresponded to sensory driven responses (**Fig. 6.2**). In each animal participating in the fMRI experiment, between two and eight localizer runs were intermixed with target runs. In the localizer runs, either light pulses (8

animals) or whisker deflections (4 animals) were applied for 15 s followed by 15 s of no stimulation, and repeated 16 times in each run. BOLD responses were observed in SIBF for the optical (**Fig. 6.2 A**) and sensory (**Fig. 6.2 B**) conditions. Optically driven BOLD responses extended over a volume of  $0.65 \pm 0.29 \text{ mm}^3$  (mean  $\pm$  std; 8 animals), consistent with the emitted light irradiance. Similarly, sensory-driven BOLD responses extended over a volume of  $0.60 \pm 0.11 \text{ mm}^3$  (4 animals). To evaluate the consistency of evoked hemodynamic responses across animals, we calculated the average percent signal modulation in each animal for multiple runs. Stable estimates were observed across all animals in both stimulation strategies (**Fig. 6.2 C**).

Dale and Buckner (1997b) observed that the BOLD response summated in an approximately linear fashion to pairs of brief visual stimuli (1 s), spaced by as little as 2 s. We sought to test the assertion that subtraction of (n) 1 s trains from (n + 1) 1 s trains of activity would yield a response equivalent to a single 1 s train. Employing cell-attached juxtacellular recording from single units (SUA; 5 animals) as well as MUA and LFP recording with 16-channel laminar electrodes (1 animal) we observed an equivalent level of activity by 1 s periods of stimulation in both the single and double trial conditions (**Fig. 6.3**).

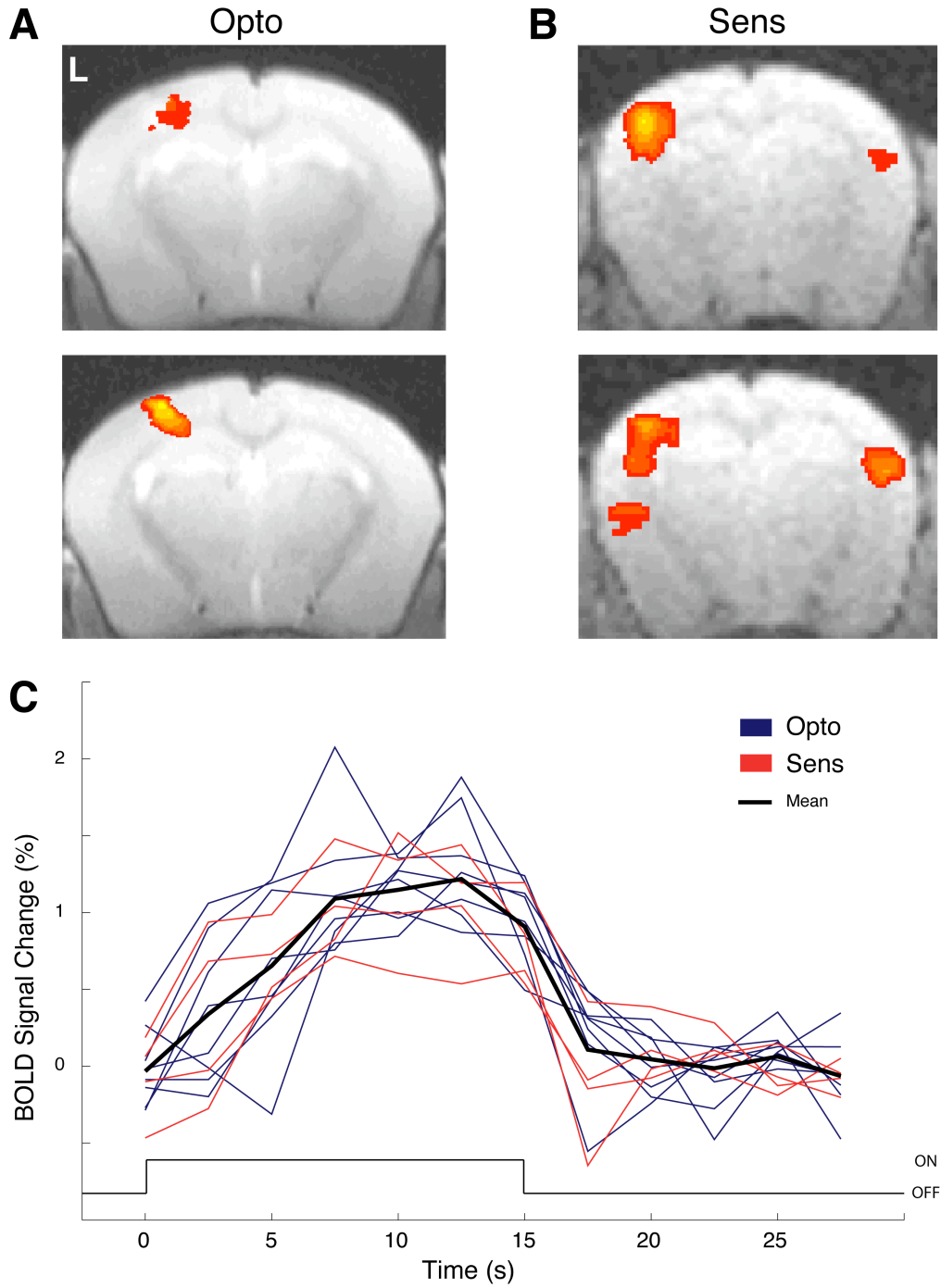


**Figure 6.2. Neural activation of layer V ChR2-expressing neurons by light stimulation evokes a reliable fMRI response that is equivalent to somatosensory response evoked by whisker deflection.** “Localizer” runs consisted of 16 repetitions of 15 s light-pulses or deflections of the mystacial whiskers followed by 15 s of no stimulation. **A**, A statistical parametric map of a positive BOLD response to light stimulation ( $P < 0.05$  corrected for multiple comparisons) is overlaid on the average fMRI BOLD image of the sequential

cross-sections demonstrating the response for the optical drive in a typical animal (“Opto”). **B**, A similar BOLD response was observed to whisker deflections (“Sens”). **C**, Activation extracted for activated voxels is plotted for both optically-driven (blue; n = 8) and sensory-driven (red; n = 4) responses in primary somatosensory cortex.

We next extracted the BOLD time series from voxels identified in localizer runs for all animals. The single and double trial conditions demonstrated an approximately linear increase, where a subtraction of the single trial from the double trial yielded a time series matching the single trial condition (**Fig. 6.4 A**; 6 animals). To generalize this result, we tested whether this pattern held when multiple 1 s trains were compared. We compared in a separate experiment (2 animals) optical drive of five (quintuple) to six (sextuple) 1 s trains. The computed the subtraction of these conditions yielded a response that appeared to be equivalent to a single 1 s train (**Fig. 6.4 B**). To provide a bridge to BOLD responses observed in human fMRI, we compared the optical somatosensory evoked responses to multi-synaptic sensory evoked responses such as those generated by vibrissal deflections. Both the single/double (2 animals; **Fig. 6.4 C**) and quintuple/sextuple (2 animals; **Fig. 6.4 D**) exhibited what appeared to be linear increase.

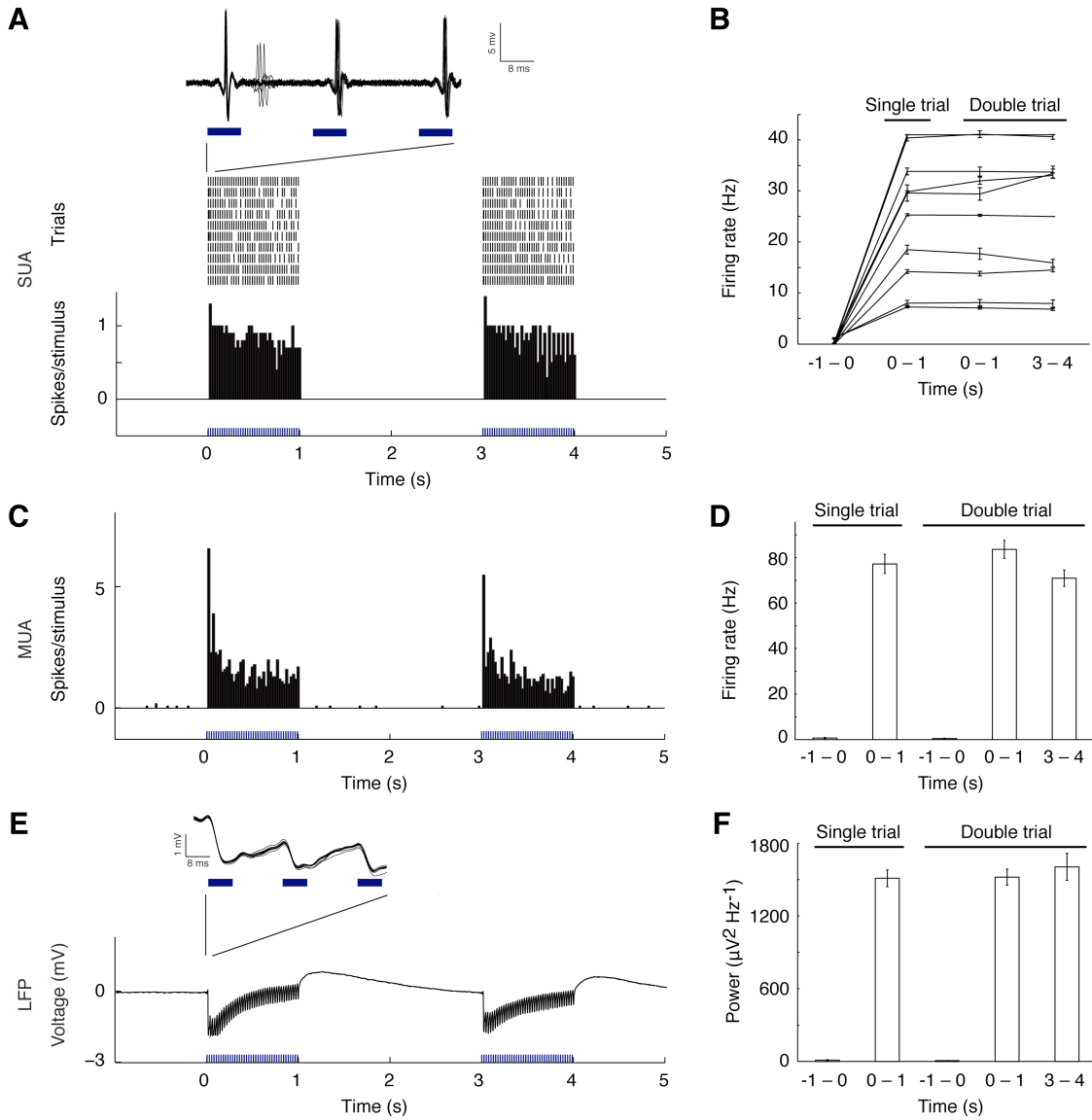


**Figure 6.3. Precisely evoked spike and local field potential activity for 1 s trains of optical stimulation of primary somatosensory cortex.** **A**, A representative neuron's activity (single-unit activity [SUA]) recorded juxtacellularly is depicted. Raster plot (top) and Peri-stimulus time histogram (PSTH; bottom) show equivalent spike responses for the two trains of 1 s stimulation. Overlaid voltage traces during the first three light pulses (inset) show highly reliable spike times and shape. **B**, SUA shown for individual neurons, demonstrates that although firing rate was variable between neurons, each neuron showed equivalent firing rate for 1 s train of light pulses in all conditions. **C**, PSTH of multi-unit activity (MUA) recorded using a laminar electrode is depicted. Responses are averaged from two contacts (depths of 700  $\mu\text{m}$  and 800  $\mu\text{m}$ ). **D**, Similar to SUA, MUA responses were above baseline and equivalent when comparing the 1 s optical stimulation intervals. **E**, Local field

potential (LFP) modulation was observed for each light stimulation train. A representative voltage trace is shown for one trial. The consistency of the response across individual trials is shown by the high overlap of individual traces (inset). **F**, Similar to SUA and MUA, power modulation was equivalent across the 1 s intervals.

We quantified these results using a variety of metrics. First, we verified that the integrated BOLD response of the (n +1) trials produced a significantly greater response relative to (n) trials in the optical and sensory driven responses (Wilcoxon signed rank paired two-tailed test; Opto: single/double  $P = 7.04e-6$  and quintuple/sextuple:  $P = .017$ ; Sens: single/double  $P = 0.006$  and quintuple/sextuple:  $P = .015$ ). Second, we computed the ratio between the responses of the (n +1) and (n) trials conditions. For the single/double conditions the BOLD response signal was integrated over the 2.5–12.5 s period for the optical and sensory driven responses; for SUA and MUA, the total number of spikes was counted; and for LFPs, the total power was calculated. The electrophysiological measures yielded a double to single response ratio close to 2: SUA,  $1.99 \pm 0.02$  [mean  $\pm$  SEM]; MUA;  $2.05 \pm 0.07$ ; LFP  $2.05 \pm 0.04$ , and a similar ratio held for the BOLD responses (Opto:  $1.97 \pm 0.25$ ; Sens:  $1.70 \pm 0.18$ ). Similarly, for the quintuple/sextuple conditions BOLD integrated responses were computed over the 2.5–22.5 s period for the optical and sensory driven responses, yielding a response ratio close to 1.2 (Opto:  $1.25 \pm .08$ ; Sens:  $1.25 \pm .08$ ). Thus, consistent with spiking activity in individual neurons, short trains of activity, when separated in time, linearly summated in the BOLD response.

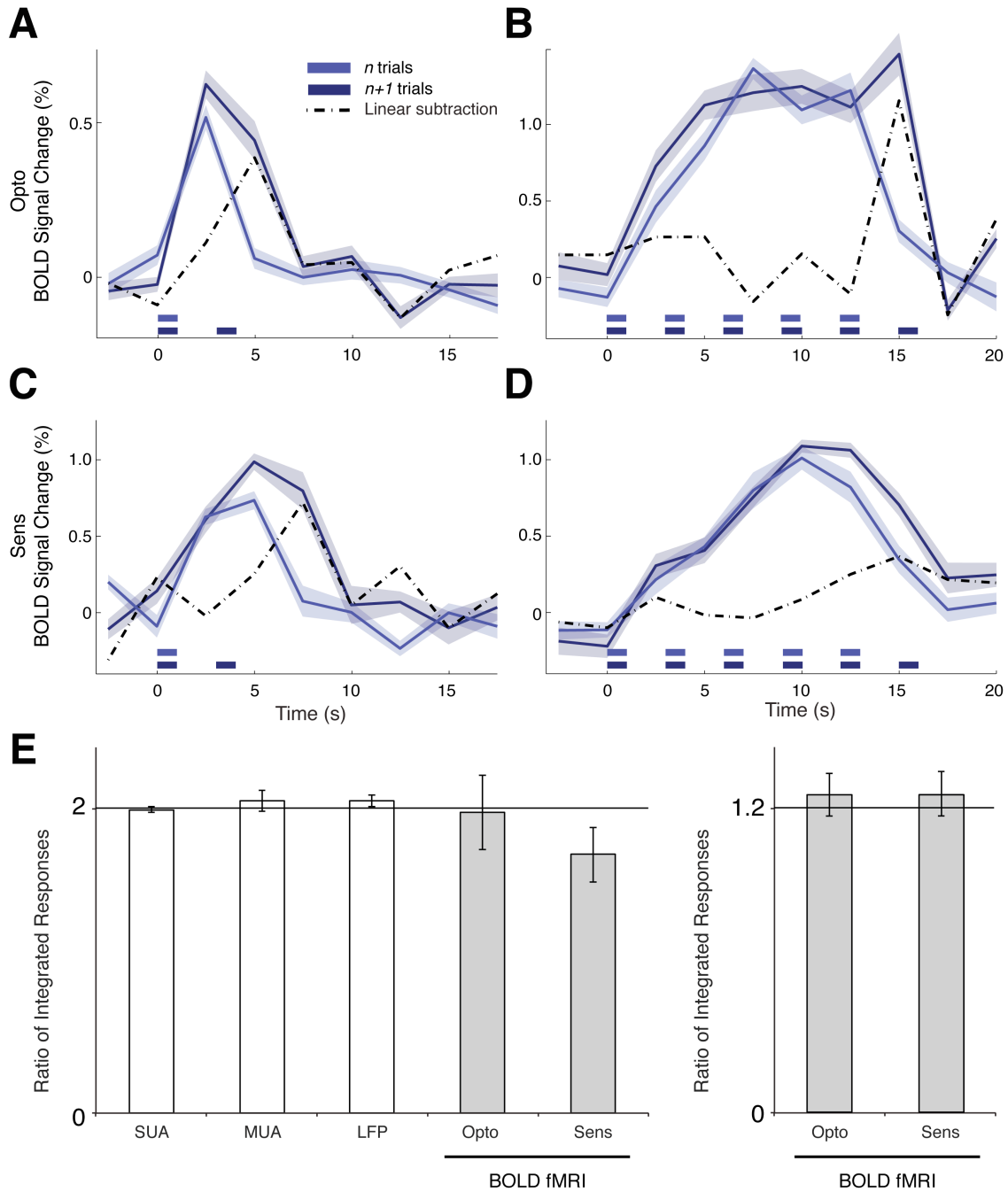


**Figure 6.4. The BOLD response shows linear temporal summation for closely spaced short trains of stimulation.** For each animal, time series were extracted from a region of interest (ROI) identified in independent localizer runs. The linear response can be qualitatively observed by subtracting the  $n$  from the  $n+1$  conditions (dashed line). **A**, Optical stimulation evoked equivalent responses across multiple independent of 1 s trains. Average time series ( $n = 6$

animals) of the BOLD fMRI response to one 1 s interval (single) and two trains of 1 s intervals (double) with an inter-stimulus interval of 2 s. The subtraction of the two conditions (dashed line) provides a qualitative depiction of the response to the estimated 1 s train. **B**, Five 1 s (quintuple) and six 1 s trains (sextuple) show an equivalent temporal linearity response (2 animals) to that observed in **A**. **C,D**, Sensory stimulation yielded an equivalent responses in the single / double (2 animals) experiment and quintuple / sextuple (2 animals) experiments. **E**, The temporal linearity response was quantified by dividing the response for the n+1 trials condition by the n trials condition. Opto: Optical drive; Sens: Sensory drive; SUA: Single Unit Activity; MUA: Multi Unit activity; LFP: Local Field Potential.

## 6.4. Discussion

In this chapter optical stimulation was used to control the precise timing of pyramidal cell activity. Our findings demonstrate that when regular spiking pyramidal cells in layer V of the sensory neocortex are driven by stimulation of light-activated cation channels, a hemodynamic response is evoked reliably. We recorded single-unit, multi-unit and LFP activity to test whether the BOLD response followed the linear transform model. We observed a linear summation of the BOLD response for temporally spaced short trains of optical stimulation that were proportional to the cumulative neural activity recorded as SUA, MUA and LFP signals.

A core assumption of brain imaging with fMRI using the BOLD-contrast mechanism is that local changes of neural activity elicit a hemodynamic response and that the hemodynamic response is approximately linearly related to the

underlying neural activity (Boynton et al. 1996; Dale and Buckner 1997b; Heeger and Ress 2002; Logothetis et al. 2001; Miezin et al. 2000; Rees et al. 2000). Results in this chapter suggest that – to first approximation – this assertion is supported. Optically driven BOLD responses demonstrated temporal linear summation following closely temporally spaced trains of stimulation. Further, the data presented in this chapter indicate that similar analysis assumptions can be applied to opto-fMRI responses generated by direct optical activation of pyramidal neurons. The findings in this chapter suggest that a rodent model may be a valid approach to explore what inferences can be made about underlying neural activity from the indirect BOLD response.

The use of opto-fMRI to probe the BOLD response suggest a general approach to study systematically the relation between local changes in neural activity and the BOLD response recorded by fMRI. The opto-fMRI approach employed in this chapter is similar to the one used in **Chapter 5**, Desai et al. (2010) and Lee et al. (2010), which used opto-fMRI to study network connectivity, and activated CaMKII $\alpha$ -expressing excitatory neurons that were virally transduced. In this chapter (and **Chapter 4**) Thy1 transgenic mouse model expressing Chr2 is used, providing an effective system for studying the relation between neural activity and fMRI. By focusing on understanding the local response, we have probed the neural and BOLD responses under conditions typically employed in human imaging, the summation of short duration, closely spaced event-related signals.



## **Chapter 7. Summary and Future Direction**

### **7.1. Summary**

The goal of this thesis was to develop methods that extend the unique aspects of small-animal high-field functional magnetic resonance imaging (fMRI) and to deploy them to better understand how neurons within a specific functional network interact. In **Chapter 3**, we have seen how we developed a technique to image squirrel monkeys in a high-field 9.4 T scanner. We use this technique to map activation associated with stimulation of the distal fingerpad of the 3<sup>rd</sup> digit in squirrel monkeys. The somatosensory maps obtained for the fingerpad stimulation were largely in agreement with the known anatomical and functional maps (Chen et al. 2005; Flaherty and Graybiel 1991; 1995; Jain et al. 2001; Nelson et al. 2006; Sur et al. 1982). Next in this chapter, the interaction between somatosensory cortex and basal ganglia within the somatosensory network that is activated by fingerpad stimulation is examined. In this study the isoflurane depth is modulated and the functional connectivity between the somatosensory cortex and basal ganglia is probed. We observe a dose dependent effect of isoflurane on the fMRI responses in somatosensory cortex and in the putamen for the tactile stimulation, but a near loss in the response in caudate nucleus. What we also

observe is that while the impact of isoflurane on sensory-driven activation of SI and putamen was modest (responses in > 60% of the sessions at 1.4%), the connectivity between these regions is significantly decreased for increased isoflurane levels.

An approach of combining high-resolution blood oxygenation level-dependent (BOLD) fMRI and optogenetics manipulation (opto-fMRI) to measure the distributed BOLD response evoked by optical activation of a defined cell class expressing the light-gated ion channel channelrhodopsin-2 (ChR2) is described in **Chapter 4**. Key technical approaches, including the critical hardware design choices, surgical strategies, MRI pulse sequences, and data analysis methods required to combine high-field small-animal fMRI and optical control of defined neural networks in the mouse brain, are described in this chapter. Repeatability and reliability of the opto-fMRI approach is demonstrated in mice transgenically expressing ChR2, with high spatial resolution, sufficient to resolve sub-columnar activity.

**Chapter 5** extends the opto-fMRI approach and is implemented on awake mice that were virally transduced with ChR2 in CaMKII $\alpha$ -expressing excitatory neurons. By using opto-fMRI in awake mouse and optically targeting cortical pyramidal cells of the mouse SI barrel cortex, which has well-characterized targets throughout the brain (Aronoff et al. 2010; Carvell and Simons 1986; 1987; Chakrabarti and Alloway 2006; Diamond et al. 2008; Ferezou et al. 2007; Megevand et al. 2008; White and DeAmicis 1977), we demonstrate that

distributed regions of a network in the brain could be mapped by light stimulation and measured using an unbiased, automated fMRI analysis. Functional connectivity between the regions of a network was also measured and an anesthesia effect on the functional connectivity (much like **Chapter 3**) was also observed using this technique. These collective results from **Chapter 4** and **Chapter 5** suggest that opto-fMRI provides an approach to map circuits in the awake mouse and thus complements fMRI approaches used *in vivo* in humans.

In **Chapter 6** optical stimulation was used to control the precise timing of pyramidal cell activity in mice that transgenically express ChR2 in layer V pyramidal cells. Our findings demonstrate that when regular spiking pyramidal cells in layer V of the sensory neocortex are driven by stimulation of light-activated cation channels, a hemodynamic response is evoked reliably. We recorded single-unit, multi-unit and LFP activity to test whether the BOLD response followed the linear transform model. We observed a linear summation of the BOLD response for temporally spaced short trains of optical stimulation that were proportional to the cumulative neural activity recorded as SUA, MUA and LFP signals. In this we demonstrate that using opto-fMRI we can focus on understanding the fMRI BOLD response, under conditions typically employed in human imaging, and helps interpret the sensory driven BOLD responses and its relationship to the underlying neural activity.

## **7.2. Future directions**

There are number of possible studies that may stem from the work presented in this thesis. The opto-fMRI techniques presented here represent an operational platform for probing the causal role of a set of neurons in a specific region on the other regions throughout the brain. This initial demonstration of the feasibility of obtaining fMRI images during brain stimulation by light opens the possibility of using allied optogenetic methods including optical neural silencing reagents (Chow et al. 2010; Zhao et al. 2008) and other advances in the field of optogenetics, including multisite neuromodulation, targeting of different interneurons within circuits (Cardin et al. 2009), and further improvements of fMRI that will further optimize opto-fMRI.

The initial demonstration of awake opto-fMRI also opens up several lines of new fMRI studies related to sensory perception in behaving animals. Opto-fMRI studies in behaving animals would provide an opportunity to dissect the influence of a specific set of neurons on a behavior and simultaneously would allow the study of neural circuits that influence that behavior or any behavioral changes. These studies would have great impact, as they would provide the unique ability to target a single cell types and also measure whole brain activity related to a behavioral goal and/or outcome (e.g., failure or success at perceiving a stimulus).

Opto-fMRI can also be used to study characteristics of the BOLD signal. In this thesis, one such study was presented, where we systematically examined linear temporal summation characteristics of the BOLD signal that were previously reported in sensory driven fMRI studies. Likewise, opto-fMRI presents an opportunity to further examine the BOLD signal by systematically probing different types of neurons and delineating their relative contribution to the induced BOLD signal. The BOLD signal measures brain activity indirectly, using signals generated by the hemodynamic changes in response to the neural activity (Boynton et al. 1996; Dale and Buckner 1997a; Heeger et al. 2000; Logothetis et al. 2001; Mukamel et al. 2005). While the hemodynamic changes are relatively well understood, little is known about the mechanism driving them. Opto-fMRI would be an ideal tool for determining how direct activation of a given cell type leads to functional hyperemia, as it allows probing of different cell types in the brain (i.e. excitatory neurons, interneurons, and astrocytes; (Boyden et al. 2005a; Cardin et al. 2009; Gradinaru et al. 2009; Han and Boyden 2007b; Zhang et al. 2006)).

As the component technologies of opto-fMRI continue to improve, so will the power of opto-fMRI to enhance the ability to understand distributed network functions.



## Chapter 8. References

1. **Ahrens ET, and Dubowitz DJ (2001)** Peripheral somatosensory fMRI in mouse at 11.7 T. *NMR in Biomedicine* 14: 318-324.
2. **Airan RD, Hu ES, Vijaykumar R, Roy M, Meltzer LA, and Deisseroth K (2007)** Integration of light-controlled neuronal firing and fast circuit imaging. *Curr Opin Neurobiol* 17: 587-592.
3. **Akbarian S, Grusser OJ, and Guldin WO (1992)** Thalamic connections of the vestibular cortical fields in the squirrel monkey (*Saimiri sciureus*). *J Comp Neurol* 326: 423-441.
4. **Alkire MT, Haier RJ, and Fallon JH (2000)** Toward a unified theory of narcosis: brain imaging evidence for a thalamocortical switch as the neurophysiologic basis of anesthetic-induced unconsciousness. *Conscious Cogn* 9: 370-386.
5. **Alloway KD, Lou L, Nwabueze-Ogbo F, and Chakrabarti S (2006)** Topography of cortical projections to the dorsolateral neostriatum in rats: multiple overlapping sensorimotor pathways. *J Comp Neurol* 499: 33-48.
6. **Alloway KD, Matic JJ, Hoffer ZS, and Hoover JE (2000)** Overlapping corticostriatal projections from the rodent vibrissal representations in primary and secondary somatosensory cortex. *J Comp Neurol* 428: 51-67.
7. **Andermann ML, Kerlin AM, and Reid RC (2010)** Chronic cellular imaging of mouse visual cortex during operant behavior and passive viewing. *Front Cell Neurosci* 4: 3.
8. **Andermann ML, and Moore CI (2006)** A somatotopic map of vibrissa motion direction within a barrel column. *Nat Neurosci* 9: 543-551.
9. **Andermann ML, and Moore CI (2008)** Mechanical resonance enhances the sensitivity of the vibrissa sensory system to near-threshold stimuli. *Brain Res* 1235: 74-81.

10. **Arenkiel BR, Peca J, Davison IG, Feliciano C, Deisseroth K, Augustine GJ, Ehlers MD, and Feng G (2007)** In vivo light-induced activation of neural circuitry in transgenic mice expressing channelrhodopsin-2. *Neuron* 54: 205-218.
11. **Aronoff R, Matyas F, Mateo C, Ciron C, Schneider B, and Petersen CC (2010)** Long-range connectivity of mouse primary somatosensory barrel cortex. *Eur J Neurosci* 31: 2221-2233.
12. **Austin VC, Blamire AM, Allers KA, Sharp T, Styles P, Matthews PM, and Sibson NR (2005)** Confounding effects of anesthesia on functional activation in rodent brain: a study of halothane and alpha-chloralose anesthesia. *Neuroimage* 24: 92-100.
13. **Ayling O, Harrison T, Boyd J, Goroshkov A, and Murphy T (2009a)** Automated light-based mapping of motor cortex by photoactivation of channelrhodopsin-2 transgenic mice. *Nature Methods* 6: 219--224.
15. **Bandettini PA, Wong EC, Jesmanowicz A, Hinks RS, and Hyde JS (1994)** Spin-echo and gradient-echo EPI of human brain activation using BOLD contrast: a comparative study at 1.5 T. *NMR Biomed* 7: 12-20.
16. **Berndt A, Yizhar O, Gunaydin L, Hegemann P, and Deisseroth K (2009)** Bi-stable neural state switches. *Nat Neurosci* 12: 229-234.
17. **Bernstein JG, Han X, Henninger MA, Ko EY, Qian X, Franzesi GT, McConnell JP, Stern P, Desimone R, and Boyden ES (2008)** Prosthetic systems for therapeutic optical activation and silencing of genetically-targeted neurons. *Proc Soc Photo Opt Instrum Eng* 6854.
18. **Biswal B, Yetkin FZ, Haughton VM, and Hyde JS (1995)** Functional connectivity in the motor cortex of resting human brain using echo-planar MRI. *Magn Reson Med* 34: 537-541.
19. **Boyden E, Zhang F, Bamberg E, Nagel G, and Deisseroth K (2005a)** Millisecond-timescale, genetically targeted optical control of neural activity. *Nature Neuroscience* 8: 1263--1268.
20. **Boyden ES, Katoh A, Pyle JL, Chatila TA, Tsien RW, and Raymond JL (2006)** Selective engagement of plasticity mechanisms for motor memory storage. *Neuron* 51: 823-834.

21. **Boyden ES, and Raymond JL (2003)** Active reversal of motor memories reveals rules governing memory encoding. *Neuron* 39: 1031-1042.
23. **Boynton GM, Engel SA, Glover GH, and Heeger DJ (1996)** Linear systems analysis of functional magnetic resonance imaging in human V1. *J Neurosci* 16: 4207-4221.
24. **Brady AG (2000)** Research techniques for the squirrel monkey (*Saimiri* sp.). *ILAR J* 41: 10-18.
25. **Brevard ME, Duong TQ, King JA, and Ferris CF (2003)** Changes in MRI signal intensity during hypercapnic challenge under conscious and anesthetized conditions. *Magn Reson Imaging* 21: 995-1001.
26. **Brown P, and Marsden CD (1998)** What do the basal ganglia do? *Lancet* 351: 1801-1804.
27. **Canals S, Beyerlein M, Murayama Y, and Logothetis NK (2008)** Electric stimulation fMRI of the perforant pathway to the rat hippocampus. *Magn Reson Imaging* 26: 978-986.
28. **Cardin J, Carlen M, Meletis K, Knoblich U, Zhang F, Deisseroth K, Tsai L-H, and Moore C (2009)** Driving fast-spiking cells induces gamma rhythm and controls sensory responses. *Nature* 459: 663--667.
29. **Cardin JA, Carlen M, Meletis K, Knoblich U, Zhang F, Deisseroth K, Tsai LH, and Moore CI (2010)** Targeted optogenetic stimulation and recording of neurons in vivo using cell-type-specific expression of Channelrhodopsin-2. *Nat Protoc* 5: 247-254.
30. **Carter ME, and de Lecea L (2011)** Optogenetic investigation of neural circuits in vivo. *Trends Mol Med* 17: 197-206.
31. **Carvell GE, and Simons DJ (1986)** Somatotopic organization of the second somatosensory area (SII) in the cerebral cortex of the mouse. *Somatosens Res* 3: 213-237.
32. **Carvell GE, and Simons DJ (1987)** Thalamic and corticocortical connections of the second somatic sensory area of the mouse. *J Comp Neurol* 265: 409-427.

- 33. Chakrabarti S, and Alloway KD (2006)** Differential origin of projections from SI barrel cortex to the whisker representations in SII and MI. *J Comp Neurol* 498: 624-636.
- 34. Chen LM, Friedman RM, and Roe AW (2005)** Optical imaging of SI topography in anesthetized and awake squirrel monkeys. *J Neurosci* 25: 7648-7659.
- 35. Chen LM, Turner GH, Friedman RM, Zhang N, Gore JC, Roe AW, and Avison MJ (2007)** High-resolution maps of real and illusory tactile activation in primary somatosensory cortex in individual monkeys with functional magnetic resonance imaging and optical imaging. *J Neurosci* 27: 9181-9191.
- 36. Cheung SW, Bedenbaugh PH, Nagarajan SS, and Schreiner CE (2001)** Functional organization of squirrel monkey primary auditory cortex: responses to pure tones. *J Neurophysiol* 85: 1732-1749.
- 37. Chow BY, Han X, Dobry AS, Qian X, Chuong AS, Li M, Henninger MA, Belfort GM, Lin Y, Monahan PE, and Boyden ES (2010)** High-performance genetically targetable optical neural silencing by light-driven proton pumps. *Nature* 463: 98-102.
- 38. Chudler EH, Sugiyama K, and Dong WK (1995)** Multisensory convergence and integration in the neostriatum and globus pallidus of the rat. *Brain Res* 674: 33-45.
- 39. Cohen ER, Ugurbil K, and Kim SG (2002)** Effect of basal conditions on the magnitude and dynamics of the blood oxygenation level-dependent fMRI response. *J Cereb Blood Flow Metab* 22: 1042-1053.
- 40. Coq JO, Qi H, Collins CE, and Kaas JH (2004)** Anatomical and functional organization of somatosensory areas of the lateral fissure of the New World titi monkey (*Callicebus moloch*). *J Comp Neurol* 476: 363-387.
- 41. Corfield DR, Murphy K, Josephs O, Adams L, and Turner R (2001)** Does Hypercapnia-Induced Cerebral Vasodilation Modulate the Hemodynamic Response to Neural Activation? *NeuroImage*
- 42. Cox R (1996)** AFNI: software for analysis and visualization of functional magnetic resonance neuroimages. *Computers and biomedical research, an international journal* 29: 162--173.

- 43. Crosby G, Crane AM, Jehle J, and Sokoloff L (1983)** The local metabolic effects of somatosensory stimulation in the central nervous system of rats given pentobarbital or nitrous oxide. *Anesthesiology* 58: 38-43.
- 44. Dale AM, and Buckner RL (1997a)** Selective averaging of rapidly presented individual trials using fMRI. *Hum Brain Mapp* 5: 329-340.
- 46. de Kock CP, and Sakmann B (2009)** Spiking in primary somatosensory cortex during natural whisking in awake head-restrained rats is cell-type specific. *Proc Natl Acad Sci U S A* 106: 16446-16450.
- 47. De Poorter J (1995)** Noninvasive MRI thermometry with the proton resonance frequency method: study of susceptibility effects. *Magn Reson Med* 34: 359-367.
- 48. Deisseroth K, Feng G, Majewska A, Miesenböck G, Ting A, and Schnitzer M (2006)** Next-generation optical technologies for illuminating genetically targeted brain circuits. *J Neuroscience* 26: 10380--10386.
- 49. Desai M, Kahn I, Knoblich U, Bernstein J, Atallah H, Yang A, Kopell N, Buckner RL, Graybiel AM, Moore CI, and Boyden ES (2010)** Mapping Brain Networks in Awake Mice Using Combined Optical Neural Control and fMRI. *J Neurophysiol*
- 50. Detari L, Rasmusson DD, and Semba K (1999)** The role of basal forebrain neurons in tonic and phasic activation of the cerebral cortex. *Prog Neurobiol* 58: 249-277.
- 51. Detsch O, Kochs E, Siemers M, Bromm B, and Vahle-Hinz C (2002)** Differential effects of isoflurane on excitatory and inhibitory synaptic inputs to thalamic neurones in vivo. *Br J Anaesth* 89: 294-300.
- 52. Diamond M, Heimendahl M, Knutsen P, Kleinfeld D, and Ahissar E (2008)** 'Where' and 'what' in the whisker sensorimotor system. *Nat Rev Neurosci* 9: 601--612.
- 53. Disbrow EA, Slutsky DA, Roberts TP, and Krubitzer LA (2000)** Functional MRI at 1.5 tesla: a comparison of the blood oxygenation level-dependent signal and electrophysiology. *Proc Natl Acad Sci U S A* 97: 9718-9723.

- 54. Duda RO, Hart PE, and Stork DG.** The Problem of Validity. In: *Pattern Classification*, edited by 2ndWiley-Interscience, 2000, p. 557-559.
- 55. Duong TQ, Yacoub E, Adriany G, Hu X, Ugurbil K, and Kim SG (2003)** Microvascular BOLD contribution at 4 and 7 T in the human brain: gradient-echo and spin-echo fMRI with suppression of blood effects. *Magn Reson Med* 49: 1019-1027.
- 56. Ehses P, Fidler F, Nordbeck P, Pracht ED, Warmuth M, Jakob PM, and Bauer WR (2008)** MRI thermometry: Fast mapping of RF-induced heating along conductive wires. *Magn Reson Med* 60: 457-461.
- 57. Ekstrom LB, Roelfsema PR, Arsenault JT, Bonmassar G, and Vanduffel W (2008)** Bottom-up dependent gating of frontal signals in early visual cortex. *Science* 321: 414-417.
- 58. Ekstrom LB, Roelfsema PR, Arsenault JT, Kolster H, and Vanduffel W (2009)** Modulation of the contrast response function by electrical microstimulation of the macaque frontal eye field. *J Neurosci* 29: 10683-10694.
- 59. Felisberti F, Antkowiak B, and Kirschfeld K (1997)** Effects of volatile anaesthetics on the membrane potential and ion channels of cultured neocortical astrocytes. *Brain Res* 766: 56-65.
- 60. Feng G, Mellor RH, Bernstein M, Keller-Peck C, Nguyen QT, Wallace M, Nerbonne JM, Lichtman JW, and Sanes JR (2000)** Imaging neuronal subsets in transgenic mice expressing multiple spectral variants of GFP. *Neuron* 28: 41-51.
- 61. Ferezou I, Haiss F, Gentet LJ, Aronoff R, Weber B, and Petersen CC (2007)** Spatiotemporal dynamics of cortical sensorimotor integration in behaving mice. *Neuron* 56: 907-923.
- 62. Ferris CF, Snowdon CT, King JA, Duong TQ, Ziegler TE, Ugurbil K, Ludwig R, Schultz-Darken NJ, Wu Z, Olson DP, Sullivan Jr JM, Tannenbaum PL, and Vaughan JT (2001)** Functional imaging of brain activity in conscious monkeys responding to sexually arousing cues. *Neuroreport* 12: 2231-2236.
- 63. Fiset P, Paus T, Daloze T, Plourde G, Meuret P, Bonhomme V, Hajj-Ali N, Backman SB, and Evans AC (1999)** Brain mechanisms of propofol-induced loss of consciousness in humans: a positron emission tomographic study. *J Neurosci* 19: 5506-5513.

- 64. Flaherty AW, and Graybiel AM (1991)** Corticostriatal transformations in the primate somatosensory system. Projections from physiologically mapped body-part representations. *J Neurophysiol* 66: 1249-1263.
- 65. Flaherty AW, and Graybiel AM (1994)** Input-output organization of the sensorimotor striatum in the squirrel monkey. *J Neurosci* 14: 599-610.
- 66. Flaherty AW, and Graybiel AM (1995)** Motor and somatosensory corticostriatal projection magnifications in the squirrel monkey. *J Neurophysiol* 74: 2638-2648.
- 67. Flaherty AW, and Graybiel AM (1993a)** Output architecture of the primate putamen. *J Neurosci* 13: 3222-3237.
- 68. Flaherty AW, and Graybiel AM (1993b)** Two input systems for body representations in the primate striatal matrix: experimental evidence in the squirrel monkey. *J Neurosci* 13: 1120-1137.
- 69. Forman S, Cohen J, Fitzgerald M, Eddy W, Mintun M, and Noll D (1995a)** Improved Assessment of Significant Activation in Functional Magnetic Resonance Imaging (fMRI): Use of a Cluster-Size Threshold. *Magnetic Resonance in Medicine* 33: 636-647.
- 70. Forman SD, Cohen JD, Fitzgerald M, Eddy WF, Mintun MA, and Noll DC (1995b)** Improved assessment of significant activation in functional magnetic resonance imaging (fMRI): use of a cluster-size threshold. *Magn Reson Med* 33: 636-647.
- 71. Fox MD, and Raichle ME (2007)** Spontaneous fluctuations in brain activity observed with functional magnetic resonance imaging. *Nature Reviews Neuroscience* 8: 700-711.
- 72. Fox MD, Snyder AZ, Vincent JL, Corbetta M, Van Essen DC, and Raichle ME (2005)** The human brain is intrinsically organized into dynamic, anticorrelated functional networks. *Proc Natl Acad Sci U S A* 102: 9673-9678.
- 73. Fox PT, Mintun MA, Reiman EM, and Raichle ME (1988)** Enhanced detection of focal brain responses using intersubject averaging and change-distribution analysis of subtracted PET images. *J Cereb Blood Flow Metab* 8: 642-653.

- 74. Fox PT, and Raichle ME (1986)** Focal physiological uncoupling of cerebral blood flow and oxidative metabolism during somatosensory stimulation in human subjects. *Proc Natl Acad Sci U S A* 83: 1140-1144.
- 75. Friston KJ (1994)** Functional and effective connectivity in neuroimaging: A synthesis. *Human Brain Mapping* 2: 56-78.
- 76. Friston KJ, Frith CD, Liddle PF, and Frackowiak RS (1993)** Functional connectivity: the principal-component analysis of large (PET) data sets. *Journal of cerebral blood flow and metabolism* 13: 5-14.
- 77. Fulton JF (1928)** Vasomotor and Reflex Sequelae of Unilateral Cervical and Lumbar Ramisectomy in a Case of Raynaud's Disease, with Observations on Tonus. *Ann Surg* 88: 827-841.
- 78. Gati JS, Menon RS, Ugurbil K, and Rutt BK (1997)** Experimental determination of the BOLD field strength dependence in vessels and tissue. *Magn Reson Med* 38: 296-302.
- 79. Giedd JN, Blumenthal J, Jeffries NO, Castellanos FX, Liu H, Zijdenbos A, Paus T, Evans AC, and Rapoport JL (1999)** Brain development during childhood and adolescence: a longitudinal MRI study. *Nat Neurosci* 2: 861-863.
- 80. Gradinaru V, Mogri M, Thompson KR, Henderson JM, and Deisseroth K (2009)** Optical deconstruction of parkinsonian neural circuitry. *Science* 324: 354-359.
- 81. Gradinaru V, Thompson KR, and Deisseroth K (2008)** eNpHR: a Natronomonas halorhodopsin enhanced for optogenetic applications. *Brain Cell Biol* 36: 129-139.
- 82. Gradinaru V, Thompson KR, Zhang F, Mogri M, Kay K, Schneider MB, and Deisseroth K (2007)** Targeting and readout strategies for fast optical neural control in vitro and in vivo. *J Neurosci* 27: 14231-14238.
- 83. Gradinaru V, Zhang F, Ramakrishnan C, Mattis J, Prakash R, Diester I, Goshen I, Thompson KR, and Deisseroth K (2010)** Molecular and cellular approaches for diversifying and extending optogenetics. *Cell* 141: 154-165.

- 84. Graziano MS, and Gross CG (1993)** A bimodal map of space: somatosensory receptive fields in the macaque putamen with corresponding visual receptive fields. *Exp Brain Res* 97: 96-109.
- 85. Guillery RW, and Sherman SM (2002)** Thalamic relay functions and their role in corticocortical communication: generalizations from the visual system. *Neuron* 33: 163-175.
- 86. Guldin WO, Akbarian S, and Grusser OJ (1992)** Cortico-cortical connections and cytoarchitectonics of the primate vestibular cortex: a study in squirrel monkeys (*Saimiri sciureus*). *J Comp Neurol* 326: 375-401.
- 87. Gunaydin LA, Yizhar O, Berndt A, Sohal VS, Deisseroth K, and Hegemann P (2010)** Ultrafast optogenetic control. *Nat Neurosci* 13: 387-392.
- 88. Hampson M, Tokoglu F, Sun Z, Schafer RJ, Skudlarski P, Gore JC, and Constable RT (2006)** Connectivity-behavior analysis reveals that functional connectivity between left BA39 and Broca's area varies with reading ability. *Neuroimage* 31: 513-519.
- 89. Han X, and Boyden E (2007a)** Multiple-Color Optical Activation, Silencing, and Desynchronization of Neural Activity, with Single-Spike Temporal Resolution. *PLoS ONE* 2: e299.
- 91. Han X, Qian X, Bernstein JG, Zhou HH, Franzesi GT, Stern P, Bronson RT, Graybiel AM, Desimone R, and Boyden ES (2009)** Millisecond-timescale optical control of neural dynamics in the nonhuman primate brain. *Neuron* 62: 191-198.
- 92. Haralick RM, and Shapiro LG.** *Computer and Robot Vision*. Addison-Wesley, 1992.
- 93. Heeger DJ, Huk AC, Geisler WS, and Albrecht DG (2000)** Spikes versus BOLD: what does neuroimaging tell us about neuronal activity? *Nat Neurosci* 3: 631-633.
- 94. Heeger DJ, and Ress D (2002)** What does fMRI tell us about neuronal activity? *Nat Rev Neurosci* 3: 142-151.
- 95. Hentschke H, Schwarz C, and Antkowiak B (2005)** Neocortex is the major target of sedative concentrations of volatile anaesthetics: strong depression of firing rates and increase of GABAA receptor-mediated inhibition. *Eur J Neurosci* 21: 93-102.

- 96. Hertz-Pannier L, Chiron C, Jambaque I, Renaux-Kieffer V, Van de Moortele PF, Delalande O, Fohlen M, Brunelle F, and Le Bihan D (2002)** Late plasticity for language in a child's non-dominant hemisphere: a pre- and post-surgery fMRI study. *Brain* 125: 361-372.
- 97. Hikosaka O (1991)** Basal ganglia--possible role in motor coordination and learning. *Curr Opin Neurobiol* 1: 638-643.
- 98. Hikosaka O, and Wurtz RH (1983)** Effects on eye movements of a GABA agonist and antagonist injected into monkey superior colliculus. *Brain Res* 272: 368-372.
- 99. Hikosaka O, and Wurtz RH (1989)** The basal ganglia. *Rev Oculomot Res* 3: 257-281.
- 100. Hoffer ZS, and Alloway KD (2001)** Organization of corticostriatal projections from the vibrissal representations in the primary motor and somatosensory cortical areas of rodents. *J Comp Neurol* 439: 87-103.
- 101. Hoover JE, and Strick PL (1993)** Multiple output channels in the basal ganglia. *Science* 259: 819-821.
- 102. Hoult DI, Chen CN, and Sank VJ (1986)** The field dependence of NMR imaging. II. Arguments concerning an optimal field strength. *Magn Reson Med* 3: 730-746.
- 103. Hutchison RM, Mirsattari SM, Jones CK, Gati JS, and Leung LS (2011)** Functional networks in the anesthetized rat brain revealed by independent component analysis of resting-state FMRI. *J Neurophysiol* 103: 3398-3406.
- 105. Hyder F, Behar KL, Martin MA, Blamire AM, and Shulman RG (1994)** Dynamic magnetic resonance imaging of the rat brain during forepaw stimulation. *Journal of cerebral blood flow and metabolism* 14: 649-655.
- 106. Jain N, Qi HX, Catania KC, and Kaas JH (2001)** Anatomic correlates of the face and oral cavity representations in the somatosensory cortical area 3b of monkeys. *J Comp Neurol* 429: 455-468.
- 107. Joksovic PM, and Todorovic SM (2010)** Isoflurane modulates neuronal excitability of the nucleus reticularis thalami in vitro. *Ann N Y Acad Sci* 1199: 36-42.

- 108. Kahn I, Andrews-Hanna JR, Vincent JL, Snyder AZ, and Buckner RL (2008)** Distinct cortical anatomy linked to subregions of the medial temporal lobe revealed by intrinsic functional connectivity. *J Neurophysiol* 100: 129-139.
- 109. Kahn T, Harth T, Kiwit JC, Schwarzmaier HJ, Wald C, and Modder U (1998)** In vivo MRI thermometry using a phase-sensitive sequence: preliminary experience during MRI-guided laser-induced interstitial thermotherapy of brain tumors. *J Magn Reson Imaging* 8: 160-164.
- 110. Khachaturian MH, Arsenault J, Ekstrom LB, Tuch DS, and Vanduffel W (2008)** Focal reversible deactivation of cerebral metabolism affects water diffusion. *Magn Reson Med* 60: 1178-1189.
- 111. Kim DS, Duong TQ, and Kim SG (2000)** High-resolution mapping of iso-orientation columns by fMRI. *Nature Neuroscience* 3: 164-169.
- 112. Kim YH, You SH, Kwon YH, Hallett M, Kim JH, and Jang SH (2006)** Longitudinal fMRI study for locomotor recovery in patients with stroke. *Neurology* 67: 330-333.
- 113. King JA, Garelick TS, Brevard ME, Chen W, Messenger TL, Duong TQ, and Ferris CF (2005)** Procedure for minimizing stress for fMRI studies in conscious rats. *J Neurosci Methods* 148: 154-160.
- 114. Kramer RH, Fortin DL, and Trauner D (2009)** New photochemical tools for controlling neuronal activity. *Curr Opin Neurobiol* 19: 544-552.
- 115. Kravitz AV, Freeze BS, Parker PR, Kay K, Thwin MT, Deisseroth K, and Kreitzer AC (2010)** Regulation of parkinsonian motor behaviours by optogenetic control of basal ganglia circuitry. *Nature*
- 116. Kwong KK, Belliveau JW, Chesler DA, Goldberg IE, Weisskoff RM, Poncelet BP, Kennedy DN, Hoppel BE, Cohen MS, Turner R, and et al. (1992)** Dynamic magnetic resonance imaging of human brain activity during primary sensory stimulation. *Proc Natl Acad Sci U S A* 89: 5675-5679.
- 117. Lahti KM, Ferris CF, Li F, Sotak CH, and King JA (1999)** Comparison of evoked cortical activity in conscious and propofol-anesthetized rats using functional MRI. *Magnetic resonance in medicine* 41: 412-416.
- 118. Lahti KM, Ferris CF, Li F, Sotak CH, and King JA (1998)** Imaging brain activity in conscious animals using functional MRI. *Journal of neuroscience methods* 82: 75-83.

- 119. Langmoen IA, Larsen M, and Berg-Johnsen J (1995)** Volatile anaesthetics: cellular mechanisms of action. *Eur J Anaesthesiol* 12: 51-58.
- 120. Lee JH, Durand R, Gradinaru V, Zhang F, Goshen I, Kim DS, Fenno LE, Ramakrishnan C, and Deisseroth K (2010)** Global and local fMRI signals driven by neurons defined optogenetically by type and wiring. *Nature* 465: 788-792.
- 121. Lee SP, Silva AC, Ugurbil K, and Kim SG (1999)** Diffusion-weighted spin-echo fMRI at 9.4 T: microvascular/tissue contribution to BOLD signal changes. *Magn Reson Med* 42: 919-928.
- 122. Leniger-Follert E, and Hossmann KA (1979)** Simultaneous measurements of microflow and evoked potentials in the somatomotor cortex of the cat brain during specific sensory activation. *Pflugers Arch* 380: 85-89.
- 123. Levesque M, Charara A, Gagnon S, Parent A, and Deschenes M (1996)** Corticostriatal projections from layer V cells in rat are collaterals of long-range corticofugal axons. *Brain Res* 709: 311-315.
- 124. Li X, Gutierrez DV, Hanson MG, Han J, Mark MD, Chiel H, Hegemann P, Landmesser LT, and Herlitze S (2005)** Fast noninvasive activation and inhibition of neural and network activity by vertebrate rhodopsin and green algae channelrhodopsin. *Proc Natl Acad Sci U S A* 102: 17816-17821.
- 125. Liachenko S, Tang P, Somogyi GT, and Xu Y (1999)** Concentration-dependent isoflurane effects on depolarization-evoked glutamate and GABA outflows from mouse brain slices. *Br J Pharmacol* 127: 131-138.
- 126. Lilliefors HW (1967)** On the Kolmogorov-Smirnov test for normality with mean and variance unknown. *J Amer Statistical Assoc* 62: 399-402.
- 127. Lindauer U, Villringer A, and Dirnagl U (1993)** Characterization of CBF response to somatosensory stimulation: model and influence of anesthetics. *Am J Physiol* 264: H1223-1228.
- 128. Lindquist M (2008)** The Statistical Analysis of fMRI Data. *Statistical Science* 23: 439-464.
- 129. Liu ZM, Schmidt KF, Sicard KM, and Duong TQ (2004)** Imaging oxygen consumption in forepaw somatosensory stimulation in rats under isoflurane anesthesia. *Magnetic resonance in medicine* 52: 277-285.

- 130. Livingstone MS (1996)** Oscillatory firing and interneuronal correlations in squirrel monkey striate cortex. *J Neurophysiol* 75: 2467-2485.
- 131. Logothetis NK (2003)** MR imaging in the non-human primate: studies of function and of dynamic connectivity. *Curr Opin Neurobiol* 13: 630-642.
- 132. Logothetis NK (2008)** What we can do and what we cannot do with fMRI. *Nature* 453: 869-878.
- 133. Logothetis NK, Augath M, Murayama Y, Rauch A, Sultan F, Goense J, Oeltermann A, and Merkle H (2010)** The effects of electrical microstimulation on cortical signal propagation. *Nat Neurosci*
- 134. Logothetis NK, Guggenberger H, Peled S, and Pauls J (1999)** Functional imaging of the monkey brain. *Nat Neurosci* 2: 555-562.
- 135. Logothetis NK, Pauls J, Augath M, Trinath T, and Oeltermann A (2001)** Neurophysiological investigation of the basis of the fMRI signal. *Nature* 412: 150-157.
- 136. Lukasik VM, and Gillies RJ (2003)** Animal anaesthesia for in vivo magnetic resonance. *NMR Biomed* 16: 459-467.
- 137. Magarinos-Ascone C, Garcia-Austt E, and Buno W (1994)** Polymodal sensory and motor convergence in substantia nigra neurons of the awake monkey. *Brain Res* 646: 299-302.
- 138. Masamoto K, Fukuda M, Vazquez A, and Kim S-G (2009a)** Dose-dependent effect of isoflurane on neurovascular coupling in rat cerebral cortex. *Eur J Neurosci* 30: 242-250.
- 140. Masamoto K, Kim T, Fukuda M, Wang P, and Kim SG (2007)** Relationship between neural, vascular, and BOLD signals in isoflurane-anesthetized rat somatosensory cortex. *Cereb Cortex* 17: 942-950.
- 141. Matta BF, Heath KJ, and Summors AC (1999)** Direct Cerebral Vasodilatory Effects of Sevoflurane and Isoflurane. *Anesthesiology*
- 142. McGeorge AJ, and Faull RL (1989)** The organization of the projection from the cerebral cortex to the striatum in the rat. *Neuroscience* 29: 503-537.

- 143. Megevand P, Quairiaux C, Lascano AM, Kiss JZ, and Michel CM (2008)** A mouse model for studying large-scale neuronal networks using EEG mapping techniques. *Neuroimage* 42: 591-602.
- 144. Merzenich MM, Nelson RJ, Kaas JH, Stryker MP, Jenkins WM, Zook JM, Cynader MS, and Schoppmann A (1987)** Variability in hand surface representations in areas 3b and 1 in adult owl and squirrel monkeys. *J Comp Neurol* 258: 281-296.
- 145. Meyer JS, Nomura F, Sakamoto K, and Kondo A (1969)** Effect of stimulation of the brain-stem reticular formation on cerebral blood flow and oxygen consumption. *Electroencephalogr Clin Neurophysiol* 26: 125-132.
- 146. Mhuirheartaigh RN, Rosenorn-Lanng D, Wise R, Jbabdi S, Rogers R, and Tracey I (2010)** Cortical and subcortical connectivity changes during decreasing levels of consciousness in humans: a functional magnetic resonance imaging study using propofol. *J Neurosci* 30: 9095-9102.
- 147. Middleton FA, and Strick PL (2000)** Basal ganglia output and cognition: evidence from anatomical, behavioral, and clinical studies. *Brain Cogn* 42: 183-200.
- 148. Middleton FA, and Strick PL (1998)** Cerebellar output: motor and cognitive channels. *Trends Cogn Sci* 2: 348-354.
- 149. Miezin FM, Maccotta L, Ollinger JM, Petersen SE, and Buckner RL (2000)** Characterizing the hemodynamic response: effects of presentation rate, sampling procedure, and the possibility of ordering brain activity based on relative timing. *Neuroimage* 11: 735-759.
- 150. Moeller S, Freiwald WA, and Tsao DY (2008)** Patches with links: a unified system for processing faces in the macaque temporal lobe. *Science* 320: 1355-1359.
- 151. Mohammadi B, Kollwe K, Samii A, Beckmann CF, Dengler R, and Munte TF (2011)** Changes in resting-state brain networks in writer's cramp. *Hum Brain Mapp*
- 152. Moon C-H, Fukuda M, Park S-H, and Kim S-G (2007)** Neural interpretation of blood oxygenation level-dependent fMRI maps at submillimeter columnar resolution. *The Journal of neuroscience* 27: 6892-6902.

- 153. Moruzzi G, and Magoun HW (1995)** Brain stem reticular formation and activation of the EEG. 1949. *J Neuropsychiatry Clin Neurosci* 7: 251-267.
- 154. Mowery T, Harrold J, and Alloway KD (2011)** Repeated whisker stimulation evokes invariant neuronal responses in the dorsolateral striatum of anesthetized rats: A potential correlate of sensorimotor habits. *J Neurophysiol*
- 155. Mukamel R, Gelbard H, Arieli A, Hasson U, Fried I, and Malach R (2005)** Coupling between neuronal firing, field potentials, and fMRI in human auditory cortex. *Science* 309: 951-954.
- 156. Nagel G, Szellas T, Huhn W, Kateriya S, Adeishvili N, Berthold P, Ollig D, Hegemann P, and Bamberg E (2003)** Channelrhodopsin-2, a directly light-gated cation-selective membrane channel. *Proc Natl Acad Sci U S A* 100: 13940-13945.
- 157. Nagy A, Eordegh G, Norita M, and Benedek G (2005a)** Visual receptive field properties of excitatory neurons in the substantia nigra. *Neuroscience* 130: 513-518.
- 158. Nagy A, Eordegh G, Norita M, and Benedek G (2003)** Visual receptive field properties of neurons in the caudate nucleus. *Eur J Neurosci* 18: 449-452.
- 159. Nagy A, Eordegh G, Paroczy Z, Markus Z, and Benedek G (2006)** Multisensory integration in the basal ganglia. *Eur J Neurosci* 24: 917-924.
- 160. Nagy A, Paroczy Z, Norita M, and Benedek G (2005b)** Multisensory responses and receptive field properties of neurons in the substantia nigra and in the caudate nucleus. *Eur J Neurosci* 22: 419-424.
- 161. Nair G, and Duong TQ (2004)** Echo-planar BOLD fMRI of mice on a narrow-bore 9.4 T magnet. *Magn Reson Med* 52: 430-434.
- 162. Nallasamy N, and Tsao DY (2011)** Functional connectivity in the brain: effects of anesthesia. *Neuroscientist* 17: 94-106.
- 163. Nelson AJ, Cheney CA, Chen Y-CI, Dai G, Marini RP, Grindlay GC, Ishizawa Y, and Moore CI.** High-Field (9.4T) Magnetic Resonance Imaging in Squirrel Monkey. In: *Development and Plasticity in Sensory Thalamus and Cortex*, edited by Erzurumlu R, Guido W, and Molnár Z. New York: Springer, 2006, p. 288-316.

- 164. Nelson LE, Guo TZ, Lu J, Saper CB, Franks NP, and Maze M (2002)** The sedative component of anesthesia is mediated by GABA(A) receptors in an endogenous sleep pathway. *Nat Neurosci* 5: 979-984.
- 165. Neufeld A, Assaf Y, Graif M, Hendler T, and Navon G (2005)** Susceptibility-matched envelope for the correction of EPI artifacts. *Magn Reson Imaging* 23: 947-951.
- 166. Ogawa S, Lee T, Kay A, and Tank D (1990a)** Brain Magnetic Resonance Imaging with Contrast Dependent on Blood Oxygenation. *Proceedings of the National Academy of Sciences of the United States of America* 87: 9868--9872.
- 168. Ogawa S, Lee TM, Nayak AS, and Glynn P (1990c)** Oxygenation-sensitive contrast in magnetic resonance image of rodent brain at high magnetic fields. *Magn Reson Med* 14: 68-78.
- 169. Ogawa S, Menon RS, Tank DW, Kim SG, Merkle H, Ellermann JM, and Ugurbil K (1993)** Functional brain mapping by blood oxygenation level-dependent contrast magnetic resonance imaging. A comparison of signal characteristics with a biophysical model. *Biophys J* 64: 803-812.
- 170. Ogawa S, Tank DW, Menon R, Ellermann JM, Kim SG, Merkle H, and Ugurbil K (1992)** Intrinsic signal changes accompanying sensory stimulation: functional brain mapping with magnetic resonance imaging. *Proc Natl Acad Sci U S A* 89: 5951-5955.
- 171. Olsrud J, Wirestam R, Brockstedt S, Nilsson AM, Tranberg KG, Stahlberg F, and Persson BR (1998)** MRI thermometry in phantoms by use of the proton resonance frequency shift method: application to interstitial laser thermotherapy. *Phys Med Biol* 43: 2597-2613.
- 172. Paxinos G, and Franklin KBJ.** *The mouse brain in stereotaxic coordinates*. San Diego: Academic Press, 2001, p. xxv, 1 v. (various pagings).
- 173. Peeters RR, Tindemans I, De Schutter E, and Van der Linden A (2001)** Comparing BOLD fMRI signal changes in the awake and anesthetized rat during electrical forepaw stimulation. *Magnetic Resonance Imaging* 19: 821-826.
- 174. Petreanu L, Mao T, Sternson SM, and Svoboda K (2009)** The subcellular organization of neocortical excitatory connections. *Nature* 457: 1142-1145.

- 175. Pezawas L, Meyer-Lindenberg A, Drabant EM, Verchinski BA, Munoz KE, Kolachana BS, Egan MF, Mattay VS, Hariri AR, and Weinberger DR (2005)** 5-HTTLPR polymorphism impacts human cingulate-amygdala interactions: a genetic susceptibility mechanism for depression. *Nature Neuroscience* 8: 828-834.
- 176. Pleger B, Blankenburg F, Ruff CC, Driver J, and Dolan RJ (2008)** Reward facilitates tactile judgments and modulates hemodynamic responses in human primary somatosensory cortex. *J Neurosci* 28: 8161-8168.
- 177. Poudroux G, and Freton E (1979)** Patterns of unit responses to visual stimuli in the cat caudate nucleus under chloralose anesthesia. *Neurosci Lett* 11: 53-58.
- 178. Puil E, and el-Beheiry H (1990)** Anaesthetic suppression of transmitter actions in neocortex. *Br J Pharmacol* 101: 61-66.
- 179. Puil E, Hutcheon B, and Reiner PB (1994)** Isoflurane inhibits calcium currents in neocortical neurons. *Neurosci Lett* 176: 63-66.
- 180. Raichle ME, Grubb RL, Jr., Eichling JO, and Ter-Pogossian MM (1976a)** Measurement of brain oxygen utilization with radioactive oxygen-15: experimental verification. *J Appl Physiol* 40: 638-640.
- 181. Raichle ME, Grubb RL, Jr., Gado MH, Eichling JO, and Ter-Pogossian MM (1976b)** Correlation between regional cerebral blood flow and oxidative metabolism. In vivo studies in man. *Arch Neurol* 33: 523-526.
- 182. Ramanathan S, Hanley JJ, Deniau JM, and Bolam JP (2002)** Synaptic convergence of motor and somatosensory cortical afferents onto GABAergic interneurons in the rat striatum. *J Neurosci* 22: 8158-8169.
- 183. Ramnani N, Behrens TEJ, Penny W, and Matthews PM (2004)** New approaches for exploring anatomical and functional connectivity in the human brain. *Biological psychiatry* 56: 613-619.
- 184. Ranck JB (1975)** Which elements are excited in electrical stimulation of mammalian central nervous system: a review. *Brain research* 98: 417-440.
- 185. Rees G, Friston K, and Koch C (2000)** A direct quantitative relationship between the functional properties of human and macaque V5. *Nat Neurosci* 3: 716-723.

- 186. Reiner A, Jiao Y, Del Mar N, Laverghetta AV, and Lei WL (2003)** Differential morphology of pyramidal tract-type and intratelencephalically projecting-type corticostriatal neurons and their intrastriatal terminals in rats. *J Comp Neurol* 457: 420-440.
- 187. Ries CR, and Puil E (1999)** Mechanism of anesthesia revealed by shunting actions of isoflurane on thalamocortical neurons. *J Neurophysiol* 81: 1795-1801.
- 188. Ritt JT, Andermann ML, and Moore CI (2008)** Embodied information processing: vibrissa mechanics and texture features shape micromotions in actively sensing rats. *Neuron* 57: 599-613.
- 189. Rogers BP, Morgan VL, Newton AT, and Gore JC (2007)** Assessing functional connectivity in the human brain by fMRI. *Magn Reson Imaging* 25: 1347-1357.
- 190. Roy CS, and Sherrington CS (1890)** On the Regulation of the Blood-supply of the Brain. *J Physiol* 11: 85-158 117.
- 191. Sakata S, and Harris KD (2009)** Laminar Structure of Spontaneous and Sensory-Evoked Population Activity in Auditory Cortex. *Neuron* 64: 404-418.
- 192. Scanley BE, Kennan RP, Cannan S, Skudlarski P, Innis RB, and Gore JC (1997)** Functional magnetic resonance imaging of median nerve stimulation in rats at 2.0 T. *Magnetic resonance in medicine* 37: 969-972.
- 193. Shmuel A, Augath M, Oeltermann A, and Logothetis NK (2006)** Negative functional MRI response correlates with decreases in neuronal activity in monkey visual area V1. *Nat Neurosci* 9: 569-577.
- 194. Sicard K, Shen Q, Brevard ME, Sullivan R, Ferris CF, King JA, and Duong TQ (2003)** Regional cerebral blood flow and BOLD responses in conscious and anesthetized rats under basal and hypercapnic conditions: implications for functional MRI studies. *Journal of cerebral blood flow and metabolism* 23: 472-481.
- 195. Silva AC, and Koretsky AP (2002)** Laminar specificity of functional MRI onset times during somatosensory stimulation in rat. *Proc Natl Acad Sci U S A* 99: 15182-15187.

- 196. Smith AM, Lewis BK, Ruttimann UE, Ye FQ, Sinnwell TM, Yang Y, Duyn JH, and Frank JA (1999)** Investigation of low frequency drift in fMRI signal. *Neuroimage* 9: 526-533.
- 197. Sokoloff L (1960)** Quantitative measurements of cerebral blood flow in man. *Methods Med Res* 8: 253-261.
- 198. Sokoloff L, and Kety SS (1960)** Regulation of cerebral circulation. *Physiol Rev Suppl* 4: 38-44.
- 199. Sokoloff L, Reivich M, Kennedy C, Des Rosiers MH, Patlak CS, Pettigrew KD, Sakurada O, and Shinohara M (1977)** The [14C]deoxyglucose method for the measurement of local cerebral glucose utilization: theory, procedure, and normal values in the conscious and anesthetized albino rat. *J Neurochem* 28: 897-916.
- 200. Sommers MG, van Egmond J, Booij LHDJ, and Heerschap A (2009)** Isoflurane anesthesia is a valuable alternative for alpha-chloralose anesthesia in the forepaw stimulation model in rats. *NMR in Biomedicine* 22: 414-418.
- 201. Stephan KE, Riera JJ, Deco G, and Horwitz B (2008)** The Brain Connectivity Workshops: moving the frontiers of computational systems neuroscience. *Neuroimage* 42: 1-9.
- 202. Steriade M, and Amzica F (1996)** Intracortical and corticothalamic coherency of fast spontaneous oscillations. *Proc Natl Acad Sci U S A* 93: 2533-2538.
- 203. Sultan F, Augath M, and Logothetis N (2007)** BOLD sensitivity to cortical activation induced by microstimulation: comparison to visual stimulation. *Magn Reson Imaging* 25: 754-759.
- 204. Sur M, Nelson RJ, and Kaas JH (1982)** Representations of the body surface in cortical areas 3b and 1 of squirrel monkeys: comparisons with other primates. *J Comp Neurol* 211: 177-192.
- 205. Tehovnik EJ, Tolias AS, Sultan F, Slocum WM, and Logothetis NK (2006)** Direct and indirect activation of cortical neurons by electrical microstimulation. *Journal of neurophysiology* 96: 512-521.
- 206. Tolias AS, Sultan F, Augath M, Oeltermann A, Tehovnik EJ, Schiller PH, and Logothetis NK (2005)** Mapping cortical activity elicited with electrical microstimulation using FMRI in the macaque. *Neuron* 48: 901-911.

- 207. Tombari D, Loubinoux I, Pariente J, Gerdelat A, Albucher J-F, Tardy J, Cassol E, and Chollet F (2004)** A longitudinal fMRI study: in recovering and then in clinically stable sub-cortical stroke patients. *Neuroimage* 23: 827-839.
- 208. Tommerdahl M, Favorov O, and Whitsel BL (2002)** Optical imaging of intrinsic signals in somatosensory cortex. *Behav Brain Res* 135: 83-91.
- 209. Triantafyllou C, Hoge RD, Krueger G, Wiggins CJ, Potthast A, Wiggins GC, and Wald LL (2005)** Comparison of physiological noise at 1.5 T, 3 T and 7 T and optimization of fMRI acquisition parameters. *Neuroimage* 26: 243-250.
- 210. Triantafyllou C, Wald LL, Wiggins CJ, Potthast A, Wiggins GC, Krueger G, and Hoge RD (2004)** Physiological Noise in fMRI: Comparison at 1.5T, 3T and 7T and Dependence on Image Resolution. *Proc Intl Soc Mag Reson Med* 11:
- 211. Trubel HK, Kida I, and Hyder F (2004)** Implications of temperature changes in the brain for fMRI. *Proc Intl Soc Mag Reson Med* 11: 1441.
- 212. Tsurugizawa T, Uematsu A, Uneyama H, and Torii K (2010)** Effects of isoflurane and alpha-chloralose anesthesia on BOLD fMRI responses to ingested l-glutamate in rats. *Neuroscience* 165: 244-251.
- 213. Ueki M, Mies G, and Hossmann KA (1992)** Effect of alpha-chloralose, halothane, pentobarbital and nitrous oxide anesthesia on metabolic coupling in somatosensory cortex of rat. *Acta Anaesthesiol Scand* 36: 318-322.
- 214. Van Dijk KRA, Hedden T, Venkataraman A, Evans KC, Lazar SW, and Buckner RL (2010)** Intrinsic functional connectivity as a tool for human connectomics: theory, properties, and optimization. *Journal of neurophysiology* 103: 297-321.
- 215. Vanduffel W, Fize D, Mandeville JB, Nelissen K, Van Hecke P, Rosen BR, Tootell RB, and Orban GA (2001)** Visual motion processing investigated using contrast agent-enhanced fMRI in awake behaving monkeys. *Neuron* 32: 565-577.
- 216. Vijayan S, Hale GJ, Moore CI, Brown EN, and Wilson M (2010)** Activity in the Barrel Cortex During Active Behavior and Sleep. *Journal of Neurophysiology* 103: 2074-2084.

- 217. Vincent JL, Kahn I, Van Essen DC, and Buckner RL (2010)** Functional connectivity of the macaque posterior parahippocampal cortex. *J Neurophysiol* 103: 793-800.
- 218. Vincent JL, Patel GH, Fox MD, Snyder AZ, Baker JT, Van Essen DC, Zempel JM, Snyder LH, Corbetta M, and Raichle ME (2007)** Intrinsic functional architecture in the anaesthetized monkey brain. *Nature* 447: 83-86.
- 219. Vincent JL, Snyder AZ, Fox MD, Shannon BJ, Andrews JR, Raichle ME, and Buckner RL (2006)** Coherent spontaneous activity identifies a hippocampal-parietal memory network. *J Neurophysiol* 96: 3517-3531.
- 220. Viswanathan A, and Freeman RD (2007)** Neurometabolic coupling in cerebral cortex reflects synaptic more than spiking activity. *Nat Neurosci* 10: 1308-1312.
- 221. Wakamori M, Ikemoto Y, and Akaike N (1991)** Effects of two volatile anesthetics and a volatile convulsant on the excitatory and inhibitory amino acid responses in dissociated CNS neurons of the rat. *J Neurophysiol* 66: 2014-2021.
- 222. Wang H, Peca J MM, Matsuzaki K, Noguchi J, Qiu L, Wang D, Zhang F, Boyden E, Deisseroth K, Kasai H, Hall WC, Feng G, , and GJ A (2007)** High-speed mapping of synaptic connectivity using photostimulation in Channelrhodopsin-2 transgenic mice. *Proc Natl Acad Sci U S A* 104: 8143-8148.
- 223. Wang J, Deichmann R, Turner R, and Ordidge R (2004)** 3D DT-MRI using a reduced-FOV approach and saturation pulses. *Magnetic Resonance in Medicine* 51: 853 - 857.
- 224. Ward NS, Brown MM, Thompson AJ, and Frackowiak RS (2003)** Neural correlates of motor recovery after stroke: a longitudinal fMRI study. *Brain* 126: 2476-2496.
- 225. Weder BJ, Leenders KL, Vontobel P, Nienhusmeier M, Keel A, Zaunbauer W, Vonesch T, and Ludin HP (1999)** Impaired somatosensory discrimination of shape in Parkinson's disease: association with caudate nucleus dopaminergic function. *Hum Brain Mapp* 8: 1-12.
- 226. West MO (1998)** Anesthetics eliminate somatosensory-evoked discharges of neurons in the somatotopically organized sensorimotor striatum of the rat. *J Neurosci* 18: 9055-9068.

- 227. White EL, and DeAmicis RA (1977)** Afferent and efferent projections of the region in mouse SmL cortex which contains the posteromedial barrel subfield. *J Comp Neurol* 175: 455-482.
- 228. Wilm BJ, Svensson J, Henning A, Pruessmann KP, Boesiger P, and Kollias SS (2007)** Reduced field-of-view MRI using outer volume suppression for spinal cord diffusion imaging. *Magnetic Resonance in Medicine* 57: 625 - 630.
- 229. Wilson CJ (1987)** Morphology and synaptic connections of crossed corticostriatal neurons in the rat. *J Comp Neurol* 263: 567-580.
- 230. Woolsey TA, and Van der Loos H (1970)** The structural organization of layer IV in the somatosensory region (SI) of mouse cerebral cortex. The description of a cortical field composed of discrete cytoarchitectonic units. *Brain Res* 17: 205-242.
- 231. Wright AK, Ramanathan S, and Arbuthnott GW (2001)** Identification of the source of the bilateral projection system from cortex to somatosensory neostriatum and an exploration of its physiological actions. *Neuroscience* 103: 87-96.
- 232. Xiong J, Gao J, Lancaster J, and Fox P (1995a)** Clustered pixels analysis for functional MRI activation studies of the human brain. *Hum Brain Mapp* 3: 287-301.
- 234. Xu F, Liu N, Kida I, Rothman DL, Hyder F, and Shepherd GM (2003)** Odor maps of aldehydes and esters revealed by functional MRI in the glomerular layer of the mouse olfactory bulb. *Proc Natl Acad Sci U S A* 100: 11029-11034.
- 235. Yablonskiy DA, Ackerman JJ, and Raichle ME (2000)** Coupling between changes in human brain temperature and oxidative metabolism during prolonged visual stimulation. *Proc Natl Acad Sci U S A* 97: 7603-7608.
- 236. Yacoub E, Shmuel A, Pfeuffer J, Van De Moortele PF, Adriany G, Andersen P, Vaughan JT, Merkle H, Ugurbil K, and Hu X (2001)** Imaging brain function in humans at 7 Tesla. *Magn Reson Med* 45: 588-594.
- 237. Yaroslavsky AN (2002)** Optical Properties of Selected Native and Coagulated Human Brain Tissues In Vitro in the Visible and Near Infrared Spectral Range. *Phys Med Biol* 47: 2059-2073.
- 238. Yin HH, and Knowlton BJ (2006)** The role of the basal ganglia in habit formation. *Nat Rev Neurosci* 7: 464-476.

- 239. Zhang F, Aravanis A, Adamantidis A, de Lecea L, and Deisseroth K (2007a)** Circuit-breakers: optical technologies for probing neural signals and systems. *Nat Rev Neurosci* 8: 577--581.
- 240. Zhang F, Gradinaru V, Adamantidis AR, Durand R, Airan RD, de Lecea L, and Deisseroth K (2010)** Optogenetic interrogation of neural circuits: technology for probing mammalian brain structures. *Nat Protoc* 5: 439-456.
- 241. Zhang F, Wang L-P, Boyden E, and Deisseroth K (2006)** Channelrhodopsin-2 and optical control of excitable cells. *Nature Methods* 3: 785--792.
- 242. Zhang F, Wang L-P, Brauner M, Liewald J, Kay K, Watzke N, Wood P, Bamberg E, Nagel G, Gottschalk A, and Deisseroth K (2007b)** Multimodal fast optical interrogation of neural circuitry. *Nature* 446: 633--639.
- 244. Zhao F, Wang P, and Kim SG (2004)** Cortical depth-dependent gradient-echo and spin-echo BOLD fMRI at 9.4T. *Magn Reson Med* 51: 518-524.
- 245. Zhao S, Cunha C, Zhang F, Liu Q, Gloss B, Deisseroth K, Augustine GJ, and G. F (2008)** Improved expression of halorhodopsin for light-induced silencing of neuronal activity. *Brain Cell Biol* 36: 141-154.
- 246. Zhu P, Narita Y, Bundschuh ST, Fajardo O, Scharer YP, Chattopadhyaya B, Bouldoires EA, Stepien AE, Deisseroth K, Arber S, Sprengel R, Rijli FM, and Friedrich RW (2009)** Optogenetic Dissection of Neuronal Circuits in Zebrafish using Viral Gene Transfer and the Tet System. *Front Neural Circuits* 3: 21.